Max-Planck-Institut
für Meteorologie

MAX-PLANCK-GESELLSCHAFT

International Max Planck Research School
on Earth System Modelling

Susceptibility of trade wind cumulus clouds to precipitation

Katrin Lonitz

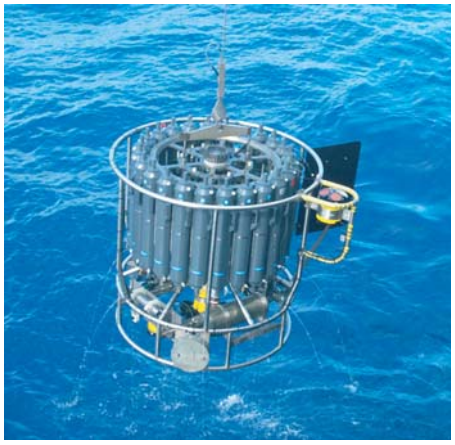

Berichte zur Erdsystemforschung 147/2014

Reports on Earth System Science

Hinweis

Die Berichte zur Erdsystemforschung werden vom Max-Planck-Institut für Meteorologie in Hamburg in unregelmäßiger Abfolge herausgegeben.

Sie enthalten wissenschaftliche und technische Beiträge, inklusive Dissertationen.

Die Beiträge geben nicht notwendigerweise die Auffassung des Instituts wieder.

Die "Berichte zur Erdsystemforschung" führen die vorherigen Reihen "Reports" und "Examensarbeiten" weiter.

Notice

The Reports on Earth System Science are published by the Max Planck Institute for Meteorology in Hamburg. They appear in irregular intervals.

They contain scientific and technical contributions, including Ph. D. theses.

The Reports do not necessarily reflect the opinion of the Institute.

The "Reports on Earth System Science" continue the former "Reports" and "Examensarbeiten" of the Max Planck Institute.

Anschrift / Address

Max-Planck-Institut für Meteorologie
Bundesstrasse 53
20146 Hamburg
Deutschland

Tel.: +49-(0)40-4 11 73-0
Fax: +49-(0)40-4 11 73-298
Web: www.mpimet.mpg.de

Layout:

Bettina Diallo, PR & Grafik

Titelfotos:
vorne:
Christian Klepp - Jochem Marotzke - Christian Klepp
hinten:
Clotilde Dubois - Christian Klepp - Katsumasa Tanaka

Berichte zur Erdsystemforschung 147/2014

Susceptibility of trade wind cumulus clouds to precipitation

Katrin Lonitz

aus Gera

Hamburg 2014

Reports on Earth System Science 147/2014

ISSN 1614-1199

Katrin Lonitz
Max-Planck-Institut für Meteorologie
Bundesstrasse 53
20146 Hamburg

Als Dissertation angenommen
vom Department Geowissenschaften der Universität Hamburg

auf Grund der Gutachten von
Prof. Dr. Bjorn Stevens
und
Dr. Ákos Horváth

Hamburg, den 28. Januar 2014
Prof. Dr. Christian Betzler
Leiter des Departments für Geowissenschaften

ISSN 1614-1199

Susceptibility of trade wind cumulus clouds to precipitation

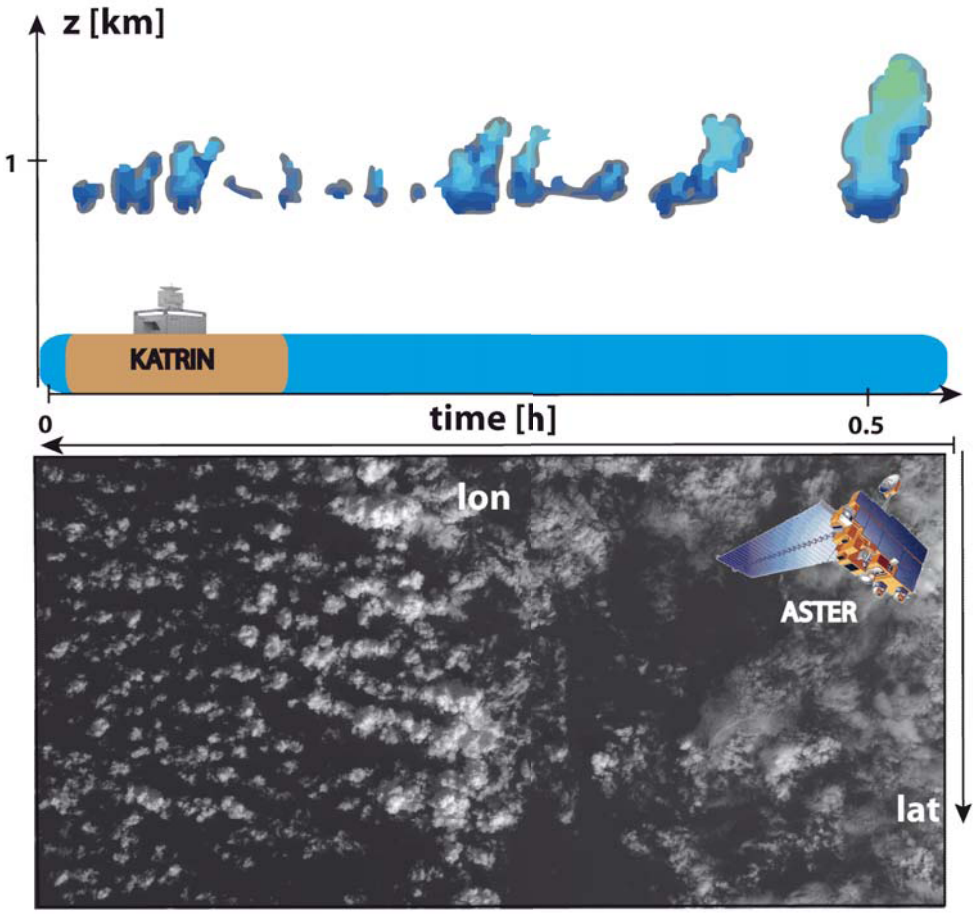

Katrin Lonitz

Hamburg 2014

Abstract

Using ground-based lidar and radar remote sensing measurements from the Barbados-Cloud-Observatory (BCO) and space-borne measurements of the Advanced Spaceborne Thermal Emission and Reflection Radiometer (ASTER), the susceptibility of trade wind cumuli to form precipitation and their degree of organization is investigated. The influence of aerosol concentration and thermodynamic state on the development of precipitation is analyzed from cloud radar echoes of developing cumuli before the onset of active precipitation.

At any specific height above cloud base, the radar reflectivity Z^* depends on the amount of cloud water, which varies with meteorology, and the cloud droplet number concentration, which varies with the aerosol. Clouds with a large Z^* are found to have a higher tendency to form precipitation at lower heights than clouds with a small Z^*. Under similar meteorological conditions, Z^* is expected to be large in an environment with few aerosols and small in an environment with numerous aerosols. The aerosol environment is defined using three methods. Of these three methods, only the one based on the Raman lidar linear depolarization ratio, which measures dusty conditions, shows a positive correlation between aerosol concentration and Z^*. Dusty conditions, however, vary seasonally, and co-vary with relative humidity. A simple model shows that small (few percent) changes in the relative humidity in the cloud layer can influence Z^* as strongly as an order of magnitude change in the cloud droplet number concentration. When clouds are conditioned on their ambient relative humidity the sensitivity of Z^* to dust even vanishes.

Furthermore, analysis of cloud radar measurements reveal that large Z^* days are characterized by clouds with a high cloud top height, which are also found to have a high rain amount. To identify rainy conditions in ASTER scenes, the relationship between rain amount and cloud top height is assumed to be the same as observed in measurements by the cloud radar. A smaller cloud cover is found for ASTER scenes with high cloud top height compared to scenes with low cloud top height. Analysis of the distribution of cloud sizes show that large clouds contribute more to the total cloud cover than small clouds, especially in ASTER scenes with high cloud top height during the wet season, which are characterized by vigorous convective clouds. An investigation of the nearest neighbor distance between clouds shows that clouds with high cloud top heights have a high tendency to organize into clusters. This suggests, that during the wet season a high degree of clustering occurs for few deep precipitating clouds, which are associated with a low cloud cover. Small variations in the humidity field of the (sub-)cloud layer are a strong candidate to be able to explain the susceptibility of trade wind clouds to precipitation and hence, the organization of the cumulus cloud field.

This thesis emphasizes to focus future investigations on the impact of subtle changes in the thermodynamic environment of shallow cumuli on their tendency to form rain and how it relates to their degree of organization.

Contents

1 Introduction **1**
1.1 Motivation and Background 1
1.2 Outline 4

2 Instruments and Data **7**
2.1 Barbados-Cloud-Observatory 7
2.2 Cloud radar 8
2.2.1 Operation of cloud radar 9
2.2.2 Doppler spectrum 13
2.2.3 Radar reflectivity and radar reflectivity factor 14
2.2.4 Doppler velocity 18
2.3 Raman lidar 19
2.4 ASTER 21
2.5 Back-trajectories 24

3 Robustness of cloud radar retrievals **27**
3.1 Intercomparison of the two cloud radars 27
3.1.1 Differences in radar observables 28
3.1.2 Detection of non-meteorological radar retrievals and other spurious echoes 30
3.1.3 Differences in cloud radar software 34
3.2 Comparison of different elevation angles 36
3.3 Conclusion about radar data treatment 38

4 Signature of aerosols and meteorology in microphysical properties of trade wind cumuli using KATRIN **41**
4.1 Introduction 41
4.2 Background and theoretical framing 42
4.3 Methodology 44
4.3.1 Identifying cloud entities 46
4.3.2 Different aerosol environments 46
4.3.3 Data treatment 48
4.4 Differences in the precipitation characteristics 49
4.5 Z-lapse rate for different aerosol environments 51

4.6 Z-lapse rate and its dependency on meteorological conditions 55
4.7 Summary and Conclusion 60

5 Variability of macrophysical properties of trade wind cumuli 63
5.1 Introduction 63
5.2 Methodology 64
5.2.1 Identification of shallow clouds in ASTER data 66
5.3 Characteristics of raining clouds 70
5.3.1 Cloud characteristics from KATRIN 71
5.3.2 Case study 73
5.4 Characteristics of cloudiness in the trades 74
5.4.1 Cloud cover 74
5.4.2 Cloud size distribution 76
5.4.3 Spatial distribution 78
5.5 Summary and Conclusion 80

6 Conclusion and Outlook 83
6.1 General summary and conclusion 83
6.2 Outlook 85

Appendix 89
Back-trajectory analysis 89

Acronyms 89

Bibliography 93

List of Figures

1.1 Schematic showing the vertical cross section along the path of a trade wind trajectory, with clouds drawn larger than their actual scale. Typical wind speed at the various levels are indicated by arrows at the right. The moist layer deepens by about 300 m in 800 km horizontal distance. From Malkus (1958). 1
1.2 Schematic showing cloud regimes in thermally direct circulations. From Stevens (2005). 2

2.1 Geographical location of the Barbados-Cloud-Observatory (Courtesy: Bjorn Stevens). 8
2.2 Picture of the Barbados-Cloud-Observatory with its instruments. The Differential absorption lidar (DIAL) and the microwave radiometer from the University Cologne have been deployed only for a few months in the past and are currently not under operation (Courtesy: Friedhelm Jansen). 9
2.3 Sketch displays the operating mode of a cloud radar. Electromagnetic radiation with a well defined wavelength λ is emitted by the radar. The meteorological targets - here cloud droplets - which are in the line of sight of the radar, scatter the emitted waves. The sum of all directly backscattered signals are received by the radar antenna. Sketch modified after Melchionna (2010). 10
2.4 Images of the two cloud radars, used in this study (a) KIT and (b) KATRIN. (Courtesy: Friedhelm Jansen) 11
2.5 Schematic showing the monthly fraction of days (in green) when KATRIN was measuring between January 2011 and March 2012. Total fraction is outlined at the top of every bar. 12
2.6 Schematic showing a gaussian distributed $S(f_{\mathrm{D}})$ with the maximum value S_0 for the mean f_0, and the standard deviation σ. 13
2.7 Basic representation how the cloud radar observes the variety in clouds at the East coast of Barbados. (Courtesy: Norbert Noreiks) 15
2.8 Six minute mean of dBZ measured by the KIT Radar on January 6$^{\mathrm{th}}$ 2011, displayed as a function of height and time. 18
2.9 Six minute mean of v_{D} measured by the KIT Radar on January 6$^{\mathrm{th}}$ 2011, displayed as a function of height and time. 19

2.10 View of the green laser beam from the operating Raman lidar at the BCO. In the background Ragged Point with the AERONET station is visible. (Courtesy: Björn Brügemann and Ilya Serikov.) 20

2.11 Two minute means of a) particle backscatter at $\lambda = 532\,\text{nm}$, b) particle linear depolarization ratio at $\lambda = 532\,\text{nm}$ and c) water vapor mixing ratio measured by Raman lidar on January 6$^{\text{th}}$ 2011, displayed as a function of height and time. Black vertical stripes mark times when no measurements were obtained, as for example during times of precipitation (for example at 4 UTC, also visible in Fig. 2.8) or direct sun overhead. The water vapor mixing ratio can only be measured during night time. 22

2.12 ASTER snapshot close to the BCO on January 6$^{\text{th}}$ 2011 at 14:05 UTC, observed in the visible channel 1 from the Level 1B product. In the right left corner a sub-sample of the whole cloud field is displayed, showing the capability of ASTER to retrieve different textures of clouds. 23

2.13 Map shows Caribbean islands, marking the region (black bounding box) for which ASTER data was retrieved in 2011. The bounding box measures: 18°N - 11°N and 60°W - 50°W. Barbados is located inside the bounding box and the other Caribbean islands outside of it. Blue colors mark ocean and gray colors land. 24

2.14 Map of air mass' origin. In blue the origins of maritime air masses are highlighted and in red continental air masses. 25

3.1 Frequency of occurrence of KATRIN quantities vs. KIT quantities using the dataset from 22 December 2010 to 9 January 2011. 29

3.2 Time-height cross section of reflectivity for both cloud radars operating in the vertically pointing mode on 6 January 2011. Here, no lower limit for Z is applied. 31

3.3 Dependencies on the minimum reflectivity which is allowed to occur for retrievals up to 5 km using the vertically pointing mode for the measurements period from 22 December 2010 to 9 January 2011. 32

3.4 Time-height cross section of reflectivity for both cloud radars operating in the vertically pointing mode on 6 January 2011. Here, a lower limit of $\text{dBZ}_{\text{min}} = -35$ is applied. 33

3.5 Reflectivity-height histograms from retrievals of Z using the vertically pointing mode for the measurements period from 22 December 2010 to 9 January 2011. 35

3.6 Reflectivity-height histogram of different elevation angles from KATRIN for the measurements period from February 2011 to April 2011. 37

3.7 Time-height histogram from retrievals using different elevation angles for the measurements period from 1 January 2011 to 4 May 2011. 39

4.1 Reflectivity dBZ as a function of height (z) for a droplet distribution $n(D)$ behaving as a Γ-distribution [Eq. (4.2)]. k^2 is chosen to be 2.25. The black line patterns display conditions of different $\beta^2 N^{-1}$, which are set to be constant with height. The gray dashed line represents a decreasing $\beta^2 N^{-1}$ from 4.0 at cloud base $z_\mathrm{b} = 0.5\,\mathrm{km}$ to $\beta^2 N^{-1} = 1.0$ at cloud top $z_\mathrm{t} = 1.5\,\mathrm{km}$. 45

4.2 Reflectivity (contoured, upper panel) versus height and time, for a thirty minute period on 2nd February 2012. Lower panel identifies shallow cloud entities in black and other clouds in red. 47

4.3 Reflectivity-height histograms normalized by the sum of all actual retrievals per height level. 48

4.4 Distribution of daily fraction of clouds with downward moving cloud tops of $v_\mathrm{t} \leq -0.5\,\mathrm{m\,s^{-1}}$ for every shallow cloud entity having $720\,\mathrm{m} \leq z_\mathrm{t} \leq 1140\,\mathrm{m}$. The fractional distribution is calculated for every 5% and smoothed using a running mean of three subsequent points. Different colors refer to different regimes, as indicated in the Figure. Caution: the y-axis is displayed in a logarithmic scale. 50

4.5 Histogram showing the frequency of occurrence (FoO) for shallow clouds having a certain daily mean velocity at cloud top $\tilde{v}_\mathrm{t}$, normalized by the sum of all clouds of a particular z_t. The binning in z_t is 210 m and the FoO is calculated for every $\tilde{v}_\mathrm{t} = 0.5\,\mathrm{m\,s^{-1}}$. Panels refer to conditional samples during large Z^* and small Z^*. 51

4.6 Distribution of z_t from developing cumulus clouds. Solid lines show the fractional distribution per $\triangle z_\mathrm{t} = 60\,\mathrm{m}$ and the dashed lines to their corresponding cumulative distribution. Blue color refer to clouds during large Z^* days, red to clouds during small Z^* days. 52

4.7 Change of averaged reflectivity $\tilde{Z}_\mathrm{z}$ with height of developing cumulus clouds during non-dusty (blue line) and dusty (red line) conditions. Only $\tilde{Z}_\mathrm{z}$ are displayed which pass the 2-sided Kolmogorov-Smirnov test. The dotted colored lines display the non-linear regression according to Eq. 4.6 for both regimes for $n(D)$ behaving as a Γ-distribution function with $k^2 = 2.25$ and an assumed cloud base height of 500 m. The different black lines display the change of Z with height for conditions of various $\beta^2 N^{-1}$, which are set to be constant with height as described in section 4.2. Further details see Fig. 4.1. 53

4.8 Distribution of $\beta^2 N^{-1}$ of every developing cumulus cloud. Black lines show the frequency per $0.2 \cdot 10^{-4}\mathrm{cm}^3$ of all conditions and red lines of dusty conditions. At the top the 25^{th} percentile $\mathrm{x}_{25} = 0.53 \cdot 10^{-4}\mathrm{cm}^3$, the median $\mathrm{x}_{50} = 0.78 \cdot 10^{-4}\mathrm{cm}^3$ and the 75^{th} percentile $\mathrm{x}_{75} = 1.21 \cdot 10^{-4}\mathrm{cm}^3$ of the distribution in $\beta^2 N^{-1}$ during all conditions is marked. 55

4.9 Height profiles of averaged daily median relative humidity, $\bar{\eta}$, during non-cloudy conditions measured at nighttime (0 - 8 UTC). Relative humidity is derived from Raman lidar at the BCO. Only measurements are considered when the standard deviation is less than 35% of the actual value. The shadings corresponds to the inner-quartile range. 56

4.10 Distribution of daily median relative humidity $\eta_{1.5\,\mathrm{km}}$ in 1.5 km height for days with developing cumulus clouds. Blue lines show the frequency per $\Delta\eta = 5\,\%$ for non-dusty days and red lines for dusty days. 59

5.1 ASTER snapshots close to the BCO in February 2011, observed in the visible channel 1 from the Level 1B product. 65
5.2 Box-and-whisker plot of minimum reflectance (r_{min}) and maximum brightness temperature (Tb_{max}) measured with ASTER for all months in 2011. 68
5.3 Monthly means in reflectance and brightness temperature for all percentiles (plus minimum and maximum) and all months in 2011. 69
5.4 Frequency of detecting clouds having a certain cloud top height (z_t) for height levels of 30 m compiled from KATRIN data, measured between January 2011 to March 2012. The measurements are segregated into days which are very and less rainy, and have a large Z^* and small Z^*. 71
5.5 Frequency of occurrence of daily rain amount for conditional samples of days with high z_t and days with low z_t, and large Z^* days and small Z^* days. 73
5.6 Frequency of occurrence [%] of cloud cover (cc) for a) all scenes (colored in gray) and b) high z_t (colored in turquoise) and low z_t scenes (colored in orange) with shallow clouds obtained from ASTER scenes in 2011, binned for every cc = 1%. 75
5.7 Normalized cloud size distribution on log-log axes for shallow clouds from a) all scenes (colored in gray) and b) high z_t (colored in turquoise) and low z_t scenes (colored in orange) obtained from ASTER scenes in 2011. The dashed lines correspond to linear fits by a power law [Eq. (5.7)]. The binning of 5 pixels is chosen for cloud size. 77
5.8 Normalized distribution of NND $\cdot$size^{-1} for trade wind cumuli retrieved with ASTER in 2011. 79

A.1 Reflectivity-height histogram from KIT retrievals using the vertically pointing mode for the CARRIBA measurements in November 2010. 90

List of Tables

2.1 Specifications of the KATRIN cloud radar in the set up on 24^{th} of April 2013. 12

4.1 Number of days during non-dusty and dusty conditions for different seasons between 1 January 2011 and 15 March 2012. Winter season includes months December to May and summer season includes months June to November. . 54
4.2 Typical values of η, β, $\beta^2 N^{-1}$ and N_{new} at z_1 for shallow clouds with $N = 100\,\text{cm}^{-3}$ are listed. The change in total water inside the cloud with height behaves according to the mass flux equation of Tiedtke (1989) with the environmental total water decreasing linearly with height. $\Delta\text{dBZ} = \text{dBZ}_{\text{humid}} - \text{dBZ}_{\text{dry}}$. 58

5.1 The 25^{th} percentile ($z_{\text{t}_{25}}$) of cloud top height (z_{t}) as well as its median ($\widetilde{z_{\text{t}}}$), the 75^{th} percentile ($z_{\text{t}_{75}}$) and the mean ($\widehat{z_{\text{t}}}$) in meters. 72
5.2 Mean in projected cloud cover [%] for all ASTER scenes in 2011, during the dry winter season (December - May) and wet summer season (June - November) for all scenes, scenes with high z_{t} and scenes with low z_{t}. 76
5.3 Slope parameter for all ASTER scenes in 2011, during the dry winter season (December - May) and wet summer season (June - November) for all scenes, scenes with high z_{t} and scenes with low z_{t}. 78
5.4 Fraction of clouds [%] with nearest neighbor within a distance of 1 times less than their cloud size ($\text{NND} \cdot \text{size}^{-1} < 1$) for all ASTER scenes in 2011, during the dry winter season (December - May) and wet summer season (June - November) for all scenes, scenes with high z_{t} and scenes with low z_{t}. 80

Chapter 1

Introduction

1.1 Motivation and Background

Trade wind cumuli are shallow convective clouds that can be found over the subtropical oceans of the trade wind region. This region is located outside of the Intertropical Convergence Zone (ITCZ) between 30°S and 30°N. The main characteristic of the trades are the prevailing surface winds, namely the trade winds, blowing predominantly from the northeast in the northern hemisphere and from the southeast in the southern hemisphere. Back in the days, sailors used those winds to explore continents and trade goods across the world.

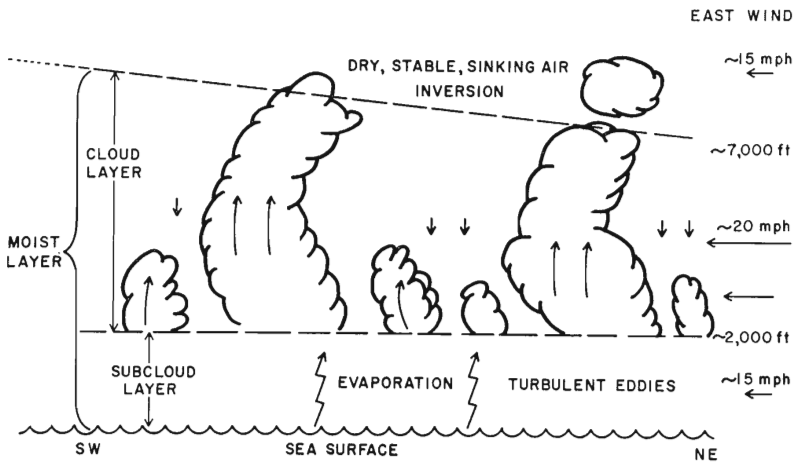

Figure 1.1: Schematic showing the vertical cross section along the path of a trade wind trajectory, with clouds drawn larger than their actual scale. Typical wind speed at the various levels are indicated by arrows at the right. The moist layer deepens by about 300 m in 800 km horizontal distance. From Malkus (1958).

In the late 1950s Joanne Malkus studied the trade wind region and its role on the global scale. Fig. 1.1 displays the vertical structure of the prevailing warm, maritime

shallow cumulus clouds in the trades, or in other words the "trade wind cumuli". These clouds are embedded in a moist convective and conditionally unstable layer, whose vertical extent is limited by a layer of dry air aloft. The vertical zone in which subsidence and convection balance each other, is called "trade wind inversion", a zone of rapid drying and stabilization. As shown in Fig. 1.1, the trade wind inversion rises in height westward towards the ITCZ as surface driven moist convection penetrates into the dry air above the inversion with greater frequency, weakening the inversion. In the ITCZ the inversion breaks down, enabling shallow cumuli to grow to cumulonimbi and transporting warm and moist air from the surface to the tropopause. In the upper troposphere a large amount of latent heat is released through condensation and transported eastward towards the mid-latitudes, balancing local energy deficits. This circulation of a westward current in the lower troposphere with strong upward motions in the ITCZ, an eastward motion in the upper troposphere and strong subsidence over cold subtropical oceans at higher latitudes, is known as the Hadley circulation (see Fig. 1.2).

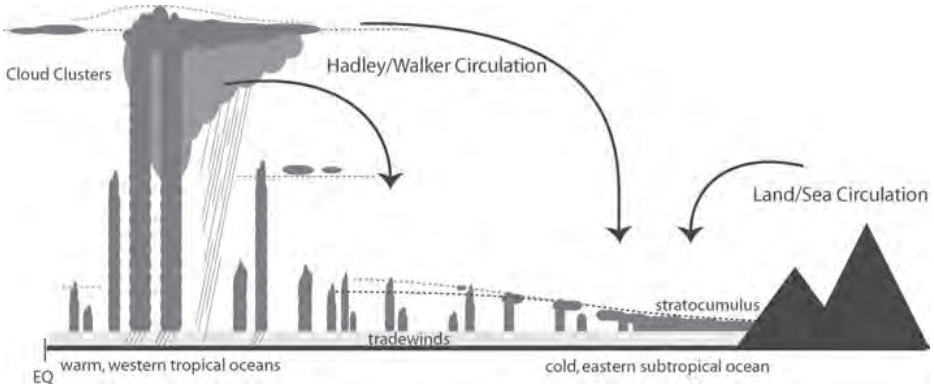

Figure 1.2: Schematic showing cloud regimes in thermally direct circulations. From Stevens (2005).

The major role of shallow cumuli in the trades is to transport moisture upward towards the trade wind inversion where warm, moist air moving upwards competes with subsiding dry air aloft. The evaporation of liquid water premoistens the atmosphere for deeper convection and induces a mixing of warm, dry air from the layer aloft of the inversion into the moist convective layer. This entrainment of dry air helps to maintain the strong surface evaporation and hence, the formation of trade wind cumuli. The accumulation of latent heat in the trades determines the total available energy in the ITCZ and the energy supply for the subtropics (Malkus, 1958). That means, trade wind cumuli have a strong impact on the tropical circulation (Riehl et al., 1951). A detailed understanding of underlying processes of the formation of those clouds, precipitation and modulating factors is therefore from great importance.

In particular, precipitation induced by shallow cumuli plays an important role for the evolution of the boundary layer, as stated by Jensen et al. (2000). It was already recognized in the 1950s that a detailed understanding about precipitating trade wind cumuli and

their formation is needed, e.g. by Byers and Hall (1955). Later, Short and Nakamura (2000) showed that shallow convection forms 20% of the total precipitation in the tropics. Furthermore, processes related to precipitation encounter a range of scales, with the formation of precipitation in the micrometer range up to areas affected by evaporative cooling of rain showers of several hundred meters to kilometers ($\mathcal{O}(100\,\mathrm{m})$ - $\mathcal{O}(10\,\mathrm{km})$). As discussed by Rauber et al. (2007), the relatively rapid initiation of warm rain on the micrometer scale is still not well understood. Large-Eddy-Simulations by Seifert and Heus (2013) suggested further that the precipitation behavior of shallow cumuli on the macrophysical scale correlates with the organization of clouds.

In order to improve an understanding of processes related to trade wind cumuli, the first large field experiments in the trades took place in 1969. The Atlantic Trade Wind Experiment (ATEX) studied the boundary layer in the trades and the Barbados Oceanographic and Meteorological EXperiment (BOMEX)[1] determined rates for the transfer of water vapor, heat and momentum at the boundary between sea and air. In 2007, the Rain In shallow Cumulus over the Ocean (RICO) campaign around Antigua and Barbuda in the Caribbean concentrated on the formation of rain by trade wind cumuli (Rauber et al., 2007). Nuijens et al. (2009) found that the variability in precipitation relates to variability in humidity and zonal wind speed. A comparison of twelve different Large-Eddy-Simulations which used data from RICO, showed that the amount and structure of precipitation is (at least) partly related to microphysical assumptions made in models (van Zanten et al., 2011), highlighting the high sensitivity of precipitation in the trades towards subtle changes in the clouds and their environment.

One of the factors which is thought to modulate precipitation is aerosol concentration. Albrecht (1989), and Liou and Ou (1989) hypothesized that increasing aerosol amounts hinder warm rain formation and hence increase cloud amount, as also suggested by observations from satellites (Kaufman et al., 2005). Very large changes in the cloud condensation nuclei concentration (and hence the aerosol more generally) are beyond dispute to have an influence on cloud properties. To which degree, however, remains under discussion (Stevens and Brenguier, 2009) as other factors (e.g. relative humidity) could also explain the correlation between cloud amount and precipitation efficiency. In fact, the extent to which microphysical changes help explain variability in the propensity of clouds to precipitate and the degree to which changes in precipitation efficiency affect cloud amount is much less clear (Stevens and Feingold, 2009).

Furthermore, an understanding on the development of precipitation and how it relates to sizes of clouds and their organization is still lacking. As stated by Snodgrass et al. (2009) arc-shaped clusters of shallow cumuli are associated with the production of significant rainfall rates. Similar to findings for tropical deep convection (Tompkins, 2001), the spatial organization of cold pools is hypothesized to be important for convection. During RICO, precipitating clouds were found to be deeper ($\sim 3\,\mathrm{km}$ depth) than non-precipitating clouds and organized in successive arcs (Rauber et al., 2007). To which extent this degree of organization is related to precipitating trade wind cumuli and their contribution to the total cloud cover, however, needs further analysis.

[1] www.eol.ucar.edu/projects/bomex

This thesis contributes to a better understanding of the relative role of aerosol as compared to meteorological changes in regulating precipitation from shallow convection, and their degree of organization. For this purpose, measurements of different ground-based and space-borne observations are exploited. One set of observations is recorded at the Barbados-Cloud-Observatory (BCO), which compromises a suite of remote sensing instruments, like the KATRIN cloud radar, a Raman lidar, a Micro Rain Radar and a ceilometer. This unique combination of instruments enables to characterize trade wind cumulus clouds, their precipitation behavior, atmospheric aerosol concentration, and the humidity and temperature of the environment. The second set of observation is recorded by a space-borne radiometer, named Advanced Spaceborne Thermal Emission and Reflection Radiometer (ASTER), which can observe trade wind cumuli and their organization with a very high spatial resolution up to 15 m. For the first time, long-term measurements in the trades allow to undertake a detailed study about robust signals of ***driving factors of the onset of precipitation*** of maritime shallow cumuli and their ***macrophysical characteristics***: the organization and the contribution of different cloud sizes to the total cloud cover.

1.2 Outline

In this regard, this thesis aims to answer the following three research questions:

1. ***Can measurements from a single location describe the variety of cloudiness in the trades?***
2. ***Can aerosols significantly alter the onset of precipitation of trade wind cumuli?***
3. ***Do precipitating clouds have common macrophysical characteristics?***

The thesis is organized as follows, by addressing the main research questions in chapters 3, 4 and 5:

- ***Chapter 2*** describes the set up of the Barbados-Cloud-Observatory (BCO) and its instrumentation with a focus on the KATRIN cloud radar, as measurements from KATRIN are mainly investigated towards the onset of precipitation. Furthermore, the Advanced Spaceborne Thermal Emission and Reflection Radiometer (ASTER) is described briefly, whose measurements are studied in chapter 5 considering the macrophysical cloud properties.

- ***Chapter 3*** investigates the robustness and sensitivities of cloud radar measurements in the trades and tackles the question: ***Can measurements from a single location describe the variety of cloudiness in the trades?***

- In ***chapter 4*** the signature of KATRIN cloud radar echoes is used to investigate the impact of aerosols on the susceptibility of trade wind cumuli to form precipitation; answering the second research question: ***Can aerosols significantly alter the onset of precipitation of trade wind cumuli?*** Here, the sensitivity of the formation of rain is evaluated during conditions with high and low aerosol concentrations including a discussion if differences in the radar echoes could be simply explain during those conditions by small additional variations in the thermodynamic properties of the environment.

- ***Chapter 5*** considers the cloud cover and cloud size distribution of clouds in the trades using measurements of KATRIN and ASTER. The spatial distribution and degree of clustering is analyzed to address the question: ***Do precipitating clouds have common macrophysical characteristics?***

- ***Chapter 6*** closes the thesis with a summary of the main findings and an outlook.

Remark: Chapter 4 and chapter 5 are written in the style of a Journal publication and as such chapters contain their own introduction and conclusions. Chapter 4 was submitted to the Journal of the Atmospheric Sciences (Lonitz et al., 2013) and is included in this thesis with some editorial changes and omitting the abstract to make it consistent with other chapters of this thesis.

Chapter 2

Instruments and Data

This thesis aims to characterize micro- and macrophysical properties of shallow cumuli, and the precipitation that is associated with them. To study small changes in the microphysical properties of shallow cumuli, the high sensitivity of a cloud radar to the size of cloud droplets and their concentration in a volume of cloudy air is exploited. For investigating the impact of relative humidity and aerosol concentration on microphysical cloud properties, measurements by a Raman lidar are used. Additionally, back-trajectories are taken to characterize conditions of different aerosol concentration. The macrophysical properties of shallow cumuli, like cloud amount and cloud size distribution, are studied with measurements of the Advanced Spaceborne Thermal Emission and Reflection Radiometer (ASTER).

In this chapter, the characteristics and limitations of each instrument are described with a focus on the cloud radar measurements, as they are used extensively throughout this thesis, in particular in chapters 3 and 4. The other instruments, e.g. Raman lidar, are only shortly explained, as they complement the analysis of cloud radar measurements. After an introduction of the Barbados-Cloud-Observatory (BCO) in section 2.1, the cloud radar and the meaning of the most important measured quantities are described in section 2.2. A short description of the Raman lidar are given in section 2.3, before ASTER is described in section 2.4. The additional indicator of aerosol, the information about the history of arriving air masses at Barbados through an analysis of back-trajectories is sketched in section 2.5.

2.1 Barbados-Cloud-Observatory

The data from ground-based instruments used in this work was measured at the Barbados-Cloud-Observatory (BCO), which is located on the east coast of Barbados at 13° 09′ N, 59° 25′ W (Deebles Point, see Fig. 2.1). Barbados belongs to the Lesser Antilles and is located in the Atlantic ocean. Here, easterly trade winds prevail during most of the year and occupy the lowest atmospheric levels up to 3 km depth, although the marine layer itself is usually somewhat shallower. The location of the BCO is well suited for studies of the evolution and variability of clouds in the trades, which ranges from cumulus fractus over cumulus congestus to tropical thunderstorms. About 20 m away from the coast, the

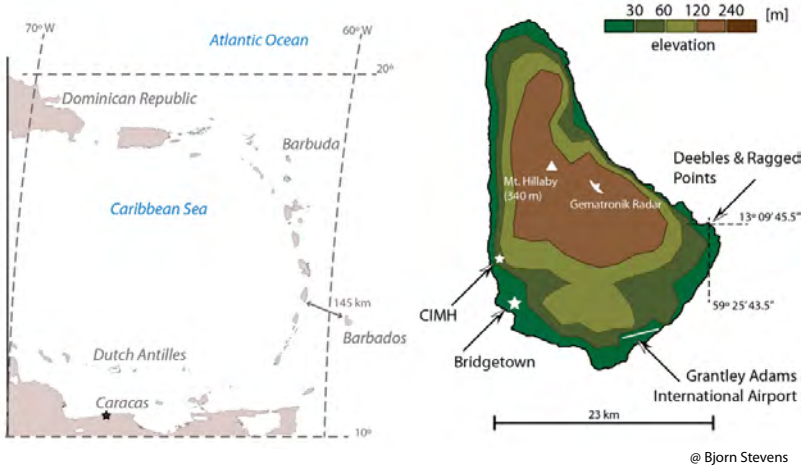

Figure 2.1: Geographical location of the Barbados-Cloud-Observatory (Courtesy: Bjorn Stevens).

instruments at the BCO measure clouds almost undisturbed by land, that move with the trades over the site from east north east.

The BCO has been developed by the Max Planck Institute for Meteorology and is maintained in cooperation with the Caribbean Institute for Meteorology and Hydrology (CIMH) in Barbados since April 2010. With a long-term data set from BCO, one is able to simultaneously measure the thermodynamic properties of the marine (sub-)cloud layer as well as the aerosol and clouds within the layer. Currently a weather sensor, a Raman lidar, the KATRIN cloud radar, a Micro Rain Radar (MRR), a ceilometer and an allsky-imager operate at the BCO, as shown in Fig. 2.2. In December 2010 the KIT cloud radar, borrowed from the Karlsruhe Institute of Technology, was replaced by the KATRIN cloud radar. Both cloud radars are 35.5 GHz polarized Doppler radars with scanning abilities. A full description of the site can be found in Stevens et al. (2013).

In this thesis, BCO measurements from the cloud radar characterizing microphysical cloud properties, relative humidity and aerosol measurements by the Raman lidar and measurements of rain by the MRR are used. A description of the MRR is omitted in this chapter, as the rain information is only needed by the Raman lidar to close its hatch during rain. As the focus of this work is on the BCO measurements by the KIT cloud radar and the KATRIN cloud radar in chapters 3 and 4, the characteristics of a cloud radar are described in detail in section 2.2, whereas only a short overview of the Raman lidar is given in section 2.3.

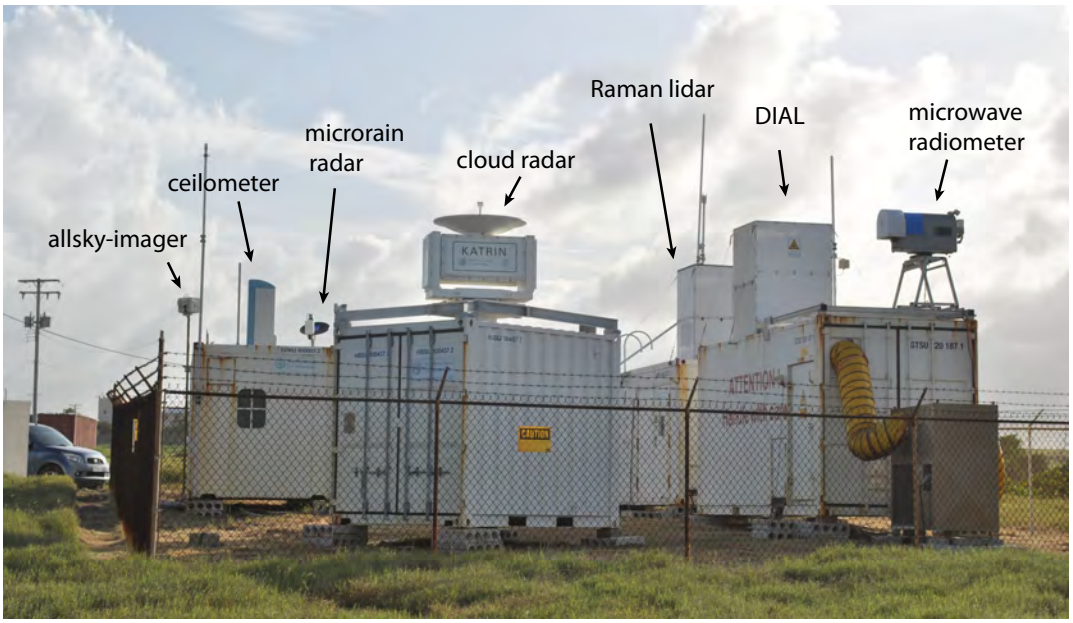

Figure 2.2: Picture of the Barbados-Cloud-Observatory with its instruments. The Differential absorption lidar (DIAL) and the microwave radiometer from the University Cologne have been deployed only for a few months in the past and are currently not under operation (Courtesy: Friedhelm Jansen).

2.2 Cloud radar

Cloud radar systems are active remote sensing instruments which can be used to study properties of hydrometeors, like cloud and rain droplets. The high resolution in time and range makes the cloud radar a powerful instrument for the observation of clouds in a detailed, continuous and unattended manner. Measurements by the cloud radar describe how deep clouds are and how many, differently sized rain and cloud droplets are moving up - or downward. The combination of the radar observables with observables from Raman lidar measurements and other ground based active remote sensing instruments, like ceilometers and microwave radiometer measurements, allows for studying the interplay of clouds, rain formation, aerosol concentration and thermodynamic conditions in a unique and highly resolved way. In chapter 4 we combine cloud radar and Raman lidar measurements to study the signature of aerosols and meteorology in the radar footprint. In this section, the basic principle of the cloud radar and the meaning of the measured quantities reflectivity, Doppler velocity and linear depolarization ratio are described.

2.2.1 Operation of cloud radar

Cloud radars emit electromagnetic pulses with a short wavelength λ into the atmosphere. This wavelength in the millimeter range sets the limit of Raleigh scattering which makes

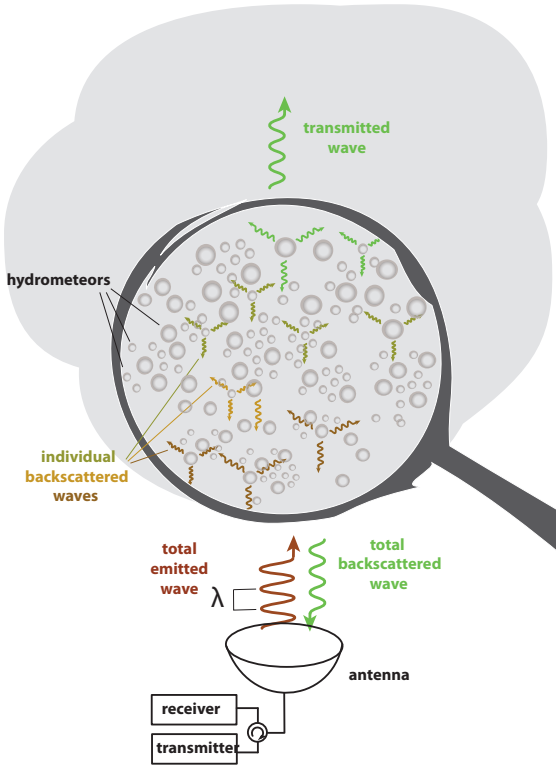

Figure 2.3: Sketch displays the operating mode of a cloud radar. Electromagnetic radiation with a well defined wavelength λ is emitted by the radar. The meteorological targets - here cloud droplets - which are in the line of sight of the radar, scatter the emitted waves. The sum of all directly backscattered signals are received by the radar antenna. Sketch modified after Melchionna (2010).

the cloud radar highly sensitive towards small hydrometeors, like cloud and small rain droplets, and ice particles which are much smaller than λ. If the emitted pulses hit targets, like cloud droplets, the wave is scattered elastically in all directions, as shown in Figure 2.3. This Raleigh scattering depends strongly on the wavelength of the radiation and the size (D) of the targets. That means the intensity of the scattered radiation varies proportional to λ^{-4} and D^6. For the configuration of the cloud radar used in this study, targets up to approximately 1 mm can be assumed to act as Raleigh scatterers (Melchionna, 2010). Cloud droplets are typically ten microns or a few tens of microns big, whereas drizzle may reach sizes of roughly a hundred microns. Larger sized drops are called raindrops, whose size is commensurate to the wavelength of the radiation emitted by the radar scatter in the Mie regime.

An advantage of the cloud radar with its operation at wavelengths in the microwave regime (i.e. wavelengths between 1 mm and 1 m) is its negligible dependency on the scattering caused by turbulent fluctuations of the refractive index of the air. Nevertheless, the cloud radar signal suffers to a small amount (less than 0.1 dB km^{-1}) from the absorption

by atmospheric gases (Grenzhäuser, 2012), and to a larger extent from heavy rain fall events when the signal becomes attenuated. In this study the interest is on the properties of shallow cumulus clouds and the precipitation connected to them and not on heavy rain fall events. The cloud radars employed for this study all have a frequency of 35.5 GHz (λ = 8.6 mm) and high power, which is tailed to the need to study the changes in microphysical properties of shallow cumuli.

Figure 2.3 illustrates the basic concept of the operation mode of a radar. The cloud radar antenna emits directed electromagnetic pulses of length τ with a well defined wavelength λ and one linear depolarization direction. The microwaves travel through the atmosphere and interact with meteorological targets, such as cloud and rain droplets, as well as with other targets, like insects and dust particles. The summation over all individual directly backscattered waves is then received again by the antenna. Due to the scattering of the emitted wave on randomly moving targets, the total backscattered signal has experienced a shift in phase and a change in its amplitude. The phase shift contains the information of the target's velocity relative to the radar.

(a) KIT. (b) KATRIN.

Figure 2.4: Images of the two cloud radars, used in this study (a) KIT and (b) KATRIN. (Courtesy: Friedhelm Jansen)

The change in the amplitude of the wave or in other words, the reflectivity Z, is proportional to the number concentration N and size of the hydrometeors D. A polarization filter inside the cloud radar antenna allows to receive the backscattered signals in the vertical and in the horizontal polarization plane. With the calculation of the ratio of both signals we able to infer about the geometrical shape of the observed targets. This ratio, named the linear depolarization ratio (LDR), is useful to differentiate between spherical cloud or rain droplets, which is of interest in the present study, and non-spherical insects or dust particles, which are useful to identify for the purpose of removing such signals. Next to the derivation of those microphysical properties the cloud radar measurements also allow to retrieve macrophysical properties, like cloud top height (z_t), which can be associated with the height of the most distant echo.

In this thesis, measurements from two linearly polarized Ka-band cloud radars: (i) KIT and (ii) KATRIN (see Fig. 2.4) are used. Both radars are Doppler radars, that means they possess the capability to retrieve the motion of the measured targets. Additionally, they are able to perform various scanning procedures. Both radars scan in 360° in azimuth with the KIT antenna scanning ± 45° in elevation and the KATRIN antenna scanning ± 90° in elevation. The KIT cloud radar (Grenzhäuser, 2012) operated from April 2010 until January 2011 at the BCO and was deployed in cooperation with the Karlsruhe Institute of Technology (KIT). The KATRIN cloud radar from the Max Planck Institute of Meteorology was deployed in December 2010 and has been measuring continually since then.

Table 2.1 describes the current configuration of KATRIN with more precision. The cloud radar KATRIN was named in memory of Katrin Lehmann, who past away before she could start her work in the project of the Barbados-Cloud-Observatory.

Table 2.1: Specifications of the KATRIN cloud radar in the set up on 24$^{\text{th}}$ of April 2013.

parameter	**value**
frequency	35.5 GHz
wavelength	8.6 mm
antenna diameter	1.2 m
beam width	0.52°
peak power of magnetron	30 kW
pulse repetition frequency PRF	5 kHz
pulse length τ	200 ns
integration time	0.1 s
averaging time	10 s
minimum range	300 m
maximum range	15 km
Doppler velocity resolution	0.08 m/s
FFT length	256

In this thesis, KATRIN measurements between January 2011 and March 2012 are used for further investigations in chapter 4. Due to problems with the air conditioning unit, most measurements have been recorded during the dry winter season as sketched in Fig. 2.5.

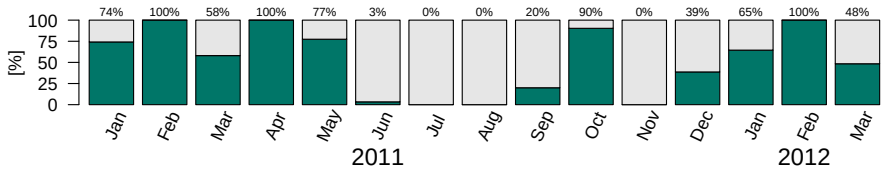

Figure 2.5: Schematic showing the monthly fraction of days (in green) when KATRIN was measuring between January 2011 and March 2012. Total fraction is outlined at the top of every bar.

2.2.2 Doppler spectrum

As mentioned already, KIT and KATRIN are capable to measure the motion of the targets relative to the radar, or in other words the radar can determine a shift in frequency (Doppler shift). This frequency shift happens when an electromagnetic wave hits targets moving toward or away from the radar and is known as the Doppler effect. As the cloud radar can only measure a small fraction of the Doppler shift within a pulse, it reconstructs the Doppler shift from phase changes of a series of pulses. A transformation of a timeseries of backscattered power gives the Doppler spectrum:

$$S(f_\mathrm{D}) = \int_{+\infty}^{-\infty} S_{f_\mathrm{D}}(f_\mathrm{D}) df_\mathrm{D}, \tag{2.1}$$

where $S_{f_\mathrm{D}}(f_\mathrm{D})df_\mathrm{D}$ represents the backscattered signal with a Doppler shift between f_D and f_D+df_D. Commonly, $S(f_\mathrm{D})$ is referred to as the Doppler spectrum of meteorological targets. Strong fluctuations in time can broaden the width of the spectrum (peak width), that is equal to the square root of the second central moment of the Doppler spectrum. Valuable insights into cloud microphysics can be obtained from the moments of the observed Doppler spectrum give, when it is assumed to be Gaussian-distributed (Fig. 2.6).

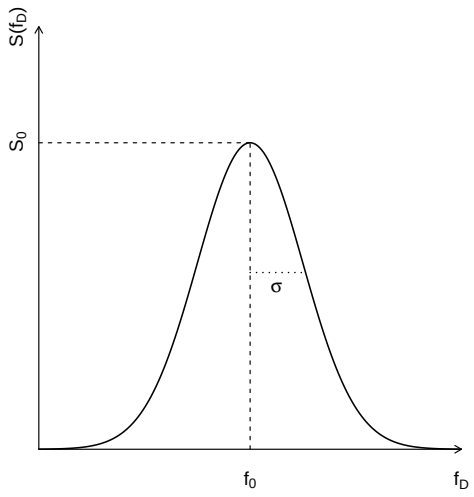

Figure 2.6: Schematic showing a gaussian distributed $S(f_\mathrm{D})$ with the maximum value S_0 for the mean f_0, and the standard deviation σ.

In this thesis the zeroth moment, the radar reflectivity factor (Z) of the particles in a volume of air, and the first moment, the mean Doppler velocity (v_D), of the continuous Doppler spectrum are used for the investigation of the susceptibility of shallow cumuli to form rain. Under the assumption that the mean air motion is small compared to motions by up- and downdrafts inside clouds, the Doppler velocity can be taken as a measure of developing clouds (section 4.3). In cases of downward directed velocities and large speed,

one can even use v_D as a measure of precipitation. A derivation of radar reflectivity factor is given in more detail in section 2.2.3, whereas the Doppler velocity is briefly outlined in section 2.2.4.

2.2.3 Radar reflectivity and radar reflectivity factor

To derive the radar reflectivity factor, one has to understand first how the cloud radar measures clouds, as illustrated in Figure 2.7 near Barbados. As mentioned before, the radar emits pulses of microwaves which are generated by a magnetron with a pulse repetition frequency (PRF) of 5 kHz (Table 2.1). The PRF is equivalent to the reciprocal of the time T between two consecutive pulses. The duration, τ, of a pulse determines the resolution of the range gate, which is 30 m in the current set up of the cloud radar (Table 2.1). The measurements of the cloud radar are therefore called range-resolved. With a limitation of 500 range gates the radar can measure up to an altitude of 15 km.

The time between emitted and received signal (t_s) determines the distance (x) of the targets and can be calculated with

$$x = \frac{2t_s}{c} \tag{2.2}$$

and the speed of light (c). The radar antenna emits electromagnetic pulses with the power (P_e) into one main direction. The effectiveness and directivity of the antenna can be measured by the antenna gain (G), which is a function of azimuth and elevation angle. For the circular paraboloidal reflectors of the KATRIN antenna, the maximum in the antenna gain is described by

$$G_0 = \frac{4\pi A}{\lambda^2}, \tag{2.3}$$

where A describes the effective aperture of the antenna. The power (P_e) is first received and then absorbed or scattered anisotropically by targets, that are located in beam direction. Targets at a distance (r) scatter some part of the received energy directly back to the antenna. This power can be described with

$$P_t = \frac{P_e}{4\pi r^2} G_0 \, \sigma, \tag{2.4}$$

where σ denotes the back-scattering cross-section. KATRIN receives and emits radiation with the same antenna in terms of the same effective aperture (A) as defined in Eq. (2.3), so that the backscattered power (P_b) can be expressed as:

$$P_b = \frac{P_t}{4\pi r^2} A. \tag{2.5}$$

For a single target in a volume (V) we can describe the backscattered power with

$$P_b = \frac{P_e {G_0}^2 \lambda^2}{(4\pi)^3} \frac{\sigma}{r^4}, \tag{2.6}$$

by inserting equations 2.3 and 2.4 into 2.5. Under real conditions, many targets are contained in a volume of air, as sketched in Figure 2.3. Signals from each individual

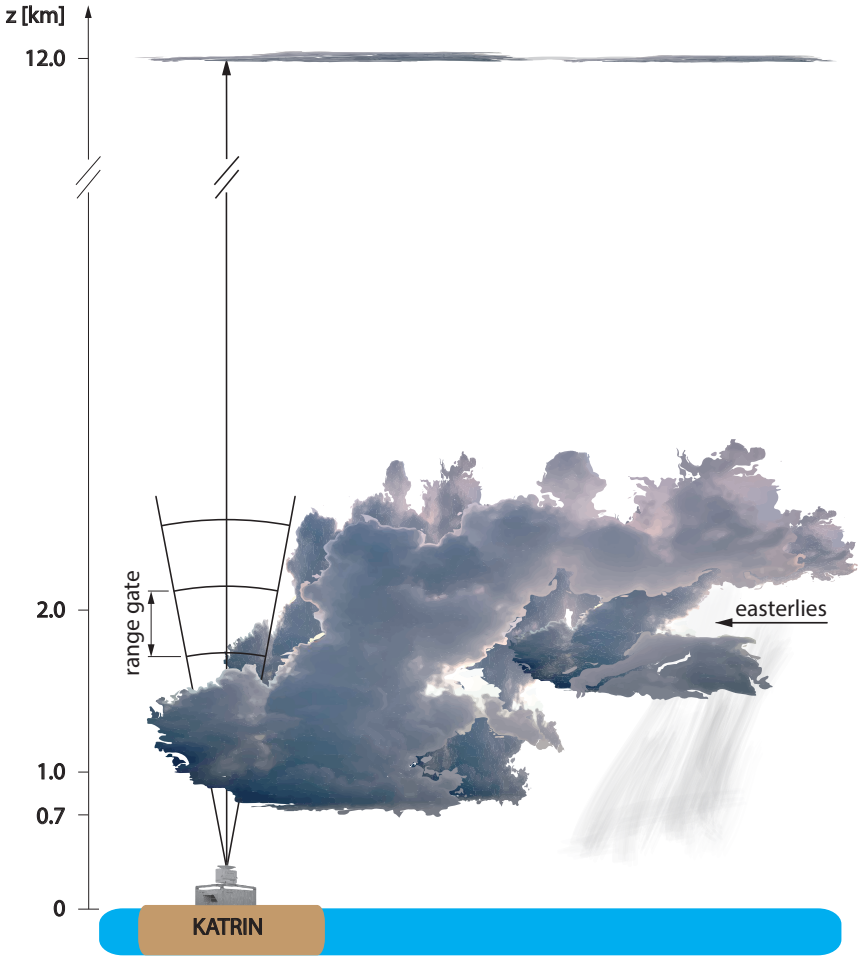

Figure 2.7: Basic representation how the cloud radar observes the variety in clouds at the East coast of Barbados. (Courtesy: Norbert Noreiks)

target contribute to the total backscattered signal. If the targets are spread over the whole contributing region the total backscattering cross-section $\sum \sigma_i$ is described by

$$\sum \sigma_i = \eta V, \tag{2.7}$$

where η is the radar reflectivity. The radar sampling volume (V) is defined as

$$V = \frac{\pi \theta^2 r^2 c\tau}{2^4 \ln 2}, \tag{2.8}$$

where θ is the azimuth angle [for more details see Melchionna (2010)].

Finally, power loss (L) in the signal by antenna characteristics and components of the receiver, like waveguides, have to be considered in the computation of backscattered power:

$$\begin{aligned} P_\mathrm{b} &= \frac{P_\mathrm{e} {G_0}^2 \lambda^2}{(4\pi)^3} \frac{\sum \sigma_i}{r^4} \frac{1}{L}, \\ &= \frac{P_\mathrm{e} {G_0}^2 \lambda^2}{(4\pi)^3} \frac{\eta \pi \theta^2 r^2 c\tau}{r^4 2^4 \ln 2} \frac{1}{L}, \\ &= \frac{P_\mathrm{e} {G_0}^2 \lambda^2 \theta^2 c\tau}{1024(\ln 2)\pi^2 L} \frac{\eta}{r^2}. \end{aligned} \tag{2.9}$$

Eq. (2.9) represents the radar equation for distributed targets. Note, that the backscattered power of a single target is inversely proportional to the fourth power of the distance (r), whereas the backscattered power (P_b) for a volume filled with targets is only inversely proportional to the square of distance. Additionally, P_b is directly proportional to radar reflectivity (η), which depends on the properties of the targets, like shape, size, number concentration and phase, or in other words how much energy is scattered back. Assuming spherical targets in a liquid phase with a size in which Raleigh scattering is prominent, the backscattering cross-section (σ_i) of a single target i can be described such that

$$\sigma_i = \frac{\pi^5}{\lambda^4} K_w^2 D_i^6, \tag{2.10}$$

where K_w is the dielectric factor and D the diameter of particles.

The resolution volume of KATRIN contains many thousands of liters of air, depending on the distance (r). One liter of cloudy air typically contains about 100.000 droplets. Hence, a continuous particle size distribution ($n(D)$) with many distributed particles can be assumed. To compute η, Equation 2.10 is inserted into Eq. 2.7 and is solved for η:

$$\eta = \frac{\pi^5}{\lambda^4} K_w^2 \int_0^\infty n(D) D^6 dD. \tag{2.11}$$

The right hand side of Equation 2.11 is called radar reflectivity factor (Z):

$$Z = \int_0^\infty n(D) D^6 dD, \tag{2.12}$$

and refers to spherical targets with a known size, only. Z does not depend on the settings of a radar system, that means one can compare Z from different radar systems.

Now, Eq. 2.9 can be rewritten as:

$$P_\mathrm{b} = \frac{P_\mathrm{e} {G_0}^2 \lambda^2 \theta^2 c\tau}{1024(\ln 2)\pi^2 L} \frac{\pi^5}{\lambda^4 r^2} K_w^2 Z, \tag{2.13}$$

incorporating the additional constants associated with the definition of the radar reflectivity in Eq. (2.11). The actual power (P_m) measured by the radar system is the sum of backscattered power (P_b) and receiver thermal noise power (P_n), which is described with:

$$P_\mathrm{n} = k_\mathrm{B} T_0 B F, \tag{2.14}$$

with the Boltsmann's constant $k_\mathrm{B} = 1.38 \times 10^{-23} J\,K^{-1}$, the standard temperature ($T_0 = 290\,K$), the receiver bandwidth $B = \tau^{-1}$, and the receiver noise factor (F). Herewith, the signal to noise ratio (SNR) is defined:

$$\mathrm{SNR} = \frac{P_\mathrm{b}}{P_\mathrm{n}} = \frac{P_\mathrm{m} - P_\mathrm{n}}{P_\mathrm{n}}. \tag{2.15}$$

Finally, the radar reflectivity factor can be is described as a function of SNR by solving Eq. 2.13 after Z. After replacing P_b with (P_m - P_n) and inserting Equation 2.15 we obtain:

$$\begin{aligned} Z &= \frac{1024(\ln 2)\pi^2 L}{P_\mathrm{e} {G_0}^2 \lambda^2 \theta^2 c\tau} \frac{\lambda^4 r^2}{\pi^5} K_w^{-2}\, P_\mathrm{n}\, \mathrm{SNR}, \\ &= \frac{r^2}{C} \mathrm{SNR}, \end{aligned} \tag{2.16}$$

with a constant C.

Because measurements of reflectivity can span many orders of magnitude, a logarithmic scale is often used for Z. When Z is given in SI-units the conversion can be done by normalizing Z with $Z^\bullet = 10^{18}\mathrm{m}^3$ before taking the logarithm with base 10 and multiplying by 10, thus defining the quantity dBZ:

$$\begin{aligned} \mathrm{dBZ} &= 10 \cdot \log_{10}\left(\frac{Z}{Z^\bullet}\right) \\ &= C_\mathrm{dB} + 20 \cdot \log_{10} r + \mathrm{SNR}_\mathrm{dB}, \end{aligned} \tag{2.17}$$

with the radar constant (C_dB) and $\mathrm{SNR}_\mathrm{dB} = 10 \cdot \log_{10}\left(\mathrm{SNR}(Z^\bullet)^{-1}\right)$.

As mentioned before, the reflectivity in equation 2.12 describes properties of hydrometeors under the assumptions of small spherical liquid particles (Rayleigh scatterers) which completely (and uniformly) fill the radar volume. A prior one cannot be sure that these assumptions are filled so the quantity, Z or dBZ is usually referred to as the equivalent radar reflectivity factor (Z_e). Only if all of the mentioned assumptions are met Z equals Z_e.

This thesis focuses on warm cumulus clouds with droplets in the liquid phase, being Rayleigh scatterers. If assuming numerous small droplets, Z can be approximated to be similar to Z_e. Throughout, the text Z, Z_e and dBZ are used interchangeably to denote reflectivity, and although they really describe the reflectivity factor, rather than the reflectivity (η) itself they are often referred to as reflectivity, because η is not further discussed.

Note, that the reflectivity is highly sensitive towards rain drops, because of its strong dependence to the diameter of particles D, as seen in Eq. (2.12). That means, the reflectivity of a radar volume filled with many small cloud droplets and a few large drops, either big cloud droplets or rain drops, would be mostly modulated by the few large drops. In that case, the backscattered power of many small particles is superimposed by the backscattered power of a few relatively big particles (Russchenberg and Boers, 2004). Only a few drizzle drops inside the cloud can superpose the total radar echo of all cloud droplets, making it

difficult to obtain the cloud base during times of evaporating rain or drizzle falling out of the cloud base. In this study, retrievals of rain drops are filtered out by identifying developing shallow cloud entities, as described in chapter 4.3.

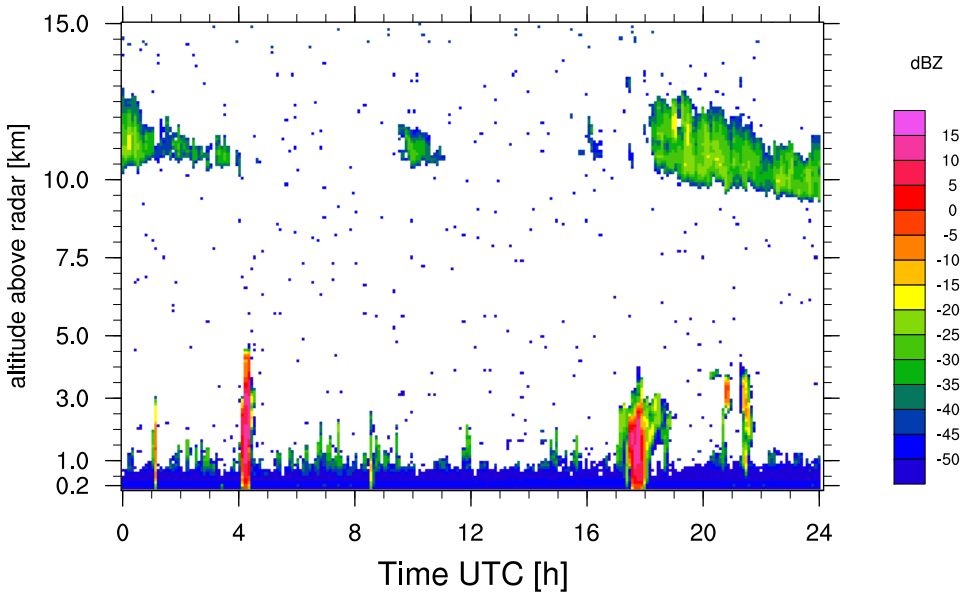

Figure 2.8: Six minute mean of dBZ measured by the KIT Radar on January 6$^{\text{th}}$ 2011, displayed as a function of height and time.

Fig. 2.8 gives an idea how the equivalent radar reflectivity factor behaves as a function of height and time for one day. On this day, high values in Z_e occur just after 4 UTC and between 17 UTC and 18 UTC marking precipitation falling out of convective clouds. Non-meteorological signals or spurious echoes can be seen in the low values of Z_e, occurring up to $\sim$ 700 m. This "clutter" is mostly an effect of the side lobes and has to be filter out before analyzing the data, as discussed in chapter 3.

2.2.4 Doppler velocity

Cloud and rain droplets are constantly moving, or at least being influenced, by the mean wind. For convective clouds this can have a significant vertical component. When the emitted radiation hits particles within the radar volume, each individual backscattered signal superposes linearly to a total echo. As a result of the random movements by the particles, only the amplitude and phase of the total backscattered wave differ from the emitted wave. As mentioned before, this phase change contains the information about the velocity of the moving targets. With the transformation of a timeseries of backscattered powers, a Doppler spectrum of particle cross sections can be created where every cross

section σ_i refers to a Doppler shift in frequency (f_D):

$$f_\mathrm{D} = \frac{2v_D}{\lambda}, \tag{2.18}$$

where v_D is the Doppler velocity, which is the radial component of the targets' velocity in the line of sight of the radar. The radial velocity depends on the wind's velocity and the sedimentation or fall velocity of the targets. In this study, only retrievals are used during times when the cloud radar operated in the vertical pointing mode. This makes v_D to a measure of the vertical velocity, which is the sum of the particles terminal fall velocity and the vertical air motion. The direction of the moving particles determines the sign of v_D, with falling particles having a negative v_D.

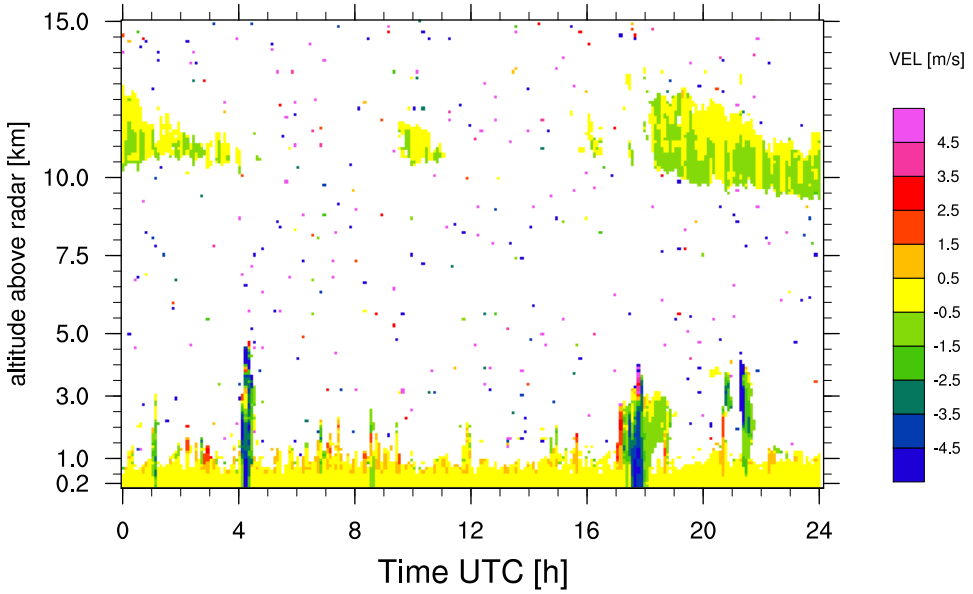

Figure 2.9: Six minute mean of v_D measured by the KIT Radar on January 6$^{\mathrm{th}}$ 2011, displayed as a function of height and time.

Fig.2.9 displays the daily evolution of Doppler velocity for the same day as displayed in Fig. 2.8. The clutter is characterized by values around 0 m s^{-1}, whereas the precipitation has strong negative values with v_D approaching -5 m s^{-1}. Note, a large raindrop can fall with a speed of 9 m s^{-1}. Values of v_D close to 0 m s^{-1} can also be found for the cirrus clouds near 11 km, which have dBZ values of around -25 in Z_e (Fig.2.8), which is much higher than the clutter in the subcloud layer.

2.3 Raman lidar

The Raman lidar, as shown in Fig. 2.10, is useful for providing information about the vertically resolved aerosol concentration, as well as temperature and humidity (only during

nighttime). The lidar is an active remote sensing instrument, emitting laser pulses with a specific wavelength and receiving the energy backscattered by particulate matter and molecules. Detecting backscatter at the same wavelength as the emitted laser light, i.e. elastic scattering, is done with elastic or backscatter lidars. The specific characteristic of a Raman lidar is the detection of the backscattered electromagnetic radiation at wavelength that differ from the wavelength of the emitted laser pulse. This allows to measure the inelastic response (or Raman effect) of molecular scattering, in addition to the elastic response. During the scattering process some molecules transit from one energy state to another, causing a frequency shift of the scattered light, known as the Raman effect. The changes in energy levels are quantized, and depend on the nature of the molecule and the transition induced. For example, to detect the water vapor mixing ratio in the atmosphere the property of water molecules is used, wherein incident radiation with a wavelength of λ = 355 nm is scattered back with a wavelength of λ = 407.5 nm. For more details on the operation of a Raman lidar please see Nicolae and Talianu (2010).

In our setup, all Raman lidar profiles have a range resolution of 60 m up to 15 km and are averaged over a time of two minutes. The Raman lidar hatch stays closed during times when the sun is directly overhead (11:30 - 13:30 local time during April and August) or when rain is measured at any height below 3 km by the micro-rain radar, as for example at 4 UTC, seen in Fig. 2.11 and Fig. 2.8. Additionally, only Raman lidar profiles outside clouds are considered.

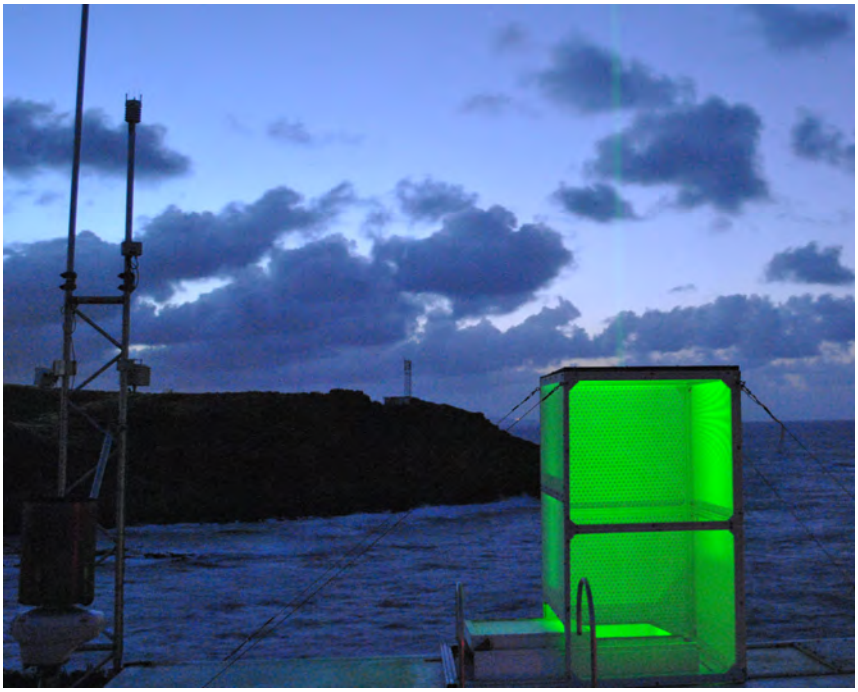

Figure 2.10: View of the green laser beam from the operating Raman lidar at the BCO. In the background Ragged Point with the AERONET station is visible. (Courtesy: Björn Brügemann and Ilya Serikov.)

To identify days with different aerosol concentration two observables from the Raman lidar are used; the particle backscatter and the linear-depolarization ratio. The particle backscatter describes the amount of backscattered energy by particles only, which depends on particle size, refractive index and the concentration of the scatterers. Measurements of atmospheric depolarization give information about the shape of the particles in the atmosphere, specifically the asymmetry. Here, the linear depolarization ratio quantifies the degree of polarization. Fig.2.11a and Fig.2.11b give an idea how those two observables behave as a function of height and time for one day, respectively.

Higher values in particle backscatter and linear depolarization ratio can be found up to 3 km height after 19 UTC compared to the rest of the day. This feature could be explained by the arrival of higher aerosol concentrations. Fig.2.11c shows the water vapor mixing ratio, which is computed using the ratio of the vibrational Raman backscatter of water vapor and nitrogen molecules. It can be converted to relative humidity by considering the measured temperature. Here, a relatively homogenous vertical evolution of water vapor mixing ratio with higher values can be seen after 22 UTC up to 4 km. The effect of small changes in relative humidity is investigated in chapter 4.6.

Because the Raman lidar only provides relative humidity data at night, evidence of a diurnal cycle was searched for, both in the cloud radar data and through measurements with a coincident differential absorption lidar (DIAL) system, which provided daytime humidity profiles over a few weeks of coincident operation. However a pronounced diurnal cycle, such as seen over and downwind of the island, is not evident at the site, which is only tens of meters from the upwind edge of the island, as stated in chapter 2.1.

2.4 ASTER

With scenes of 60 km x 60 km from the Advanced Spaceborne Thermal Emission and Reflection Radiometer (ASTER) on board the Terra spacecraft[2] we are able to study the macrophysical properties and organization of shallow cumulus clouds from space. Fig. 2.12 displays an example of the variety of such clouds within one scene from January 6$^{\text{th}}$ 2011, with numerous small clouds on the western side of the scene and a few large clouds on the eastern side. In the sub-sampled cloud field the fine differences in the texture of the clouds are visible and when the sea is very rough even the crests of waves can be seen (not shown).

ASTER is a joint effort between Japan's Ministry of Economy, Trade and Industry (METI) and NASA, including scientific and industrial organizations in both countries. The operational purpose of ASTER is to provide high spatial resolution imagery, which can be used to discriminate amongst a large variety of surface materials, ideal for studies of geology and soils, vegetation and ecosystem, land surface climatology, hydrology, and

[2]The Terra spacecraft is part of NASA's Earth Observing System (EOS). It is a polar-orbiting satellite on a 98° inclination, 705 km altitude sun-synchronous orbit, with and equator crossing of 10:30 am local solar time. Other instruments on board are the Moderate-Resolution Imaging Spectroradiometer (MODIS), Multi-angle Imaging SpectroRadiometer (MISR), Clouds and the Earths Radiant Energy System (CERES), and Measurements of Pollution in the Troposphere (MOPITT).

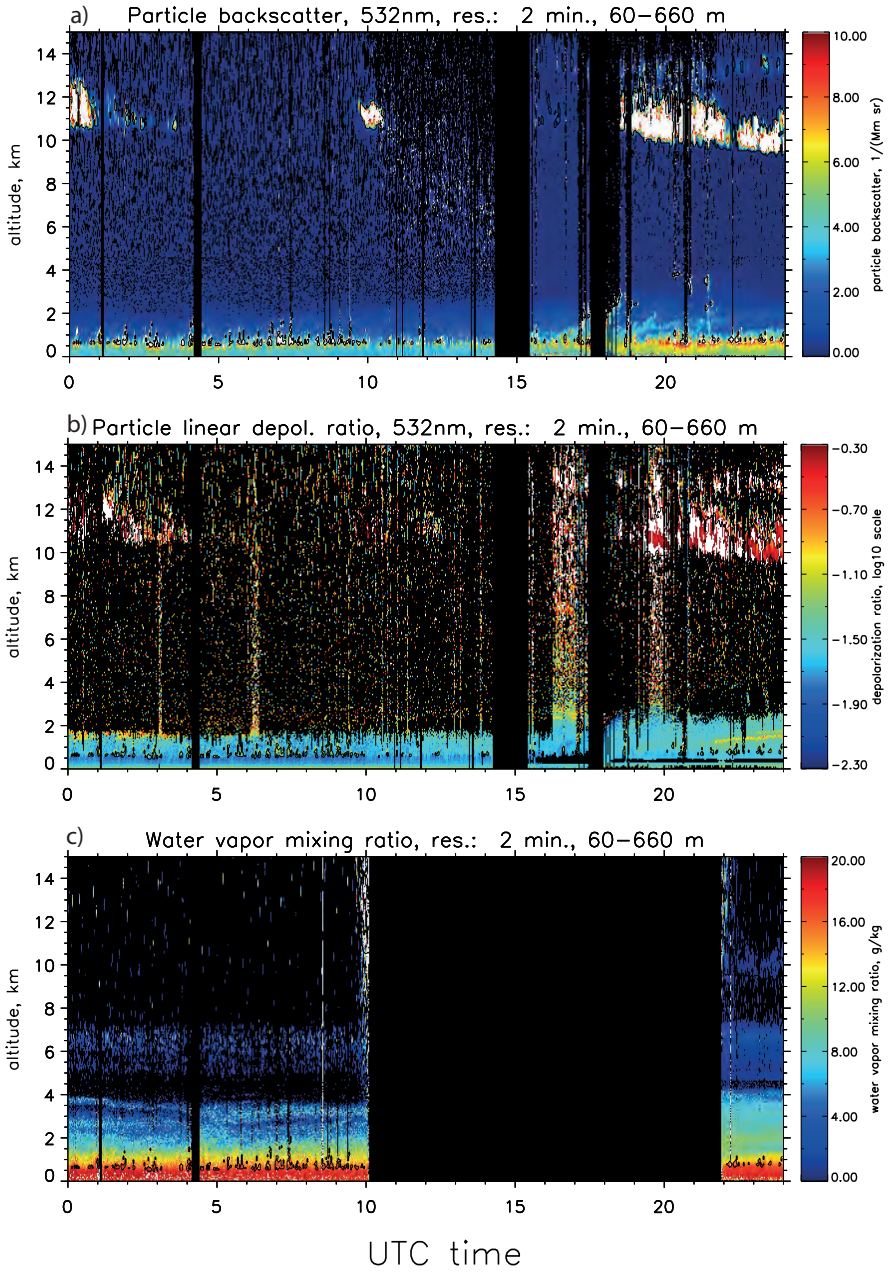

Figure 2.11: Two minute means of a) particle backscatter at $\lambda = 532\,\text{nm}$, b) particle linear depolarization ratio at $\lambda = 532\,\text{nm}$ and c) water vapor mixing ratio measured by Raman lidar on January 6$^{\text{th}}$ 2011, displayed as a function of height and time. Black vertical stripes mark times when no measurements were obtained, as for example during times of precipitation (for example at 4 UTC, also visible in Fig. 2.8) or direct sun overhead. The water vapor mixing ratio can only be measured during night time.

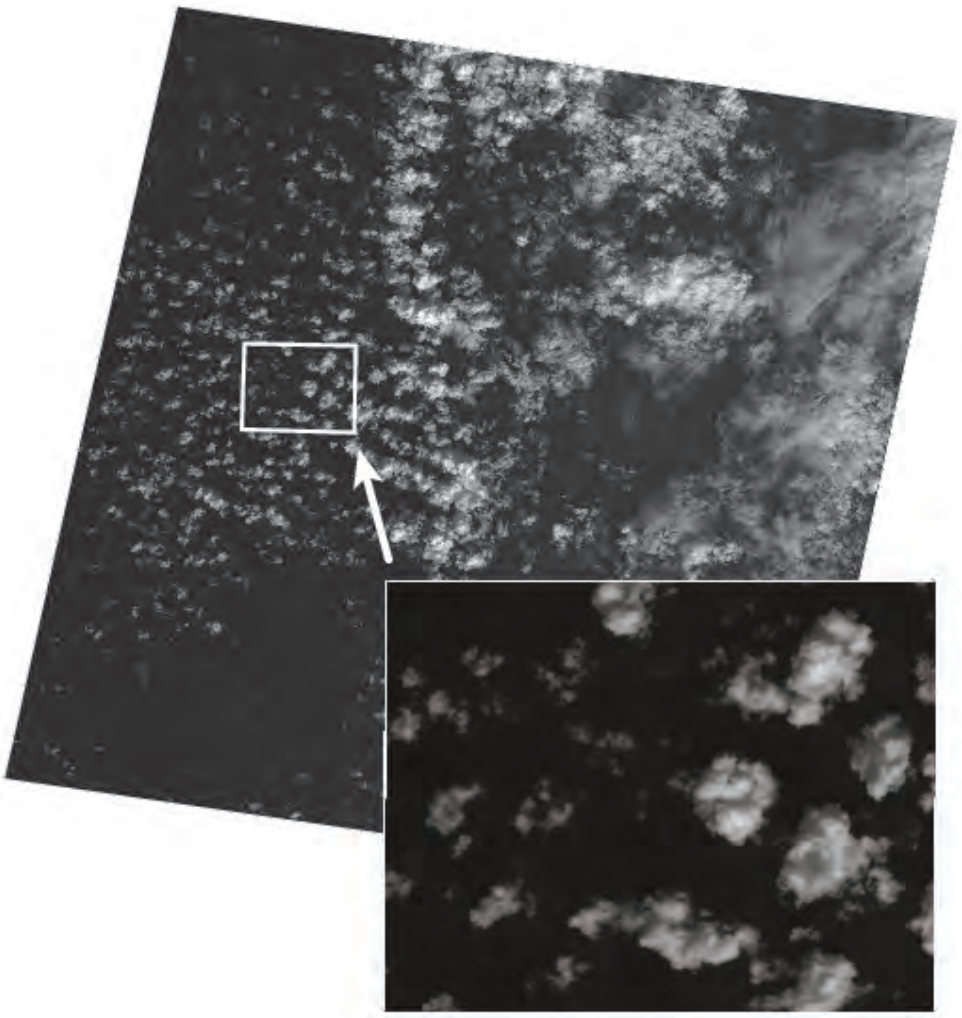

Figure 2.12: ASTER snapshot close to the BCO on January 6$^{\text{th}}$ 2011 at 14:05 UTC, observed in the visible channel 1 from the Level 1B product. In the right left corner a sub-sample of the whole cloud field is displayed, showing the capability of ASTER to retrieve different textures of clouds.

land cover change. Nevertheless, we can take advantage of the high spatial resolution of reflectance and brightness temperature from observed clouds to study, for example cloud cover and cloud size, and their organization in the trades.

The advanced multispectral imager ASTER covers a range of wavelengths from the visible to the thermal infrared with 14 bands. Additionally, it has one near-infrared camera that looks backward to provide stereo coverage. ASTER has three bands in the visible and near-infrared (VNIR: 0.52 μm to 0.86 μm), plus a backward telescope, six bands in the

short wave infrared (SWIR: 1.60 μm to 2.43 μm), and five bands in the thermal infrared (TIR: 8.13 μm to 11.65 μm). In the visible and near-infrared the spatial resolution is 15 m, in the short wave infrared 30 m, and in the thermal infrared 90 m. In this work, we use data from channel 3N and channel 14 to distinguish clouds from ocean and low-level clouds from high-level clouds, respectively. Channel 3N is part of the VNIR subsystem and covers the spectral range from 0.76 μm to 0.86 μm, whereas channel 14 is part of the TIR subsystem covering the spectral range from 10.95 μm to 11.65 μm. The VNIR subsystem has both a nadir and backward looking telescope, which are calibrated on-board with two independent calibration devices for each telescope. This procedure allows for an absolute radiometric accuracy of $\pm$ 4% or better. In this study, we only use nadir VNIR imagery. The TIR subsystem has one fixed telescope with pointing and scanning done by a mirror. For calibration, the mirror rotates 180° from the nadir position to view an internal heated or cooled black body. For further details on ASTER see Yamaguchi et al. (1998).

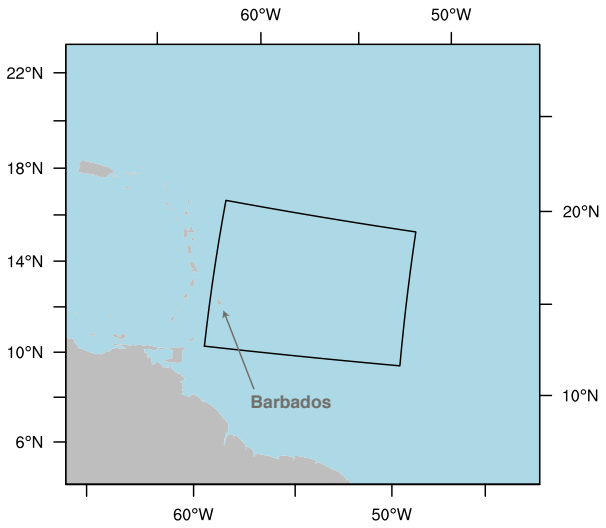

Figure 2.13: Map shows Caribbean islands, marking the region (black bounding box) for which ASTER data was retrieved in 2011. The bounding box measures: 18°N - 11°N and 60°W - 50°W. Barbados is located inside the bounding box and the other Caribbean islands outside of it. Blue colors mark ocean and gray colors land.

ASTER data are stored in two different types of Level-1 formats: Level-1A (L1A) and Level-1B (L1B). L1A is the reconstructed, unprocessed, and fully resolved instrument data, consisting of image data, radiometric and geometric coefficients, and other auxiliary data without applying the coefficients to the image data. We use the L1B product, which applies these coefficients to obtain radiometrically calibrated and geometrically resampled instrument data. In this study, ASTER data is investigate of one year (December 21$^{\text{th}}$ 2010 to December 13$^{\text{th}}$ 2011) for a region around Barbados (bounding area: 18°N - 11°N and 60°W - 50°W), as displayed in Fig. 2.13. In total 1500 ASTER scenes were obtained from the Land Processes Distributed Active Archive Center (LP-DAAC).

2.5 Back-trajectories

The back-trajectories used in chapter 4 give information about the origin of the arriving air masses in Barbados. We use the Hybrid Single Particle Lagrangian Integrated Trajectory Model model (HYSPLIT) to calculate 10-day back-trajectories, and hence to differentiate between maritime and continental air masses, which is used as an indicator of aerosol concentration. The initial development of HYSPLIT originates from a cooperation between NOAA and Australia's Bureau of Meteorology. For more details see http://ready.arl.noaa.gov/HYSPLIT.php.

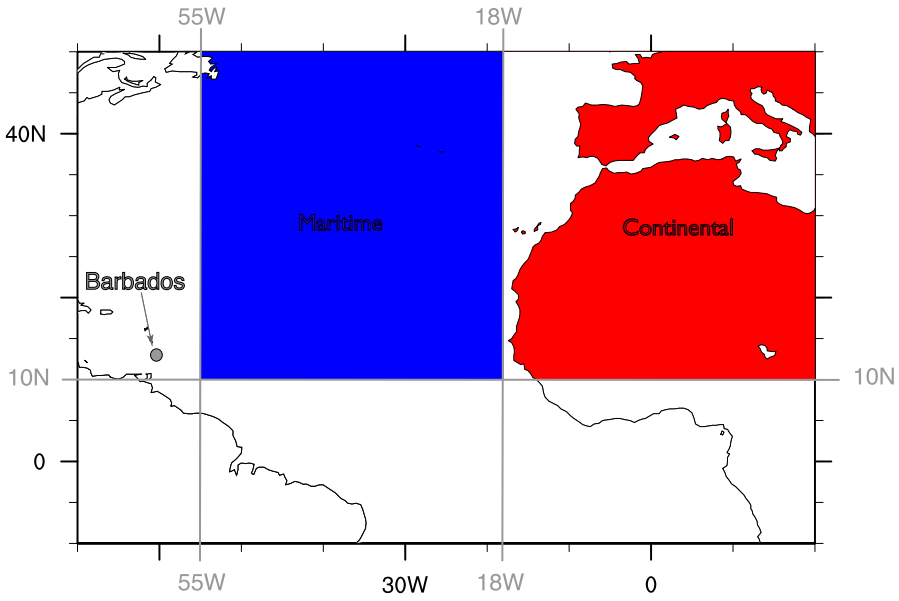

Figure 2.14: Map of air mass' origin. In blue the origins of maritime air masses are highlighted and in red continental air masses.

Air masses are defined continental if during a period five to ten days before arriving at the measurement site the airmass was estimated to have been over any of the continental areas north of 10°N (see Fig. 2.14). Air masses are defined as maritime when the airmass never crossed land during the 10 days prior to arriving at the measurement site. Here, 10-day back-trajectories are estimated using HYSPLIT [e.g. Draxler and Hess (1997)] forced by ERA-Interim reanalysis data, run every 6-hours. The motivation to do so developed from a study undertaken by Dr. Heike Wex and Co-authors (see appendix). They sampled probes in two field campaigns CARRIBA1 and CARRIBA2 at Ragged Point (Siebert et al., 2013), close to the BCO, and identified correlations between probes with dust and the air mass destination computed with back-trajectories.

Chapter 3

Robustness of cloud radar retrievals

In January 2011 the KIT radar, borrowed from the Karlsruhe Institute of Technology, was finally replaced by the new KATRIN cloud radar. To use measurements from both radars and to test if the instruments have specific sensitivities, radar retrievals are compared with each other. For a three week period between 22 December 2010 and 9 January 2011, the two cloud radars, KIT and KATRIN, measured parallel at a distance of 150 m at the BCO in a vertically pointing mode. This set up allows to study the differences and sensitivities of the two radar systems to the environmental conditions in a detailed manner, as done in the first section of this chapter (section 3.1). Here, differences in the retrievals caused by different hardware and software are analyzed. To investigate if the clouds measured at the BCO describe the variety in cloudiness within the trades, the radar retrievals of the different elevation angles are compared with each other (section 3.2). A final conclusion about the further treatment of the cloud radar data in this study is stated in section 3.3.

3.1 Intercomparison of the two cloud radars

The two cloud radars, KIT and KATRIN, are both linear polarized Doppler Ka-band cloud radars and are able to scan at different elevation and azimuth angles. They agree in most parts of their construction, but the following items are different:

- Both cloud radars have different side lobe characteristics, due to different designs of the reflector of their Cassegrain-antennas[3]. In December 2011 the feed of the KATRIN antenna was replaced, which improved the side lobe characteristics. In November 2012 the antenna of KATRIN was replaced by a Cassegrain-antenna, having a better side lobe characteristic.

- The cloud radars have different scanning procedures. KIT has a minimum elevation angle of 45° above the ground and KATRIN a minimum elevation angle of 5°.

[3]http://en.wikipedia.org/wiki/Cassegrain_antenna

- The cloud radars use different software in processing data.

After comparing the radar observables from both radars (section 3.1.1), the differences in hardware (section 3.1.2) and software (section 3.1.3) are discussed.

3.1.1 Differences in radar observables

To investigate possible differences between radar observables of KIT and KATRIN, we compute statistics of collocations between KIT and KATRIN. Collocations are found when a retrieval of KATRIN was measured within a time window of 10 s of a KIT retrieval that was closest in time. Fig. 3.1 shows the frequency of occurrence of collocations between KATRIN retrievals (y-axis) and KIT retrievals (x-axis). If both radars agree perfectly, all retrievals can be found on the one-to-one-line in black. Differences in the four cloud radar observables: reflectivity (0^{th} moment of N, see Fig.3.1a), Doppler velocity (1^{st} moment of N, see Fig.3.1b), peak width ($\sim 2^{\text{nd}}$ moment of N, see Fig.3.1c) and linear depolarization ratio (see Fig.3.1d) are shown.

To quantify the differences in the measured variables, the mean difference (MD), the root mean square difference (RMSD) and the correlation (CORR) are computed. MD is the mean of a difference between two retrievals (see Eq.3.1), whereas the root mean square difference (RMSD) is simply the standard deviation of the difference, as shown in Eq.3.2. The term correlation refers to the linear Pearson correlation coefficient, which defines the ratio of the covariance of the sample populations to the product of their standard deviations (see Eq.3.3). In all three equations x equals KIT, y equals KATRIN and M the number of collocations.

$$\mathrm{MD} = \frac{1}{M}\sum_{i=1}^{M}(x_i - y_i) \tag{3.1}$$

$$\mathrm{RMSD} = \sqrt{\frac{1}{M-1}\sum_{i=0}^{M-1}\Big((x_i - y_i) - \mathrm{MD}\Big)^2} \tag{3.2}$$

$$\mathrm{CORR} = \frac{\text{covariance of X and Y}}{(\text{standard deviation of X})(\text{standard deviation of Y})} \tag{3.3}$$

$$= \frac{\frac{1}{M-1}\sum_{i=0}^{M-1}\left(x_i - \left[\sum_{k=0}^{M-1}\frac{x_k}{M}\right]\right)\left(y_i - \left[\sum_{k=0}^{M-1}\frac{y_k}{M}\right]\right)}{\sqrt{\frac{1}{M-1}\sum_{i=0}^{M-1}\left(x_i - \left[\sum_{k=0}^{M-1}\frac{x_k}{M}\right]\right)^2}\sqrt{\frac{1}{M-1}\sum_{i=0}^{M-1}\left(y_i - \left[\sum_{k=0}^{M-1}\frac{y_k}{M}\right]\right)^2}}$$

In general, the differences between KIT and KATRIN in the three moments are small, in particular the Doppler velocity agrees almost perfectly with MD = $0.000\,\mathrm{m\,s^{-1}}$ and RMSD = $0.036\,\mathrm{m\,s^{-1}}$. The reflectivity measured with KATRIN is on average about dBZ

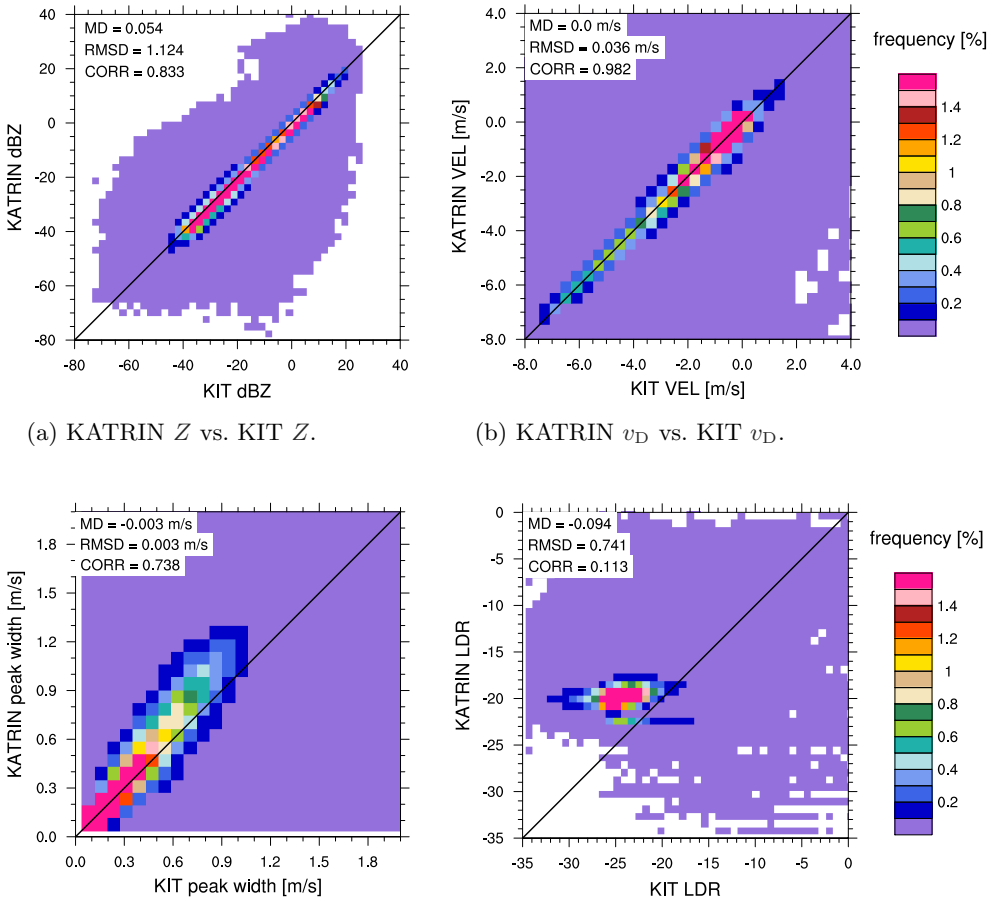

(a) KATRIN Z vs. KIT Z.

(b) KATRIN v_{D} vs. KIT v_{D}.

(c) KATRIN peak width vs. KIT peak width.

(d) KATRIN LDR vs. KIT LDR.

Figure 3.1: Frequency of occurrence of KATRIN quantities vs. KIT quantities using the dataset from 22 December 2010 to 9 January 2011.

= 0.054 ±1.124 smaller than the reflectivity measured with KIT, and the peak width measured with KATRIN is slightly higher (MD = -0.003 m s^{-1}). The largest differences between KIT and KATRIN can be found in LDR, whereas KIT shows a larger spread in LDR than KATRIN. As defined in chapter 2.2.1, the LDR is the ratio of radiation received in the cross-channel to the radiation received in the co-channel. The co-channel receives only radiation in the horizontal polarization plane, whereas the cross-channel receives only radiation in the vertical polarization plane. The reason for the smaller spread in LDR of KATRIN, and hence the low correlation between KIT and KATRIN of 0.113 is based in the reduced hardware sensitivity of KATRIN in the cross-channel of about dBZ = 3, leading to more similar LDR values.

This thesis concentrates on the increase of reflectivity with height and uses the information about the Doppler velocity (chapter 4). Because the differences are rather small

in those two quantities, the analysis is not biased towards different sensitivities in LDR of the cloud radars, KIT and KATRIN. Nevertheless, only collocation between KIT and KATRIN are considered in this section, that means retrievals of KATRIN are excluded for which no collocations with KIT have been found (and vice verse for KIT). Differences between all retrievals of KIT an KATRIN are discussed in the next section.

3.1.2 Detection of non-meteorological radar retrievals and other spurious echoes

To study the sensitivity in the reflectivity (Z) retrieval by KIT and KATRIN it is useful to look for differences in the time-height cross sections of reflectivity, as displayed for 6 January 2011 in Fig. 3.2. Just a visual comparison of KIT and KATRIN retrievals reveals many similarities, as for example detecting same values of Z of high cirrus clouds and precipitating cumulus clouds, as well as major differences, as for example the detection of numerous small reflectivity values by KATRIN up to a height of 1.5 km. These differences in reflectivity result from different hardware (design of antenna) and software of the two radar systems. For example, the antennas of the two radars introduce different "clutter" sensitivities resulting in detecting small reflectivity values in lower heights for KATRIN. This clutter is mostly an effect of the side lobes and therefore a non-meteorological signal or spurious echo, that has to be removed before analyzing the data.

In general, a radar antenna does not completely emit the radiation into one direction. That means a minor part of the radiation is sent out with angles of 0 ° and 60 ° with respect to bore sight; these effects are denoted as side lobes. Interactions with the underground or sea are due to the 0 ° side lobe. The consequence is ground clutter, characterized by a sharp peak in the power spectrum with a Doppler velocity of about 0 m s^{-1}. Heavy precipitating systems can be seen through the signals of the 60 ° side lobes, which detect the ground based precipitation from an approaching or departing cloud, before or after the cloud is seen by the main lobe. An example for the clutter caused by the 60 ° side lobe is shown in Fig. 3.2b at 17:30 UTC in about 4 km height. The main characteristics of all clutter are the small values in Z. Setting a minimum reflectivity, at which the signal is assumed as clutter free, helps to remove non-meteorological features and other spurious echoes in the radar retrieval. The caveat of this procedure is the elimination of real weak hydrometeor signals. Hence, one has to analyze to what extent radar retrievals of clouds change with a minimum detectable reflectivity ($\mathrm{dBZ_{min}}$) for both radars, KIT and KATRIN.

Fig. 3.3a shows how the projected hydrometeor cover (hereafter "cloud cover") varies as a function of $\mathrm{dBZ_{min}}$ for retrievals up to a height of 5 km. This height exceeds the maximum height up to which most of the clutter is contained in the radar retrieval. The cloud cover for KIT increases from 21% for $\mathrm{dBZ_{min}}$ = -35 to 99% for $\mathrm{dBZ_{min}}$ = -55, whereas the cloud cover for KATRIN increases from 18% for $\mathrm{dBZ_{min}}$ = -35 to 88% for $\mathrm{dBZ_{min}}$ = -55. This poses two questions: Can we simply choose a threshold to distinguish between clutter and real signal? What is a sensible threshold in Z in order to obtain a realistic cloud cover which is typical for the trades?

Instead of using a threshold in Z to filter out clutter, one could also consider reflectivities that have a low LDR, as those retrievals are characterized by a volume of air filled

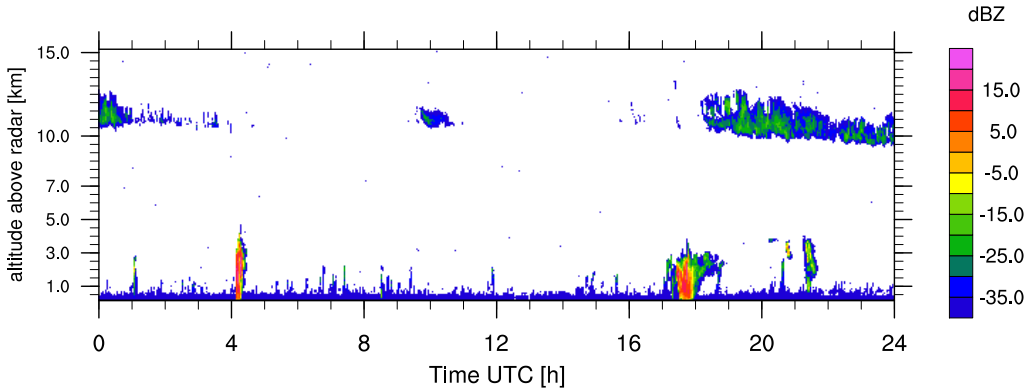

(a) Unfiltered retrievals of Z by KIT.

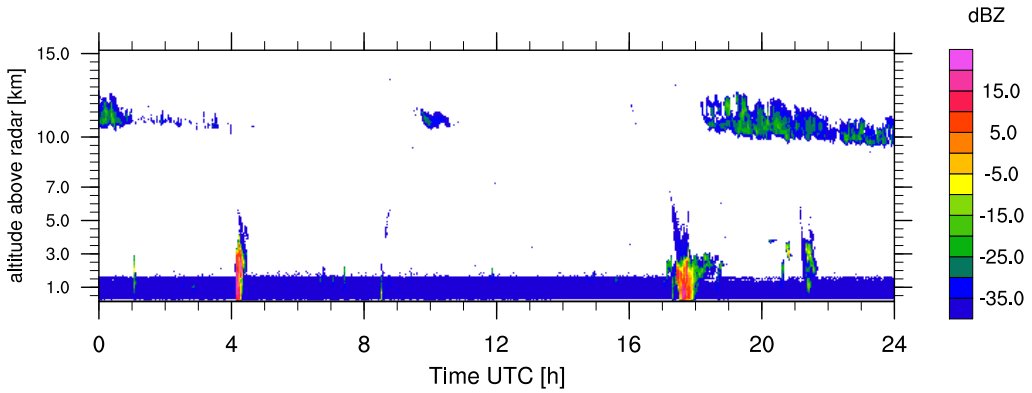

(b) Unfiltered retrievals of Z by KATRIN.

Figure 3.2: Time-height cross section of reflectivity for both cloud radars operating in the vertically pointing mode on 6 January 2011. Here, no lower limit for Z is applied.

with spherical hydrometeors such as cloud and rain drops. For example, when taking a LDR < -10 the cloud cover reaches a constant level at 24% for KIT and 19% for KATRIN for very small reflectivity values (see dashed lines in Fig. 3.3a), which seems to be a more realistic value for cloud cover than $\sim$ 80% (Nuijens et al., 2013). Filtering retrievals according to LDR would allow to keep retrievals with a low value in reflectivity. A large amount of low reflectivity values measured with KATRIN, however, do not have a value in LDR, because no signal in the cross-channel could be measured, which is needed for the computation of LDR.

Hence, choosing a threshold in Z seems to be a reasonable approach to filter out clutter without loosing too many real retrievals. Fig. 3.3b displays the linear correlation between signals from KIT and KATRIN and the number of signals as a function of $\mathrm{dBZ}_{\mathrm{min}}$. To compute the linear correlation, collocations between KIT and KATRIN are found. By identifying a minimum detectable threshold in Z at which the retrievals of KIT and KATRIN correlate well, would allow to set a sensible threshold. A high correlation of

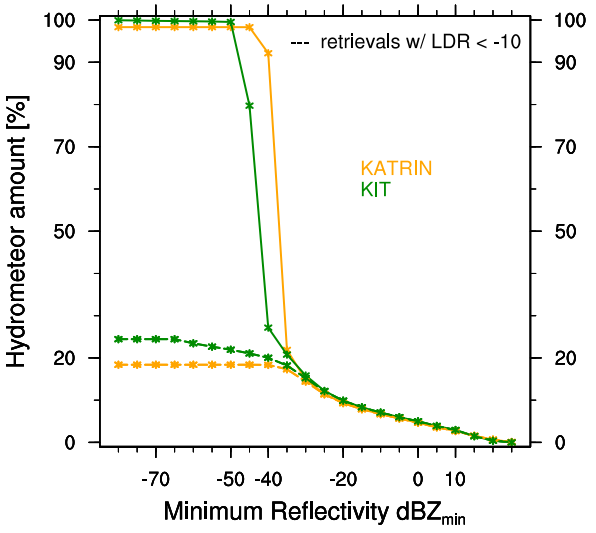

(a) Projected hydrometeor cover dependent on dBZ_{min} up to 5 km.

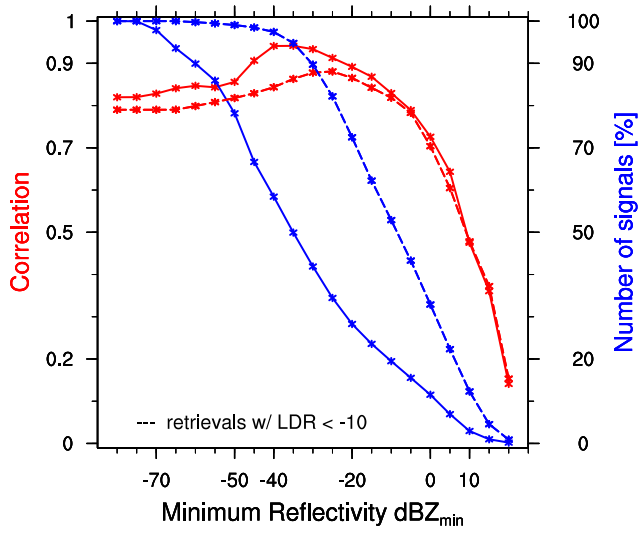

(b) Correlation between the two radars dependent on dBZ_{min} up to 5 km.

Figure 3.3: Dependencies of cloud amount (a) and correlation (b) on the minimum reflectivity dBZ_{min} which is allowed to occur for retrievals up to 5 km using the vertically pointing mode for the measurements period from 22 December 2010 to 9 January 2011. Solid lines refer to all retrievals and dashed lines only to retrievals with a LDR < 10.

about 0.94 is found for dBZ_{min} = -35 with a high reduction in the number of signals by 51% to the total number. Yet, a large amount of the received signals is due to clutter, that means this high reduction in the number of samples is consistent with filtering out clutter. The threshold of dBZ_{min} = -35 is found to be a good trade-off for giving a realistic cloud cover (see Fig. 3.3a) and a high correlation between the radar retrievals (see Fig. 3.3b), but still including enough data from our original dataset. Therefore, radar retrievals with dBZ_{min} = -35 are found to be representative for clutter-free signals.

A good example how well the two cloud radars agree when considering only signals above this threshold is displayed in Fig. 3.4. Here, the time-height cross-section of reflectivity is shown for the two cloud radars for 6 January 2011 with dBZ_{min} = -35. The clutter retrieved by KATRIN up to a height of 1.5 km disappeared. Nevertheless, in cases of heavy precipitation events, as for example at $\sim$ 17:30 UTC, the effect of the 60 ° side lobes for KATRIN is still visible, as seen when comparing Fig. 3.4a and Fig. 3.4b. This study is not affected by clutter due to rain because changes in reflectivity are only obtained from developing (non-precipitating) clouds (see chapter 4.3.3).

3.1.3 Differences in cloud radar software

In the last section it was shown that radar retrievals of KIT and KATRIN with dBZ_{min} = -35 agree fairly well. Using this threshold and analyzing how often reflectivity values occur in different heights (see Fig. 3.5) reveals interesting details for the two cloud radars. The reflectivity-height histograms of KIT and KATRIN displayed in Fig. 3.5 show similar features – qualitatively and quantitatively: a high number of hydrometeors with small dBZ $\leq$ -15 around 11 km, few retrievals between 4 km and 5 km with dBZ $\leq$ 0, and an increase with height in the number of samples with dBZ $\leq$ -22.5 for shallow clouds. Yet, some differences between KIT and KATRIN can be seen, in particular below 2.5 km. These features are a result of the different processing of the retrieved signals due to different software of the two radar systems. One can quantify the differences between the two software systems by comparing retrievals of KATRIN processed with the old and the new software that were generated during the intercomparison time period.

The new developed software used by KATRIN has three important improvements compared to the old software used by KIT. Firstly, much of the ground clutter and clutter caused by heavy precipitating systems, as described in section 3.1.2, can be identified by the new software. The effect of this improvement can be seen by comparing the reflectivity-height histograms constructed with the new software (Fig. 3.5b) and with the old software (Fig. 3.5c). The old software misses to identify clutter in the lower heights of about 300 m, marked by numerous small reflectivity values. The contribution to the overall hydrometeor fraction of those non-meteorological signals is significant, as seen in the total number of retrievals (right side of Fig. 3.5c).

The second improvement of the new software is the compensation of attenuated signals in the lower heights, that are due to a smaller sensitivity of the radar up to a height of 600 m. The last improvement comes into play in the case of saturated signals in the co-channel, where the signal-to-noise ratio (and Z) for hydrometeor targets is estimated in the co-channel using the signal-to-noise ratio in the cross-channel. Here, the power in the

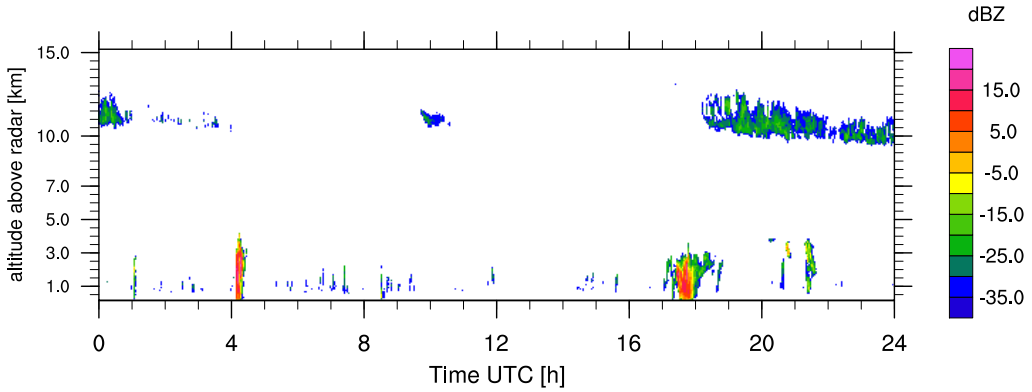

(a) Filtered retrievals of Z by KIT.

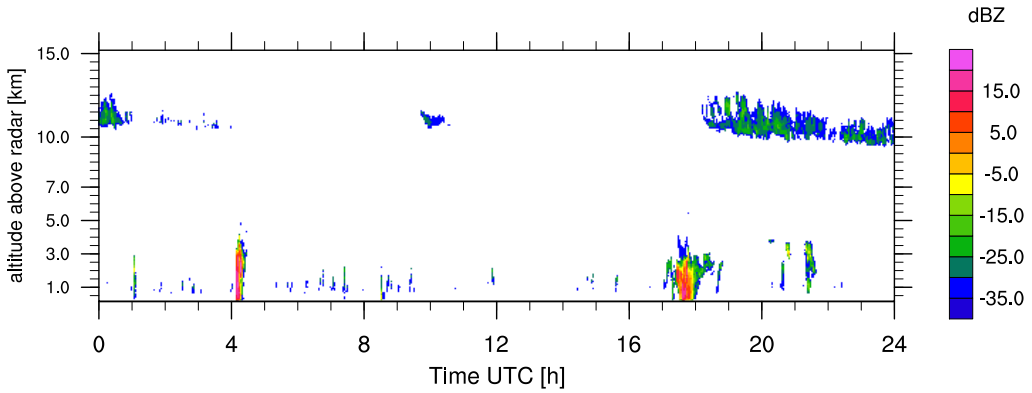

(b) Filtered retrievals of Z by KATRIN.

Figure 3.4: Time-height cross section of reflectivity for both cloud radars operating in the vertically pointing mode on 6 January 2011. Here, a lower limit of $\mathrm{dBZ}_{\mathrm{min}}$ = -35 is applied.

cross-channel is assumed to be smaller by a factor dBZ = 25 than in the co-channel when the targets are spherical. With this assumption non-hydrometeor targets can be identified by their high values in LDR.

The effects of the latter two improvements are shown in the lower heights for high reflectivity values. A high numbers of large reflectivities and a smaller maximum value in Z can be detected by the radar that processes data with the old software (Fig. 3.5a and Fig. 3.5c) compared to data processed with the new software (Fig. 3.5b). The described features occur in a comparable way for KATRIN and KIT data using the old software. This highlights that the described differences for retrievals with dBZ $\geq$ -35 are mostly due to the processing and not to differences in the hardware of the cloud radars. For more details on the new software see Bauer-Pfundstein and Goersdorf (2007).

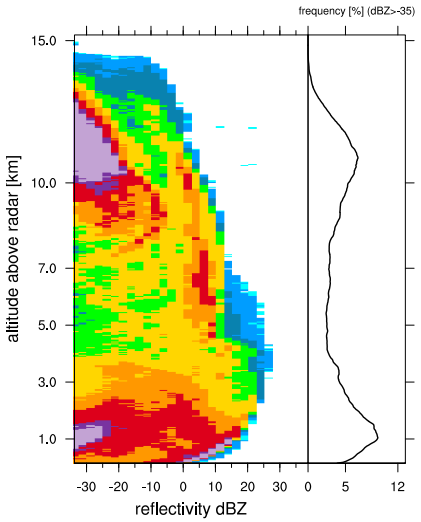

(a) Retrievals of Z by KIT.

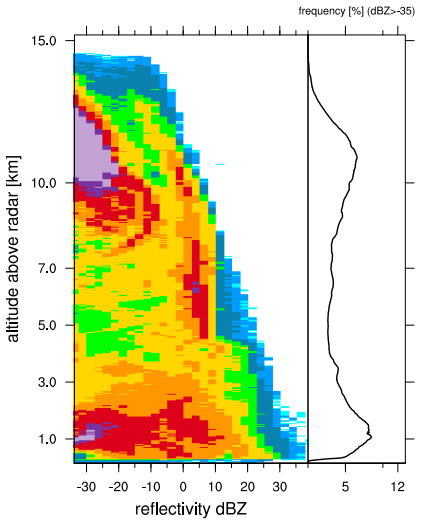

(b) Retrievals of Z by KATRIN.

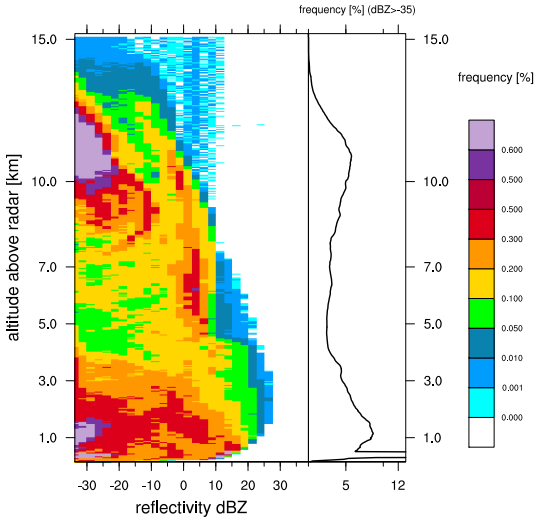

(c) Retrievals of Z by KATRIN using old software.

Figure 3.5: Reflectivity-height histograms from retrievals of Z using the vertically pointing mode for the measurements period from 22 December 2010 to 9 January 2011. On the right side the frequency of occurrence of the total number of retrievals per height levels is displayed a function of height.

3.2 Comparison of different elevation angles

The variety in cloudiness within the trades can be studied with investigating the differences in the radar retrievals of the various elevation angles. In the vertical pointing mode (elevation angle = 90°) the cloud radar observes clouds at the east coast of Barbados, whereas in a tilted mode (elevation angle < 90°) the cloud radar observes clouds a few kilometers upstream off the coast. A difference in the radar retrievals of the various elevation angles would mean that clouds observed at the BCO cannot describe the variety in cloudiness in the trades. A possible reason for those differences could be an "island effect".

The island of Barbados has a smaller heat capacity compared to the heat capacity of the Atlantic Ocean. That means, the absorbed solar energy is reemitted as thermal energy and converted to surface fluxes much faster over the island than over the ocean. The energy sources of convective clouds, such as trade wind cumuli, are mainly surface fluxes. If these fluxes change trade wind cumuli are modulated, e.g. in their extent, depth and optical thickness. Over land the surface fluxes change much faster with time of day, because the incoming solar energy undergoes a daily cycle. Over the ocean the surface fluxes are rather constant over a day and modulate clouds in more constant manner than over land. Therefore, radar retrievals of clouds affected by the island ("island effect") would differ from radar retrievals of clouds over the ocean.

To investigate the existence of an "island effect" the frequency of occurrence of reflectivity from different elevation angles is compared using radar retrievals measured by KATRIN from February 2011 to April 2011. Fig. 3.6 shows various reflectivity-height histograms for elevation angles of 90°, 45°, 22°, 12° and 5° (see panels from top to bottom). Because the range of the radar is always constant for all elevation angles, the maximum height above the ground decreases for small angles. For example, a maximum height of about 1.2 km can be reached when the radar measures with an elevation angle of 5°, as seen in the lowest panel.

The histograms of all elevation angles look very similar, marked by many clouds with dBZ $\leq$ 5 up to a height of 2 km. The clutter however (discussed in section 3.1.2), characterized by low reflectivity values of dBZ < -35, is prominent in low height levels for all elevation angles. Here, the tilt of the antenna determines at which height level the clutter is retrieved. For small elevation angles, the side lobes are reflected earlier from the ground, causing clutter at lower heights, compared to side lobes from large elevation angles, causing clutter in higher heights. The interest of this study is on meteorological signals and those are not different between the various elevation angles.

Another consequence of an island effect is a difference in the daily variation in the frequency of radar retrievals for the various elevation angles. As the island experiences a stronger diurnal cycle than the ocean, the variation in frequency of radar retrievals within a day would be stronger when clouds at the BCO experience an "island effect", compared to retrievals over the ocean. Fig. 3.7 displays time-height histograms for KATRIN retrievals for the different elevation angles, ranging from the vertically pointing mode to an elevation angle of 12°. Many retrievals are found between 0.4 km and 2.5 km and two Maxi in the

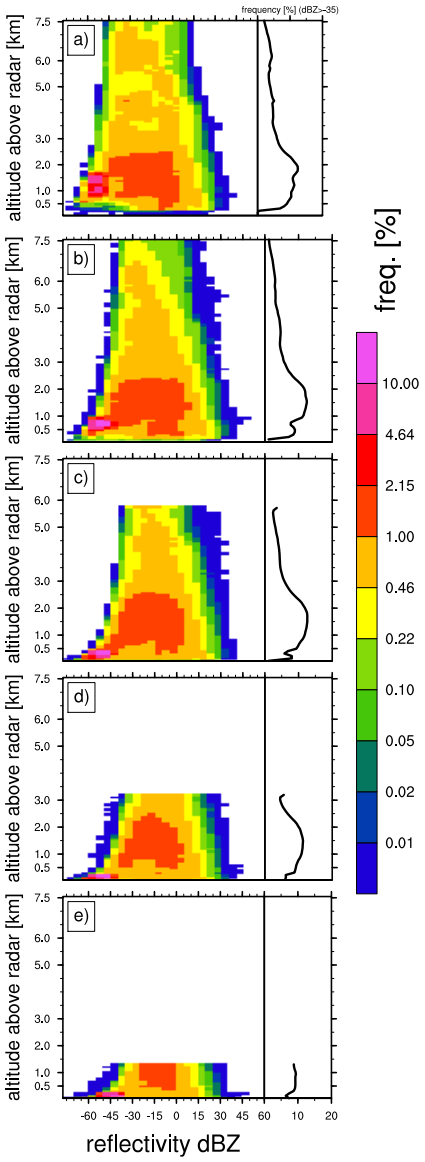

Figure 3.6: Reflectivity-height histogram of different elevation angles from KATRIN for the measurements period from February 2011 to April 2011: a) elevation angle = 90° (vertical pointing mode), b) elevation angle = 45°, c) elevation angle = 22°, d) elevation angle =12°, and e) elevation angle = 5°. Normalization is done over all possible retrievals per height level with a binning of 30 m and reflectivity bins of dBZ = 5. On the right side, the total number of retrievals per height level normalized by all possible retrievals per height level is shown.

number of samples are visible: one in the early morning between 0 UTC and 4 UTC and one in the afternoon between 12 UTC and 16 UTC for all elevation angles. Compared to the vertically pointing mode the occurrence of retrievals of the various elevation angles does not differ significantly.

Small differences between the elevation angles exits but there is no evidence of a strong discrepancy between retrievals from the vertically pointing mode and from the other elevation angles. From the similarities in time-height histograms we deduce there is no strong effect by the island on the clouds observed at the BCO, which is consistent with being able to observe the variety of cloudiness in the trades with measurements at the BCO.

3.3 Conclusion about radar data treatment

The comparison of the retrievals by the two radar systems, KIT and KATRIN, reveals in general a good agreement, in particular in measuring the reflectivity and Doppler velocity (section 3.1.1). Some differences due to different hardware and software processing tools have been discussed in section 3.1.2 and section 3.1.3, respectively. Here, a minimum detectable threshold in reflectivity of -35 has been identified, above which almost all non-meteorological signals are excluded. The utilization of different post-processing tools by the two radars caused different sensitivities of high and low reflectivities, in particular in lower height levels.

Additionally, the settings of the range resolution Δr were changed a couple of times during the measurement period, especially in the beginning. Because the number of range gates is fixed, the maximum range changed from 7.7 km for $\Delta r = 15$ m to 15.2 km for $\Delta r = 30$ m, and reduced the total number of retrievals above 7.7 km (not shown) over the measurement period. This study focuses on shallow cumulus clouds and hence, the reduced number of retrievals in higher heights does not affect this analysis. In summary, following changes in the radar settings have been made during the continually measuring period since April 2010:

- Minimum range gate differs between 150 m and 300 m.
- Range resolution and therefore maximum range (height) is different: $\text{range}_{\text{max}} = 7675$ m for end April - September 2010, else $\text{range}_{\text{max}} = 15200$ m.
- A new feed for the KATRIN antenna was deployed in December 2011, that diminished the clutter characteristics of the side lobes. In November 2012 the old antenna was replaced by a new one.

The question arises, if the datasets of the two cloud radars could be combined to create a homogeneous time series of radar retrievals. The benefit would be in having a long data record which can be used for statistical investigations, being even more robust as a shorter time record. In this chapter it was shown that identifying a minimum detectable threshold in dBZ of -35 results into sensible signals from both cloud radars. Differences due to the different software systems are shown to be manageable to a certain extent.

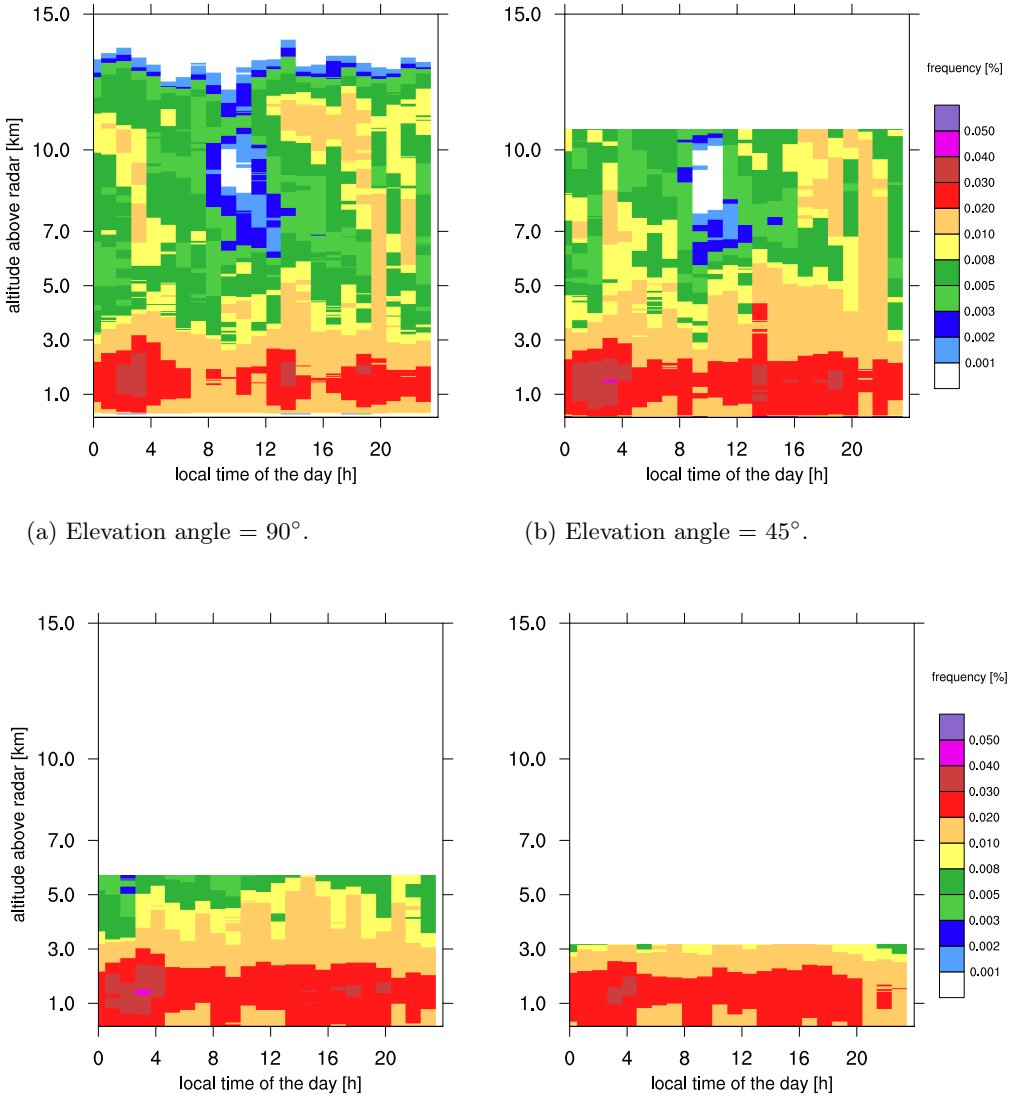

(a) Elevation angle = 90°.

(b) Elevation angle = 45°.

(c) Elevation angle = 22°.

(d) Elevation angle = 12°.

Figure 3.7: Time-height histogram from retrievals using different elevation angles for the measurements period from 1 January 2011 to 4 May 2011 from KATRIN. Here, only retrievals with dBZ $\geq$ -35 are considered of days when KATRIN operated the whole time. For the normalization the number of retrievals at a certain time and height is divided by all retrievals at a certain time. Height levels of 30 m and time bins of one hour are used.

Because this work focuses on the change of reflectivity with height of shallow cumulus clouds (see chapter 4) we are in particular interested in the low reflectivity values below a height of 3 km. These values are highly sensitive to the last two improvement steps in the

new software, as shown in section 3.1. To avoid interpretation of differences in signals due to these issues only KATRIN data is analyzed, which has been processed with the new software. A time duration of 15 months of continual data recording enables us to study statistical robust signals.

An investigation in the differences in reflectivity retrievals of the various elevation angles (section 3.2) reveals that cloud radar measurements at the BCO can be used to characterize the variety of cloudiness in the trades. The radar reflectivity-height histograms only differ by the amount of non-meteorological signals. The daily variation in reflectivity is similar among the different elevation angles with a maximum of retrieved samples in the morning and in the afternoon. That means, clouds observed at the east coast of Barbados do not differ from clouds few kilometers upstream, which allows to analyze clouds with a maritime origin using retrievals in the vertical pointing mode, as done in the further analysis. The investigation of retrievals from the vertical pointing mode is in particular useful, as one can use the Doppler velocity as an indicator of falling velocity. This is elementary for the identification of developing clouds (see chapter 4.3.3). We conclude, the variety of cloudiness in the trades can be observed by cloud radar measurements at the BCO, which deliver unique insights into the micro- and macrophysical properties of trade wind cumuli and their susceptibility to precipitation.

Chapter 4

Signature of aerosols and meteorology in microphysical properties of trade wind cumuli using KATRIN[4]

4.1 Introduction

Whether variations in cloud condensation nuclei, CCN, (and hence the aerosol more generally) meaningfully affect precipitation development in warm clouds remains an open and controversial question. Observations from satellites (Kaufman et al., 2005) suggest that cloud amount co-varies with aerosol amount, consistent with the idea that increasing aerosol amounts hinder warm rain formation and hence increase cloudiness [e.g. Albrecht (1989), Liou and Ou (1989)]. However, because other factors (for instance changes in relative humidity) could explain this type of co-variability, the inference of a meaningful effect of aerosol concentrations on warm rain formation remains controversial (Stevens and Brenguier, 2009). In this study, simultaneous measurements from advanced ground based lidar and radar remote sensing are employed to explore to what extent the variability in the ambient aerosol can explain variability in the propensity of shallow trade wind clouds to form rain.

Clouds in the trades are frequently cumuliform with tops below the freezing level and produce warm rain by coalescence of liquid drops. Observations demonstrate that precipitation may develop very rapidly in these shallow trade wind cumuli (Byers and Hall, 1955). As discussed by Rauber et al. (2007), this relatively rapid initiation of warm rain is still not well understood. The understanding of the warm rain process and what controls it is crucial, because warm rain constitutes a significant fraction of precipitation in the tropics (e.g. Short and Nakamura (2000)) and because cloud amount may ultimately depend on the precipitation efficiency of clouds, as hypothesized by (Albrecht, 1989).

[4]All sections in this chapter in a slightly modified version are part of a publication, in review for *Journal of the Atmospheric Sciences*, 2013, with B. Stevens, L. Nuijens and L. Hirsch as Coauthors.

The idea that changes in the aerosol might modify the microphysical structure of clouds goes back to the early 1970s, when Twomey (1974) suggested that variations in the concentration of CCN may influence cloud, and hence, planetary albedo. Although the physics behind what has come to be known as Twomey's effect is well established, the extent to which these microphysical changes help explain variability in the propensity of clouds to precipitate and the degree to which changes in precipitation efficiency affect cloud amount is much less clear (Stevens and Feingold, 2009). It seems beyond dispute that very large changes in the number of CCN will influence cloud properties to some degree, but to what degree is the crucial question. But it is impossible to assess to which degree without understanding the susceptibility of clouds to their meteorological environment. This meteorological susceptibility is also important in its own right as changes in the cloud environment (e.g. changes in humidity, stability, or surface wind speeds) are expected to accompany global warming, many of which can greatly influence cloudiness (Nuijens et al., 2009), but few of which are intensively studied as are aerosol cloud interactions (Stevens and Boucher, 2012).

To better quantify the relative role of the aerosol as compared to meteorological changes in regulating precipitation from shallow convection, a suite of surface based remote sensing instrumentation has been installed and operated on an upwind observatory on the Island of Barbados. Barbados appeared well suited to a study of an aerosol signal on clouds because it is far from large land masses, so that aerosol from pollution sources over Europe or dust sources over North Africa may imprint themselves on the air masses far upstream of the observational site. Because the timescale for the aerosol to evolve is measured in days [e.g., Warneck (1988)] but thermodynamic conditions in the boundary layer adjust on timescales of hours (Schubert et al., 1979), measurements on Barbados stand a reasonable chance of sampling air masses whose meteorological and chemical properties are decorrelated.

In summary, this study employs a targeted deployment of advanced remote sensing measurements to explore to what extent changes in the precipitation tendencies of trade wind cumuli during aerosol rich days can be attributed to changes in the aerosol, or whether subtle variations in the thermodynamic conditions may also play an important role. The chapter is organized as follows. In section 4.2 the main question of the chapter is framed in terms of a consideration of how strongly the radar reflectivity increases with height (Z-lapse rate), depending on the cloud microphysical properties (e.g., droplet number concentration, N) and cloud bulk properties, such as how cloud water varies with height. Section 4.3 gives a short overview about the data treatment. How the precipitation behavior of shallow clouds changes with Z-lapse rate is described in section 4.4. Then in section 4.5 the change in Z-lapse rate is discussed for aerosol rich and aerosol poor days; relative humidity effects in section 4.6. Conclusions are presented in section 4.7.

4.2 Background and theoretical framing

The radar reflectivity factor Z, or simply 'reflectivity', is the sixth moment of the droplet number distribution $n(D)$ with D being the droplet diameter, and $n(D)\,\mathrm{d}D$ measuring the

number of droplets whose diameters are between $D - \mathrm{d}D/2$ and $D + \mathrm{d}D/2$:

$$Z = \int_0^\infty n(D) D^6 \mathrm{d}D. \tag{4.1}$$

A Γ-distributed droplet number distribution is assumed in this analysis:

$$n(D) = \frac{B^p}{\Gamma(p)} \left(\frac{D}{2}\right)^{p-1} \exp\left(\text{-}B\left(\frac{D}{2}\right)\right), \tag{4.2}$$

with scale parameter, B, and the shape parameter, p.

Furthermore, the liquid water content, q_l, is proportional to the third moment of the droplet number distribution. When using a relationship between Z and q_l and inserting Eq. (4.2) into Eq.(4.1), scale parameter, B, vanishes and Z can be expressed as:

$$Z = k^2 \frac{q_l^2}{N} \left(\frac{6}{\rho_w \pi}\right)^2, \tag{4.3}$$

where N is the zeroth moment. For simplicity, it is assumed that N is constant with height. It is not clear why this should be the case, but measurements from airborne platform [Gerber et al. (2008) and Siebert et al. (2013)] have shown this to be a relatively good assumption.

The parameter k^2 appearing in Eq. (4.6) depends on the shape parameter p of the droplet number distribution:

$$k^2 = \frac{(p+3)(p+4)(p+5)}{p(p+1)(p+2)}. \tag{4.4}$$

In the literature values for $p = 7$ (Deirmendjian, 1969) and $p = 8.7 \pm 6.8$ (Brandau et al., 2010) can be found resulting in $k^2 = 2.62$ and $k^2 = 2.25$, respectively. If the distribution in $n(D)$ is assumed to be monodisperse, then k^2 equals unity. Although k may vary from cloud to cloud, here it is assumed that any covariation is either small, or proportional to variations in N so that the microphysical influence on Z is parameterized by variations in N.

It is further assumed that variations in height can be represented through a subadiabatic factor, β, such that,

$$q_l(z) = \Gamma_{\mathrm{l,ad}} \beta (z - z_\mathrm{b}), \tag{4.5}$$

with the adiabatic liquid water lapse rate $\Gamma_{\mathrm{l,ad}}$ which is a function of temperature, assumed to be constant. Here, $\Gamma_{\mathrm{l,ad}} = 2.00\,\mathrm{g\,kg^{-1}\,km^{-1}}$ is used [cf. Albrecht et al. (1990)] which equals $2.58\,\mathrm{g\,m^{-3}\,km^{-1}}$ when assuming the density of air with $1.29\,\mathrm{kg\ m^{-3}}$.

The subadiabatic factor, β, is defined as the ratio of the actual cloud liquid water to its adiabatic value. It ranges from 0 to 1 for $z_\mathrm{b} \leq z \leq z_\mathrm{t}$, with cloud base, z_b, and cloud top, z_t. For cloudy air rising reversibly (i.e. without mixing and with radiative effects being negligible), the liquid water will increase adiabatically, and $\beta = 1$. Shallow cumuli

are known to be very subadiabatic [Zhang et al. (2011), and Blyth and Latham (1993)], because they continuously mix with their environment. Based on measurements [Kim et al. (2008) and Boers et al. (2006)] and Large Eddy Simulations (Zhang et al., 2011), a range in β can be found with $0.1 < \beta < 0.9$. Especially near cloud tops of cumulus clouds, β is often much less than one.

In light of these assumptions:

$$\begin{aligned} Z(z) &= \gamma \frac{\beta(z)^2}{N}(z - z_\mathrm{b})^2 \\ \text{with } \gamma &= \left(\frac{6k\Gamma_{\mathrm{l,ad}}}{\rho_w \pi}\right)^2. \end{aligned} \tag{4.6}$$

For Z in $\mathrm{mm^6 m^{-3}}$ the commonly used dBZ is defined as:

$$\mathrm{dBZ(z)} = 10 \cdot \log_{10}\left(\frac{Z(z)}{1\,\mathrm{mm^6 m^{-3}}}\right). \tag{4.7}$$

Hereafter, Z and dBZ are used interchangeably to describe reflectivity.

The factor $\beta^2 N^{-1}$ in Eq. 4.6 determines how rapidly the reflectivity increases with height, the Z-lapse rate. Its effect can be measured in a bulk sense by measuring the reflectivity, Z^* at some specified height above cloud base, here at 1 km above z_b. The reflectivity Z^* is sensitive to q_l^2 (or β^2), but proportional to only the first power of N. Hence, β has a stronger impact on $\beta^2 N^{-1}$, if assuming N and β to be invariant with height. Even if we were to allow for N to vary, the height variations in β would likely dominate for this very reason, in part justifying our earlier assumptions.

However, if the cloud water can be controlled for, by sampling clouds in sufficiently homogeneous thermodynamic conditions variations in N may dominate variations in $\beta^2 N^{-1}$. Because the trades are a steady region in terms of their meteorological environment it may be possible to isolate the role N and the underlying CCN concentration, by assuming that β does not vary, or relative humidity in the cloud layer. Indeed, during a field campaign in Barbados (Siebert et al., 2013) measured large variations in N (almost by a factor of ten) but proportionally much smaller differences in the thermodynamic environment, e.g. temperature and cloud base height.

Nonetheless, the assumption that β is constant is a strong one, particularly given the choice to measure the microphysical trajectory of clouds in terms of their radar reflectivity, which compared to a lower moment, emphasizes the role of β. For this reason additional measurements are employed in an attempt to better control for β for instance through the use of coincident and high-frequency relative humidity profiles derived from a Raman lidar.

Fig. 4.1 illustrates how the reflectivity would change with height as a function of a single parameter, $\beta^2 N^{-1}$, which is assumed to be constant (black lines), or linear in height (gray line), for instance as might happen if the subadiabatic factor decreases with height in the cloud. If N stays constant with height, a decrease in $\beta^2 N^{-1}$ can be interpreted as decrease in β.

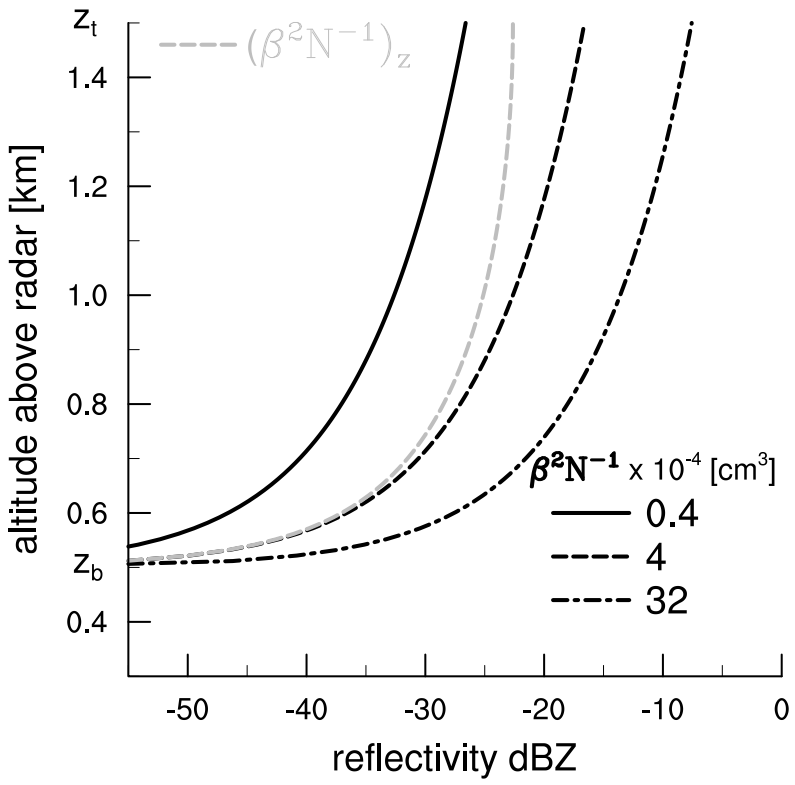

Figure 4.1: Reflectivity dBZ as a function of height (z) for a droplet distribution $n(D)$ behaving as a Γ-distribution [Eq. (4.2)]. k^2 is chosen to be 2.25. The black line patterns display conditions of different $\beta^2 N^{-1}$, which are set to be constant with height. The gray dashed line represents a decreasing $\beta^2 N^{-1}$ from 4.0 at cloud base $z_\mathrm{b} = 0.5\,\mathrm{km}$ to $\beta^2 N^{-1} = 1.0$ at cloud top $z_\mathrm{t} = 1.5\,\mathrm{km}$.

4.3 Methodology

In this section the treatment of the cloud radar data and the algorithm of identifying cloud objects are described. Lastly, three methods which have been employed to identify different aerosol environments are explained.

KATRIN cloud radar

Measurements by the KATRIN cloud radar are used to investigate how and why microphysical properties of trade wind cumuli change, in particular as regards the development of precipitation. A full description of the KATRIN cloud radar is given in chapter 2.2. In

chapter 3 we showed there is no evidence of an island effect. Based on this, measurements have predominantly been collected in the vertical pointing mode. Hence, the remainder of this chapter is restricted to an investigation of measurements taken in this mode of operation. Furthermore, a conservative filter of $\geq$ - 35 seemed sufficient, thereby avoiding any question of possible contamination from spurious signals, as discussed in chapter 3.

4.3.1 Identifying cloud entities

One aim of this study is to look at the development of trade wind cumuli in different aerosol and meteorological environments. For this purpose, a segmentation algorithm has been developed to identify echo objects (hereafter named " cloud entities") representative of typical trade wind cumuli. Before applying the algorithm the radar data is regridded on to a time-equidistant grid. Following the initial screening of the data, radar echoes are defined as pixels with dBZ $\geq$ -35. Then the segmentation algorithm identifies conterminous radar echoes as cloud entities, having common edges and vertices (Fig. 4.2). Only cloud entities consisting of more than two pixels, or with bases below 1 km (named "shallow cloud entities" and highlighted in black in bottom panel of Fig. 4.2) are considered so as to exclude cloud fragments and stratiform clouds. Because only retrievals with reflectivities larger than dBZ = -35 are retained, the first radar echoes near cloud base and very small, cumulus humulis are not well sampled, and the actual base of the cloud will in most instances be somewhat below the level of the first radar echo. The base and top of echo objects is hereafter named cloud base and cloud top, respectively. Furthermore, to treat the properties of trade wind cumuli independent of their cloud size and vertical extent the mean properties at given height levels of each entity are calculated and compared.

Cloud entities with a mean Doppler velocity $\tilde{v}_z|_{cld} \geq 0.5$ m s^{-1} in all height levels are defined as developing cumulus clouds. By concentrating on shallow clouds with a mean upward motion a higher susceptibility towards changes in environmental air properties is expected, as shown in numerical simulations by Zhao and Austin (2005). Besides the variability of updraft velocity, the aerosol number concentration are found to dominate the variability of cloud droplet number concentration N in active shallow cumulus clouds (Reutter et al., 2009). But most importantly, Z is measured before the development of precipitation by concentrating on developing clouds.

4.3.2 Different aerosol environments

Three different methods for identifying the aerosol environment are explored: [i] a back-trajectory analysis that identifies the air mass origin as continental or maritime; [ii] the particle backscatter in the subcloud layer as measured by the Raman lidar; [iii] the integrated linear-depolarization ratio δ up to 4 km height as measured by the Raman lidar, which identifies dust. In general, dust is not thought to be a good CCN, but by the time the dust aerosol reaches Barbados it has aged considerably, and organic coatings can increase its solubility (Savoie and Prospero, 1980). So associating dusty days with higher CCN concentration is not unreasonable.

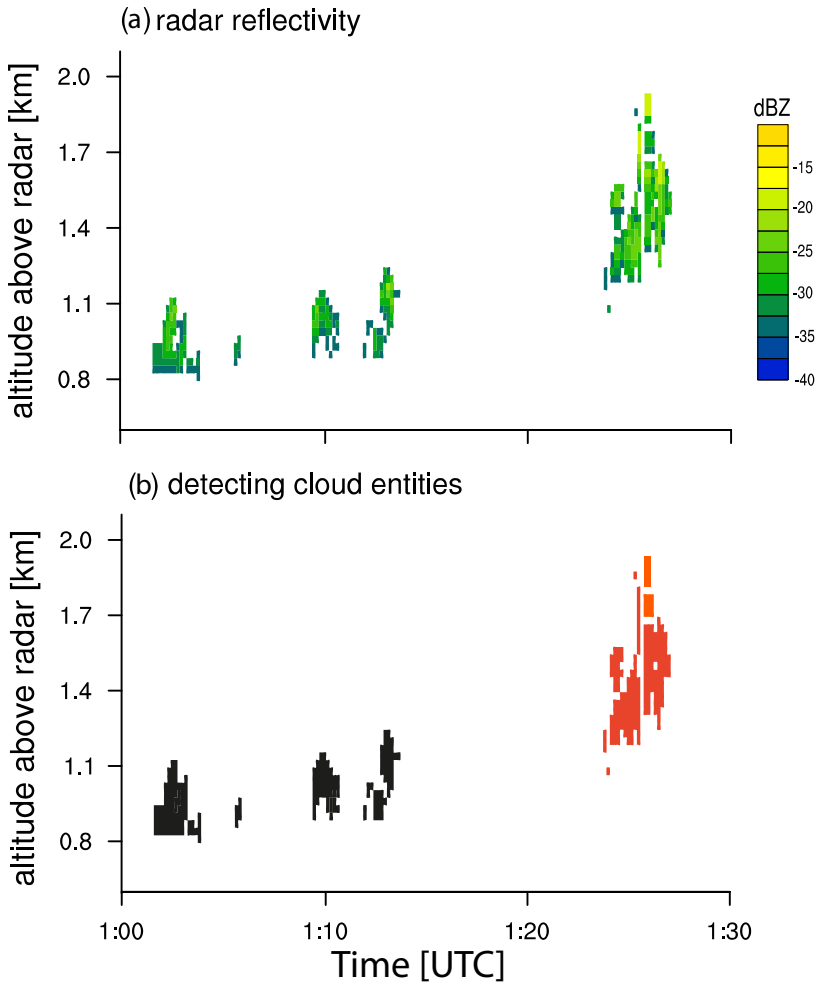

Figure 4.2: Reflectivity (contoured, upper panel) versus height and time, for a thirty minute period on 2nd February 2012. Lower panel identifies shallow cloud entities in black and other clouds in red.

The first method defines air masses as continental or maritime, as described in chapter 2.5. The cloud radar data is then segregated according to the air mass origin at an altitude of 3 km, where Saharan dust typically resides (Prospero and Carlson, 1972). The motivation to segregate cloud radar data is based on findings by Dr. Heike Wex using in-situ aerosol data, as explained in the appendix.

For the second method the mean aerosol backscatter distribution in the subcloud layer (between 140 and 260 m) is calculated and low backscatter samples are defined within the 5^{th} to 30^{th} percentile and high backscatter samples within the 70^{th} to 95^{th} percentile range. The first and last 5% in the probability distribution of aerosol backscatter are excluded to omit outliers or extreme values.

The third method uses the property of dust particles being non-spherical and therefore having higher values of δ. For each Raman lidar profile up to 4 km the height averaged linear-depolarization ratio δ is used to differentiate into a non-dusty and dusty profile. The chosen threshold of $\delta = 0.04$ roughly separates two different probability distribution of δ that appear when sampled over 2 years between April 2010 and March 2012.

A radar profile is classified as non-dusty when the coincident lidar signal has $\delta < 0.04$ and as dusty when $\delta \geq 0.04$. Here, the closest Raman profile in time up to 60 seconds before and after the radar echo is considered. A certain number of radar profiles make up a developing shallow cloud entity. A developing shallow cloud entity occurs during non-dusty conditions if more non-dusty than dusty radar profiles exist over the duration time of a cloud (similarly for dusty conditions). A day is labeled "non-dusty" when more developing shallow cloud entities have been measured during this day being non-dusty than dusty (similarly for a "dusty day").

4.3.3 Data treatment

The theoretical Z-profile from section 4.2 is investigated if it resembles the measured Z-profile. Fig. 4.3a displays the histogram of Z for all data (523 616 profiles). The most frequent reflectivity bin per height level increases with height up to 3 km, but the spread is large and the signal is weak. A clear increase of Z with height is not evident. By focusing on radar retrievals within shallow cloud entities with $v \geq 0.5$ m s^{-1}, rain is most likely excluded. Here, reflectivity increases as postulated in section 4.2, with a rather small spread (Fig. 4.3b) with a sample size of 42 260 profiles. The few detections with small reflectivities below 700 m can be explained by a few rain drops caught in an updraft or by ground clutter that was not excluded by the threshold of dBZ $\geq$ -35. In conclusion, the displayed Z-lapse rate behaves accordingly to the theoretical Z-lapse rate (see different dashed lines in Fig. 4.1), confirming that the postulated hypothesis on the Z-lapse rate (section 4.2) reasonably explains the development of radar echoes of trade wind cumuli.

The Z-lapse rate, more precisely $\beta^2 N^{-1}$, is derived by performing a non-linear regression of the median reflectivity $\bar{Z}_z|_{cld}$ of a single developing cloud entity or from an average of $\bar{Z}_z|_{cld}$ of all developing cloud entities, $\tilde{Z}_z$, as done in section 4.5. Hereby, $\bar{Z}_z|_{cld}$ and $\tilde{Z}_z$ are given per height level, $\triangle z = 30$ m. Values of the lower quartile of the distribution in $\beta^2 N^{-1}$ are defined as clouds with low $\beta^2 N^{-1}$ and values in the upper quartile as clouds with high $\beta^2 N^{-1}$. A day is labeled "large Z^*-day" when there are more developing shallow cloud entities measured during this day having a high $\beta^2 N^{-1}$ than low $\beta^2 N^{-1}$ (similarly for "small Z^*-day").

4.4 Differences in the precipitation characteristics

To better understand the precipitation of shallow cumuli and their dependencies we first explore if large Z^*-days are different from small Z^* -days in terms of their precipitation behavior before investigating what factors control the variation in Z^*. The aim is to understand whether or not Z^* (equivalently $\beta^2 N^{-1}$) is a good proxy for the tendency of

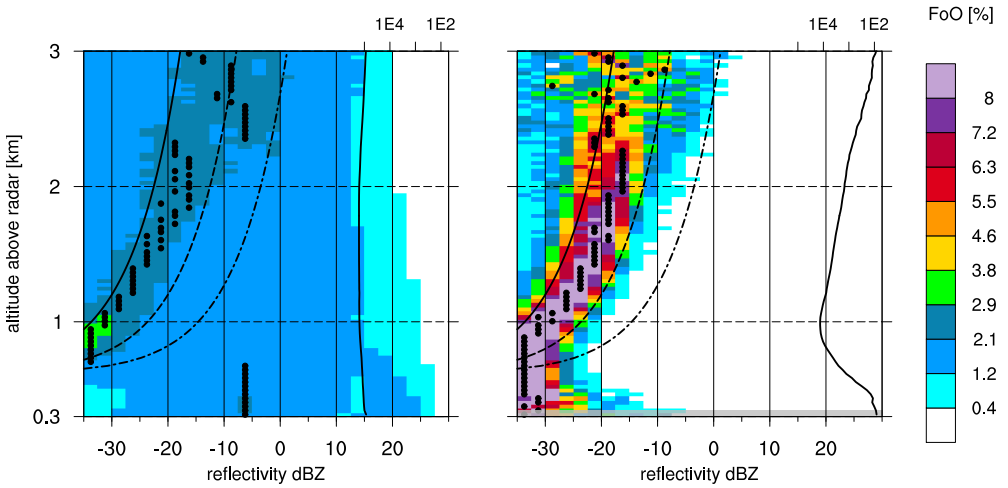

(a) All KATRIN cloud radar data measured with a vertical pointing antenna.

(b) KATRIN data from shallow cloud entities with a Doppler velocity $v \geq 0.5\,\mathrm{m\,s^{-1}}$, when the Raman lidar measured.

Figure 4.3: Reflectivity-height histograms normalized by the sum of all actual retrievals per height level of 30 m thickness. The frequency of occurrence (FoO) is calculated for every dBZ = 1. The semi-transparent gray bar marks height levels which include less than 100 retrievals. Dots denote the most frequent reflectivity bin for each height level and the black line on the left of each panel displays the number of retrievals per height level. The different dashed lines mark the behavior of reflectivity as postulated in section 4.2 for $n(D)$ behaving as a Γ-distribution function as in Fig. 4.1.

macrophysically similar clouds to develop precipitation, and if the subsequent statistics of these clouds is consistent with a more rapid development of precipitation on high Z^*-days.

Assuming that the development of precipitation is associated with the collapse of the cloud top echo, the propensity of clouds to form precipitation can be measured by the frequency with which the cloud top echo collapses during a day for cloud with a given cloud top. This type of analysis is performed by calculating the ratio of the number of clouds that have a downward moving cloud top to the number of all clouds during a day. Fig. 4.4 shows the fraction of days on which a certain portion of cloud tops is moving downward during a day, only considering clouds with tops between 720 and 1140 m. Here, a downward moving cloud top has hydrometeors which have a mean Doppler velocity at cloud top of -0.5 $\mathrm{m\,s^{-1}}$ or less.

In general, clouds can have a negative velocity at cloud top because of two reasons: the development of rain drops large enough to fall through the updraft, and the evaporative collapse of an updraft. As clouds penetrate deeper into dry air updrafts mix with evaporatively unstable air and collapse. We assume that the development of rain drops to fall causes negative Doppler velocity, as it is consistent with higher values in Z^*. Hence, clouds with a greater propensity toward negative velocities can be seen as more sensitive to form

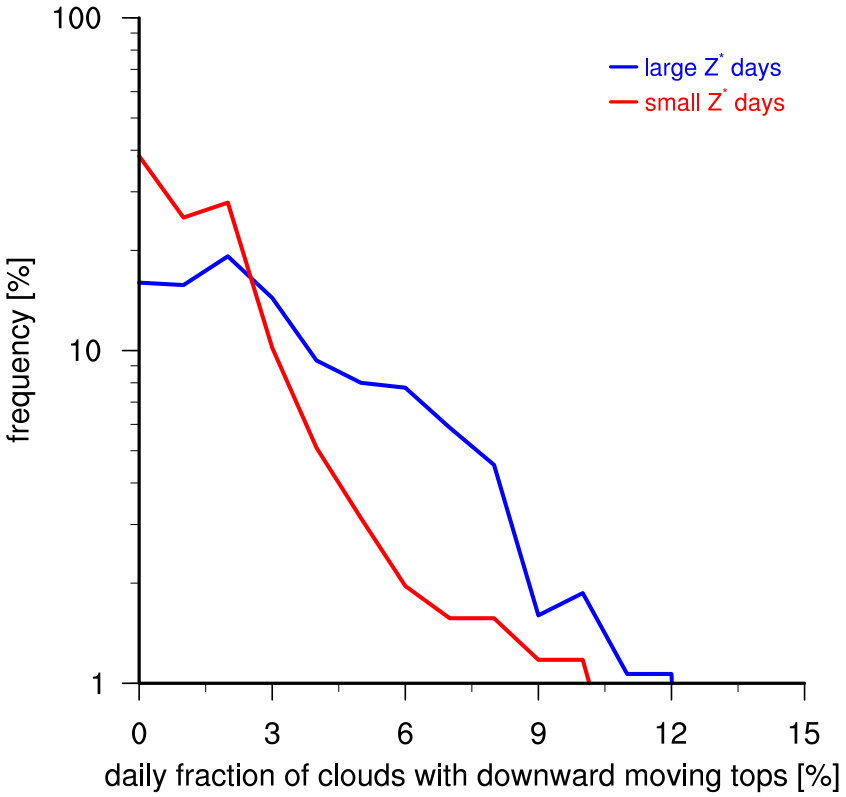

Figure 4.4: Distribution of daily fraction of clouds with downward moving cloud tops of $v_t \leq -0.5\,\mathrm{m\,s^{-1}}$ for every shallow cloud entity having $720\,\mathrm{m} \leq z_t \leq 1140\,\mathrm{m}$. The fractional distribution is calculated for every 5% and smoothed using a running mean of three subsequent points. Different colors refer to different regimes, as indicated in the Figure. Caution: the y-axis is displayed in a logarithmic scale.

rain. Fig. 4.4 shows that, clouds on large Z^*-days have more frequent downward moving cloud tops than on small Z^*-days, consistent with clouds having a higher tendency to rain more on large Z^*-days.

Next to having a higher tendency to rain more, we expect that clouds on large Z^*-days form rain at a lower heights. This means that clouds have $v < 0$ at lower heights, because a significant number of raindrops will be moving downward rather than upward. To test this we show the distribution in daily mean Doppler velocity $\tilde{v}_t$ at cloud top z_t (Fig. 4.5). Because cloud base is confined to $700\,\mathrm{m} \pm 200\,\mathrm{m}$ (Nuijens et al., 2013) trade-wind cumuli having high cloud tops are assumed to be deeper. In general, the most frequently observed $\tilde{v}_t$ decreases with an increase in cloud top height, starting from about $0.75\,\mathrm{m\,s^{-1}}$ at $z_t = 0.8\,\mathrm{km}$ to about $-0.75\,\mathrm{m\,s^{-1}}$ at $z_t = 1.8\,\mathrm{km}$. On large Z^*-days the tendency to sample a downward moving echo (which we interpret as the effect of precipitation) at lower heights ($z_t \sim 1.1\,\mathrm{km}$ and above) is enhanced than on small Z^*-days ($z_t \sim 1.4\,\mathrm{km}$).

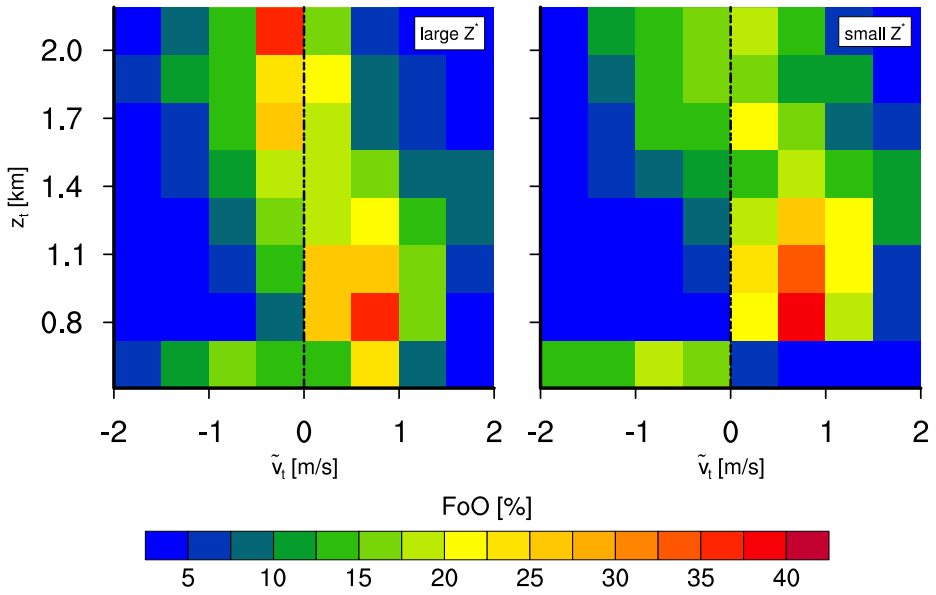

Figure 4.5: Histogram showing the frequency of occurrence (FoO) for shallow clouds having a certain daily mean velocity at cloud top $\tilde{v}_t$, normalized by the sum of all clouds of a particular z_t. The binning in z_t is 210 m and the FoO is calculated for every $\tilde{v}_t = 0.5\,\mathrm{m\,s^{-1}}$. Panels refer to conditional samples during large Z^* and small Z^*.

By excluding all cloud entities with negative velocities (rain), one would expect lower cloud tops for large Z^*-days, because we exclude clouds that rain, which are usually deep clouds having high cloud tops. Fig. 4.6 shows the distribution of cloud tops for developing cumulus clouds. As expected, developing cumulus clouds with a large Z^* have lower cloud tops with a peak at 0.8 km compared to clouds with a small Z^*, which have a peak at 1.2 km. This is also consistent with the hypothesis that trade wind cumuli with a large Z^* have a higher tendency to form rain at lower heights, because clouds have to grow less deep before developing precipitation than clouds with a small Z^*.

In summary, although one could find fault with any one of the measures used to establish a connection between Z^* and the propensity toward rain development, taken together a consistent picture emerges. On large Z^*-days more clouds develop cloud top signatures indicative of rain (Fig. 4.4), the emergence of a precipitation shaft happens lower in the cloud (Fig. 4.5), and non precipitating clouds do not reach as deeply in the atmosphere (Fig. 4.6). Thus Z^* appears to be a useful proxy for the propensity of clouds to form rain.

Based on the above, in the next section we investigate how N influences Z^*. Here, we assume that β is likely to be constant given the homogeneity of the thermodynamic conditions. We use the information about the dust, to investigate how different CCN concentration and hence different cloud droplet number concentration affect Z^*.

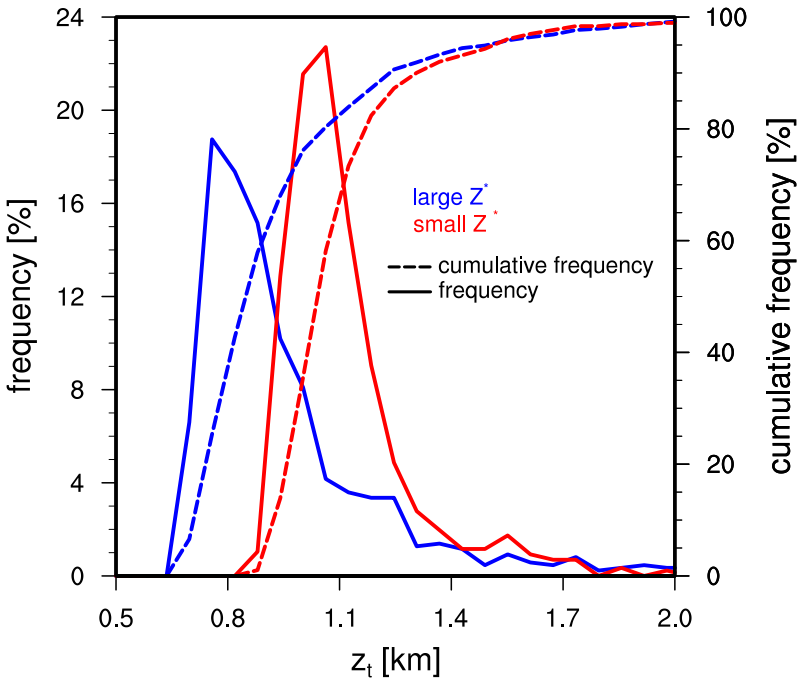

Figure 4.6: Distribution of z_t from developing cumulus clouds. Solid lines show the fractional distribution per $\triangle z_t = 60\,\mathrm{m}$ and the dashed lines to their corresponding cumulative distribution. Blue color refer to clouds during large Z^* days, red to clouds during small Z^* days.

4.5 Z-lapse rate for different aerosol environments

How does Z^* change in an environment with many or few CCN? And what is the variability in Z^*, when the liquid water content is similar? According to the theory (section 4.2) we would expect a large Z^* for clouds with low droplet number concentration N compared to clouds with high N, under the influence of similar meteorological conditions, that can be measured by the subadiabatic factor, β.

Although a back-trajectory analysis was successful in discriminating between aerosol rich and aerosol poor days during a six week period of intensive field measurements (Siebert et al., 2013) and backscatter is commonly used as an indicator of aerosol amount, surprisingly only the third method for discriminating between dusty and non-dusty days was associated with statistically significant differences in the radar retrievals. In detail, $\beta^2 N^{-1}$ for maritime conditions is $0.90 \cdot 10^{-4}\mathrm{cm}^3$, and for continental conditions $0.95 \cdot 10^{-4}\mathrm{cm}^3$. For conditions of low backscatter values of $0.86 \cdot 10^{-4}\mathrm{cm}^3$ and for high backscatter $1.04 \cdot 10^{-4}\mathrm{cm}^3$ are derived. In both cases, the back-trajectory and backscatter analysis, the differences are opposite to what one would expect, but not significant as determined by a Kolmogorov-Smirnov test of the distribution of $\tilde{Z}_z$ between the regimes.

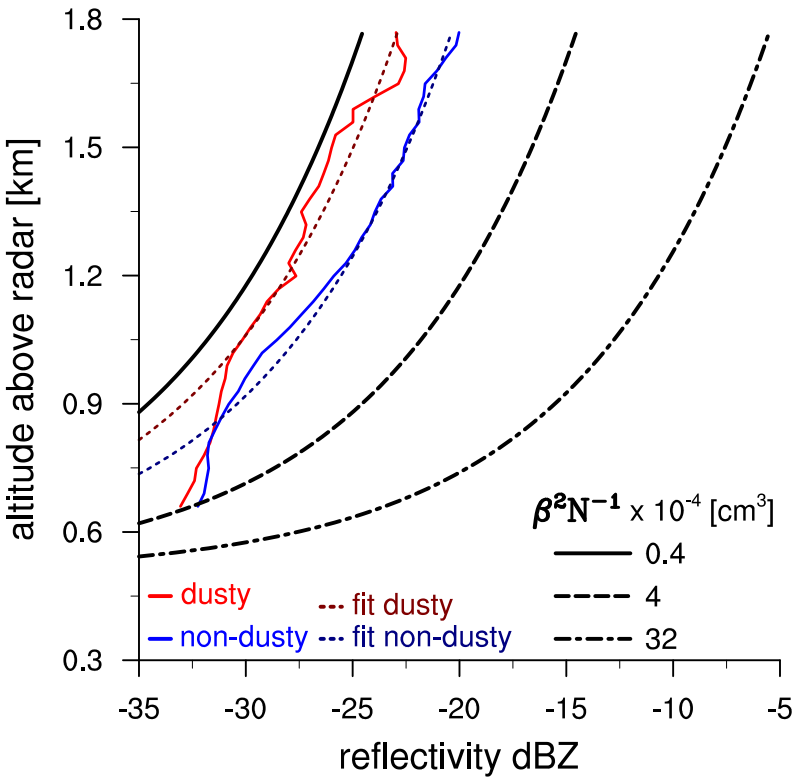

Figure 4.7: Change of averaged reflectivity $\tilde{Z}_z$ with height of developing cumulus clouds during non-dusty (blue line) and dusty (red line) conditions. Only $\tilde{Z}_z$ are displayed which pass the 2-sided Kolmogorov-Smirnov test. The dotted colored lines display the non-linear regression according to Eq. 4.6 for both regimes for $n(D)$ behaving as a Γ-distribution function with $k^2 = 2.25$ and an assumed cloud base height of 500 m. The different black lines display the change of Z with height for conditions of various $\beta^2 N^{-1}$, which are set to be constant with height as described in section 4.2. Further details see Fig. 4.1.

Using the lidar depolarization as a measure of the aerosol amount does however, indicate a difference in the development of the Z-lapse rate on dusty, versus non-dusty days (Fig. 4.7). Here, only median reflectivities $\tilde{Z}_z$ of non-dusty and dusty conditions are considered for which the 2-sided Kolmogorov-Smirnov test proves a significant difference in the distribution of $\tilde{Z}_z$ between the regimes. The dotted colored lines in Fig. 4.7 are non-linear fits for $\tilde{Z}_z$ following Eq. 4.6 with $k^2 = 2.25$ and $z_b = 0.5$ km. A slightly larger Z-lapse rate can be seen during non-dusty conditions with $\beta^2 N^{-1} = 1.04 \cdot 10^{-4}\text{cm}^3$ compared to dusty conditions with $\beta^2 N^{-1} = 0.58 \cdot 10^{-4}\text{cm}^3$. These calculated numbers are in the range of the proposed $\beta^2 N^{-1}$, consistent with a change in the dust load impacting the behavior of radar reflectivities.

Table 4.1: Number of days during non-dusty and dusty conditions for different seasons between 1 January 2011 and 15 March 2012. Winter season includes months December to May and summer season includes months June to November.

season \ regime	all	non-dusty	dusty
whole time	204	161	43
winter	180	147	33
summer	24	14	10

Assuming a fixed cloud base of $z_b = 0.5\,km$ may introduce uncertainties in $\beta^2 N^{-1}$. Cloud bases during winter are higher by about 200 m than during summer (Nuijens et al., 2013). In Table 4.1 the number of days on which we find certain regimes are presented. In general, we sample more days during non-dusty conditions than during dusty conditions, but the non-dusty regime is sampled relatively more often during winter (December to May) than during summer (June to November), consistent with our understanding of dust transport from Africa (Prospero and Lamb, 2003). Therefore, the mean cloud base during non-dusty conditions could be higher than during dusty conditions, which would shift the Z-profile towards the right (higher $\beta^2 N^{-1}$). For example, assuming a cloud base of $z_b = 0.7\,km$ gives $\beta^2 N^{-1} = 1.59 \cdot 10^{-4} cm^3$. Thus, by considering $z_b = 0.5\,km$ even further supports that non-dusty conditions are different than dusty conditions. However, this difference in $\beta^2 N^{-1}$ between non-dusty and dusty conditions is still rather small with $0.46 \cdot 10^{-4} cm^3$.

The postulated behavior of how $\beta^2 N^{-1}$ differs between non-dusty and dusty conditions holds for the derived $\beta^2 N^{-1}$ from the mean reflectivities $\tilde{Z}_z$ of all height levels, calculated from all developing cumulus clouds. To test if this holds true for derived $\beta^2 N^{-1}$ from individual developing cumulus clouds, a nonlinear fit of the median reflectivity $\bar{Z}_z|_{cld}$ is performed for each cloud entity separately. The distribution of the derived $\beta^2 N^{-1}$ is shown in Fig. 4.8 for all and for dusty conditions. The majority of all cloud entities are sampled during non-dusty conditions, hence the distribution of $\beta^2 N^{-1}$ during all conditions resembles the distribution during non-dusty conditions. The average of $\beta^2 N^{-1}$ over all cloud entities differs from the derived $\beta^2 N^{-1}$ of Fig. 4.7 during non-dusty and dusty days. That is because the measured reflectivities of fewer deeper clouds contribute stronger to the derived $\beta^2 N^{-1}$ in the first case. Therefore, it is crucial to investigate how the distribution of $\beta^2 N^{-1}$ from individual developing cloud entities behaves during non-dusty and dusty conditions.

Under dusty conditions more frequent low values of $\beta^2 N^{-1}$ are seen. Furthermore, many of the entities during non-dusty and dusty conditions do not behave differently in terms of $\beta^2 N^{-1}$. What is interesting, though, is the large spread in $\beta^2 N^{-1}$ for all samples. It appears that changes in CCNs, and hence N, cannot explain solely the variability in $\beta^2 N^{-1}$ (or Z^*).

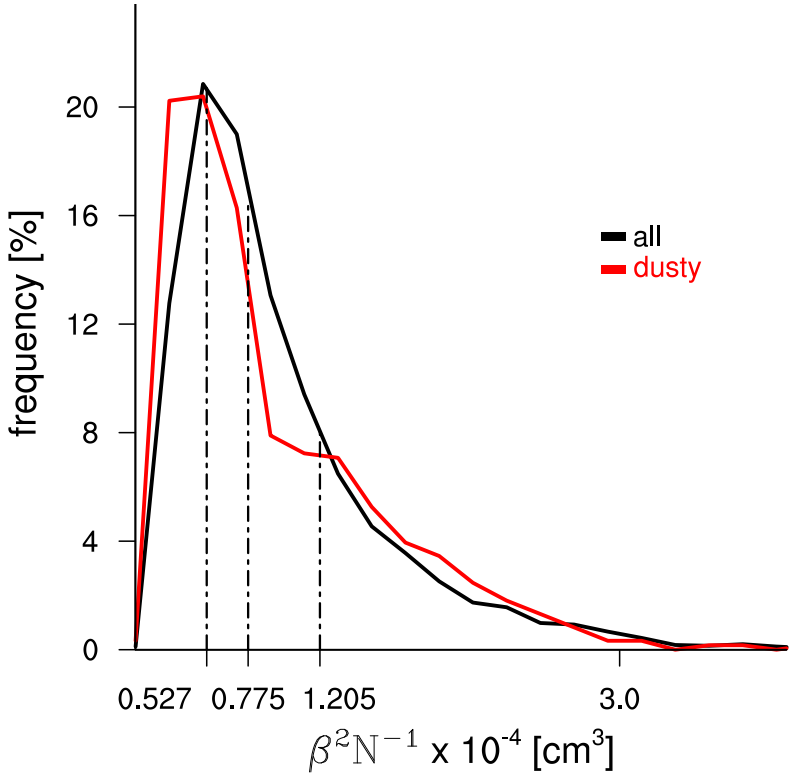

Figure 4.8: Distribution of $\beta^2 N^{-1}$ of every developing cumulus cloud. Black lines show the frequency per $0.2 \cdot 10^{-4}\text{cm}^3$ of all conditions and red lines of dusty conditions. At the top the 25^{th} percentile $x_{25} = 0.53 \cdot 10^{-4}\text{cm}^3$, the median $x_{50} = 0.78 \cdot 10^{-4}\text{cm}^3$ and the 75^{th} percentile $x_{75} = 1.21 \cdot 10^{-4}\text{cm}^3$ of the distribution in $\beta^2 N^{-1}$ during all conditions is marked.

In summary, the information about the dust concentration shows on average only small differences in Z^* and a wide spread in Z^* for individual clouds. For this reason we revisit the question of how β influences Z^*, which we interpret as the sensitivity of Z^* to the meteorological environment of the clouds. In the next section we test how meteorological factors, like relative humidity, influence Z^* by changing β along with N.

4.6 Z-lapse rate and its dependency on meteorological conditions

The liquid water content, q_l, inside clouds depends on the mixing of cloudy with non-cloudy air. This mixing and the effect of mixing depend on variations in temperature, relative humidity, η, or other meteorological conditions which would change q_l and hence β. The relative humidity indeed varies among the different samples (see Fig. 4.9). A low relative humidity might be expected to lead to more dilution of the cloud, and hence a smaller β. The fact that the relative humidity in the cloud environment might play an important

role in determining whether or not a cloud precipitates is not new idea, as a number of studies have shown that the development of precipitation in both deep and shallow convection is very sensitive to the relative humidity in the lower and lower-mid troposphere [e.g. Holloway and Neelin (2009) and Nuijens et al. (2009)]. However the differences in the relative humidities are rather small, which raises the question how to quantitatively compare the influence of η to that of N in determining Z^*.

In Fig. 4.9 the average and inner-quartile range of daily median relative humidity is shown as a function of height. The use of daily data facilitates the use of the Raman lidar humidity profiles which are only available at night, and is consistent with an auto correlation timescale of the radar reflectivity of about 0.25 days. Dusty days show a higher relative humidity because these tend to occur more frequent during summer when winds are southeasterly. That means that during dusty days, an aerosol effect on Z^* through an increase in N could be compensated by an increase in relative humidity (higher β^2). A high N might be masked when looking at $\beta^2 N^{-1}$, which could cause a similar distribution in $\beta^2 N^{-1}$ (Fig. 4.8) between dusty and non-dusty days. Would relative humidity be the same, we would expect a different distribution.

If we next contrast the large Z^*- versus small Z^*-days, the profiles reverse. In other words, β^2 and N go hand in hand in terms of their effect on Z^*. $\bar{\eta}$ is similar up to 0.9 km and then decreases faster for small Z^*. Hence, dry conditions for clouds with small Z^* contribute additionally to low values in Z^* ($\sim$ low values in $\beta^2 N^{-1}$).

The different sensitivities of developing clouds to form rain at lower heights (not shown) between non-dusty and dusty days is lower than for large Z^*- and small Z^*-days (Fig. 4.5). The higher relative humidity on large Z^*-days is consistent with the stronger signal in precipitation. To test the sensitivity of relative humidity on β in determining the strength of reflectivity Z^*, a simple entraining plume model is employed.

In this plume model β is calculated by taking the ratio of liquid water, q_l, and an adiabatic liquid water, $q_{\mathrm{ad},l} = 2\,\mathrm{g\,kg^{-1}}$ at 1 km above cloud base. The liquid water, q_l, is simply:

$$q_l(z) = q(z) - q^*(z), \tag{4.8}$$

with total water inside cloud, q, and saturated specific humidity, q^*. The latter is computed at cloud base (z_b) and at 1 km above cloud base (z_1). The saturation water vapor pressure is assumed to behave according to Bolton's formula:

$$q^*(z) = 0.622 \cdot p(z)^{-1} \cdot 6.112 \cdot \exp\left(\frac{17.67 \cdot \vartheta(z)}{\vartheta(z) + 243.5}\right), \tag{4.9}$$

with pressure p [hPa] and temperature ϑ [°C]. The values in p and ϑ are based on profiles from radiosondes ($p_{z_\mathrm{b}} = 952\,\mathrm{hPa}$ and $\vartheta_{z_\mathrm{b}} = 22.5\,^\circ\mathrm{C}$, $p_{z_1} = 850\,\mathrm{hPa}$ and $\vartheta_{z_1} = 16.05\,^\circ\mathrm{C}$), which were launched on Barbados in November 2010 and April 2011.

To compute q we solve the massflux equation for an entraining plume model of a cloud by Tiedtke (1989), which defines the change in total water inside cloud as:

$$q(z) = \tilde{q}(z) + \varepsilon^{-1}\frac{\delta q}{\delta z}\Big(1 - \exp\big(-\varepsilon(z - z_\mathrm{b})\big)\Big) \tag{4.10}$$

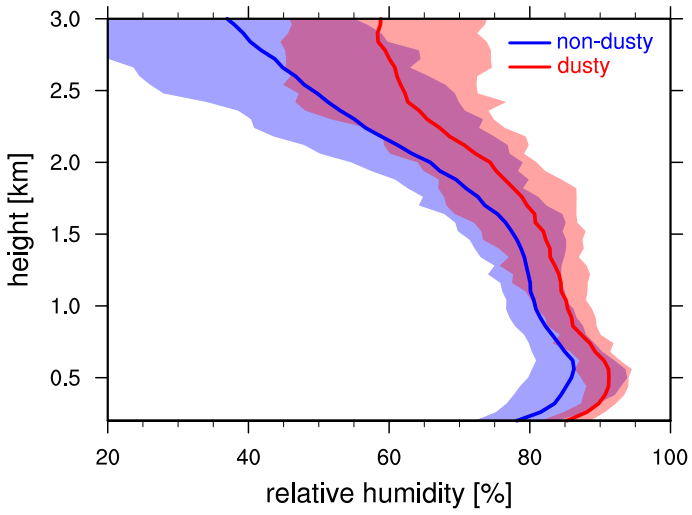

(a) Days with different dust conditions.

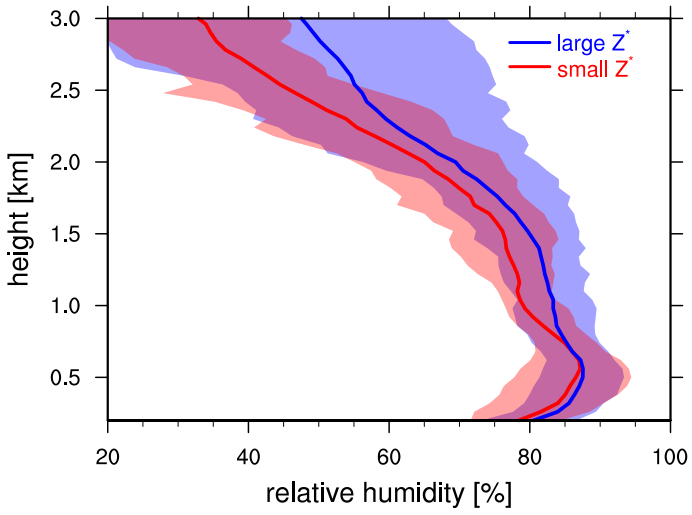

(b) Days with different reflectivities Z^*.

Figure 4.9: Height profiles of averaged daily median relative humidity, $\bar{\eta}$, during non-cloudy conditions measured at nighttime (0 - 8 UTC). Relative humidity is derived from Raman lidar at the BCO. Only measurements are considered when the standard deviation is less than 35% of the actual value. The shadings corresponds to the inner-quartile range.

with total water of the environment ($\tilde{q}$) and the fractional entrainment (ε), which is set to 2 km^{-1} (Stevens et al., 2001). The total water of the environment ($\tilde{q}$) is assumed to decrease linearly with height starting with the saturation specific humidity at cloud base (z_b).

Table 4.2: Typical values of η, β, $\beta^2 N^{-1}$ and N_new at z_1 for shallow clouds with $N = 100\,\mathrm{cm}^{-3}$ are listed. The change in total water inside the cloud with height behaves according to the mass flux equation of Tiedtke (1989) with the environmental total water decreasing linearly with height. $\Delta\mathrm{dBZ} = \mathrm{dBZ}_\mathrm{humid} - \mathrm{dBZ}_\mathrm{dry}$.

$\Delta\eta$ [%]	η_dry[%]	η_humid[%]	β_dry	β_humid	$\beta^2 N_\mathrm{dry}^{-1}$ [10^{-4}cm^{-3}]	$\beta^2 N_\mathrm{humid}^{-1}$ [10^{-4}cm^3]	N_new [cm^3]	ΔdBZ
5.0	77.0	82.0	0.106	0.295	1.124	8.703	773	8.88
1.7	78.3	80.0	0.155	0.219	2.403	4.796	200	3.01
1.0	79.0	80.0	0.181	0.219	3.276	4.796	146	1.64

With this set of equations q_l and β can be computed for different values of η (Table 4.2) for humid (η_humid) and dry conditions (η_dry). So doing demonstrates that the subadiabatic factor β is highly sensitive to surprisingly small changes in η, whereas the resulting impact on Z or the differences between $\mathrm{dBZ}_\mathrm{humid}$ and $\mathrm{dBZ}_\mathrm{dry}$ (ΔdBZ) depend on η itself. For conditions where $\eta_\mathrm{humid} = 80.0\%$ and $\eta_\mathrm{dry} = 78.30\%$, the difference between humid and dry conditions of $\Delta\eta = 1.7\%$ can cause an increase of dBZ = 3 for $N = 100$ cm^{-3}, equivalent to the effect of doubling the number concentration, N. A difference in relative humidity of $\Delta\eta = 5.0\%$ can even cause an increase by dBZ = 8.9, so that N has to increase about eight times to compensate the humidity effects.

According to the simple plume model, an increase of $\Delta N = 29\,\mathrm{cm}^3$ or a decrease of $\Delta\eta = 0.45\%$ can explain the difference between $\beta^2 N^{-1}$ during non-dusty and dusty conditions, assuming $N = 100$ cm^{-3} during non-dusty conditions. But how likely is such a change in $\Delta\eta$ compared to ΔN under realistic conditions of the observed shallow cumulus clouds? To give an estimate about the variability, a scale analysis is undertaken using measurements of N from a field campaign (Siebert et al., 2013) in November 2010. Unfortunately, η could not be measured with the Raman lidar at this time. To obtain an estimate about the variability in η, measurements in 1.5 km height are taken from November 2011.

The relative variability, v_x, of x (here: N or η) during a typical lifetime of such clouds of about half an hour (Saunders, 1965) can be computed with:

$$v_x = \frac{x_{75} - x_{25}}{\bar{x}} \cdot 100\%, \tag{4.11}$$

with the mean of x, $\bar{x}$. Relatively, N varies much more ($v_N = 88.5\%$) compared to η ($v_\eta = 10.8\%$). However, only a scale analysis can infer about the likelihood of ΔN and $\Delta\eta$ by calculating the relative change in x, r_x:

$$r_x = \frac{\Delta x}{x_{75} - x_{25}} \cdot 100\%, \tag{4.12}$$

with the inner-quartile range, $x_{75} - x_{25}$, being an estimate about the variability during the lifetime of a cloud. The relative increase in N ($r_N = 31.7\%$) to balance the difference in $\beta^2 N^{-1}$ is much higher that the relative decrease in η ($r_\eta = 5.3\%$). This demonstrates the higher likelihood of small changes in relative humidity to occur, consistent with a higher impact on $\beta^2 N^{-1}$ than N.

Although dusty samples have a high η (high β) in addition to a high N, we still observe relatively more low $\beta^2 N^{-1}$ than on non-dusty days (Fig. 4.8). What is the reason for this behavior? In the above arguments, we only consider how a change in the averaged relative humidity $\bar{\eta}$ would affect $\beta^2 N^{-1}$. But we can only understand the differences in $\beta^2 N^{-1}$ between non-dusty and dusty days, when we look into the distribution of η across these days (Fig. 4.10). On non-dusty days the distribution in relative humidity is rather

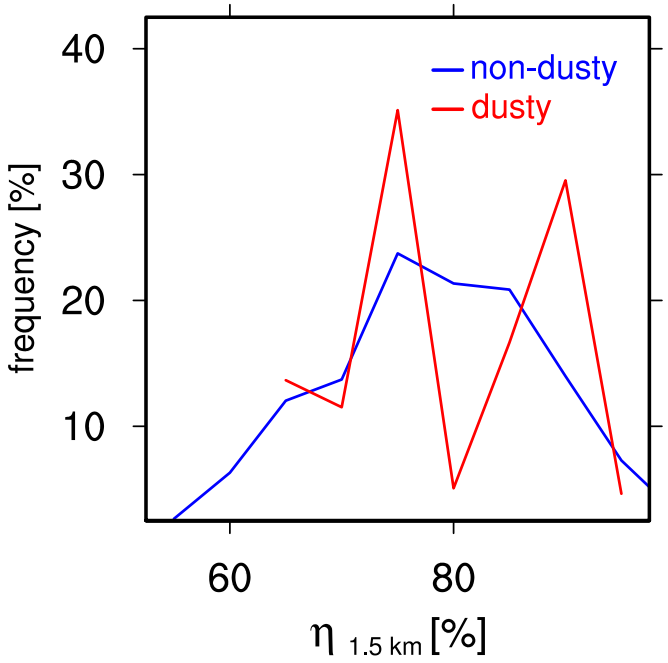

Figure 4.10: Distribution of daily median relative humidity $\eta_{1.5\,\mathrm{km}}$ in 1.5 km height for days with developing cumulus clouds. Blue lines show the frequency per $\Delta\eta = 5\,\%$ for non-dusty days and red lines for dusty days.

homogeneous, whereas on dusty days the distribution is bimodal with a low peak at 70% - 75% and a high peak at 85% - 90%. The latter peak refers to dust events during the humid summer season. This raises the question as to whether $\beta^2 N^{-1}$ differs if one controls for the humidity during the dusty days?

The non-dusty and dusty $\tilde{Z}_z$-profiles are different for $\bar{\eta}_{1.5\,\mathrm{km}} = 70\%$ - 75% but very similar for $\bar{\eta}_{1.5\,\mathrm{km}} = 85\%$ - 90% (not shown). Hence, the low $\beta^2 N^{-1}$ during dusty conditions could be a result of $\tilde{Z}_z$-profiles with a low relative humidity of $h_{1.5\,\mathrm{km}} < 75\%$. However, a

two-sided Kolmogorov-Smirnov test fails to disprove the null-hypothesis for a significance level of 10%, that non-dusty and dusty samples are drawn from the same distribution. In other words, we cannot establish that the Z-profiles differ significantly from each other in the two mentioned humidity ranges.

There is the propensity that this analysis exaggerates the role of β. By focusing on Z, the impact of the liquid water q_l, and hence β, could be overestimated through the strong dependence of Z on the sixth moment of the drop size distribution $n(D)$. In future work, other effects of aerosols might be better explored by using other moments of $n(D)$. Our interest is however on precipitation in shallow trade-wind cumuli, that is explored as a function of N and β.

In summary, the simple entraining plume model shows that the difference in the Z-lapse rate (or $\beta^2 N^{-1}$) between non-dusty and dusty days, and days when clouds have large and small Z^* could solely be explained by subtle differences in relative humidity. This suggest that relatively small variations in relative humidity explain most of the variability of the echo development in shallow cumuli, and therefore the development of precipitation. Because the difference between non-dusty and dusty Z^* estimates can be explained by the bimodality of the relative humidity during dust events, and given the lack of any signal of the aerosol using other methods to infer periods of high versus low CCN concentration we believe that the prime factor regulating the development of precipitation is the adiabaticity of clouds, which depends – based on the present analysis – critically on the ambient humidity.

4.7 Summary and Conclusion

Simultaneous measurements using advanced ground-based lidar and radar remote sensing of aerosol, clouds and meteorological factors are investigated with the purpose of discerning factors influencing the propensity of shallow clouds in the trades to form rain.

Developing cumuli are identified before the onset of active rain and are shown to have a specific signature in the increase of radar reflectivity (Z) with height which is roughly consistent with what is predicted for clouds with a constant droplet number concentration (N) and a fixed sub-adiabatic fraction of liquid water (β). By regressing profiles of Z onto the theoretical predictions for individual developing clouds, a best estimate of $\beta^2 N^{-1}$ can be derived for each cloud. This estimate can in turn be expressed as a single factor, Z^* which measures the best fit profile of reflectivity at a height of 1 km above cloud base.

Keeping in mind that Z^* itself is derived only from the subset of non-precipitating clouds, days on which Z^* is larger than normal are found on the whole to be frequented by clouds that develop precipitation more rapidly, or nearer cloud base, and the fraction of non-precipitating clouds that reach a given height is reduced. This suggests that Z^* is a good proxy for conditions that favor a more rapid onset of precipitation within shallow cumulus.

Factors influencing Z^* are explored in terms of the relative role of the aerosol and meteorological environment. Three methods for discerning aerosol rich from aerosol poor days are developed, but only one (based on a measure about dust) shows significant

differences in Z^* and hence precipitation development. On average, non-dusty days have a nearly twice as large $\beta^2 N^{-1}$ ($1.04 \cdot 10^{-4}$) as dusty days ($0.58 \cdot 10^{-4}$). Nevertheless, the spread in $\beta^2 N^{-1}$ for individual developing shallow cumuli is large. In particular many clouds with high values in $\beta^2 N^{-1}$ are found on dusty days.

The interpretation of these results as being a pure aerosol signal, is questionable, not only because other measures of aerosol amount show no signal. Pronounced seasonality of the dust measure conflates a possible aerosol influence with more systematic meteorological variations, and thus challenges the simple interpretation of the differences in Z^*, on dusty versus non dusty days, as being attributable to aerosol effects.

Raman lidar measurements are used to provide relative humidity profiles through the cloud layer during night time, and it is shown that dusty days, which are more frequent in summer, are on average moister (through the depth of the marine layer) than non-dusty days. When conditioning on a given range of cloud layer relative humidity, no statistically significant differences in Z^* are found between dusty and non-dusty days.

The role of humidity variations in explaining the variability in Z^* is explored through the help of a simple entraining plume model. This model shows that even in a relatively homogeneous environment like that observed, subtle variations in the relative humidity within the cloud layer have a pronounced influence on the sub-adiabaticity of clouds, with β and hence Z^* increasing with humidity in the cloud layer.

The model calculations are sensitive to changes in their assumptions. For example, lowering the fractional entrainment in the massflux equation by Tiedtke (1989) lowers the impact of relative humidity. And if precipitation development is more sensitive to a lower moment of the droplet distribution, the use of Z^* as a precipitation proxy may over emphasize the role of β. Notwithstanding these caveats, the qualitative effects are so large that the dominant effect of small changes in relative humidity is likely to be robust to these caveats. For example, an increase by 2% in relative humidity causes an increase in Z^* commensurate with a twofold increase in N. Even on short time scales it is found that relatively large variations N over a period of a half an hour have a smaller effect on changing Z^* than subtle, and co-varying variations in humidity. This leads us to speculate that a very small ($\sim 3\%$) change in relative humidity in the environment of a cloud likely plays a much larger role in regulating the development of precipitation than do large ($\sim 100\%$) changes in droplet number concentrations.

The implication is that aerosol effects on precipitation are likely very difficult to separate from co-varying meteorological effects. In the context of a changing climate, which continues to warm, but for which further large-changes in the global and remote aerosol amount are not expected, more focus should be put on understanding how shallow cumuli change with subtle changes in their thermodynamic environment.

Chapter 5

Variability of macrophysical properties of trade wind cumuli

5.1 Introduction

The understanding of the driving factors of macrophysical properties of cumulus clouds has been a topic of scientific investigation since Malkus (1958). Warm cumulus clouds in the trades maintain the tropical circulation through their influence on the energy and moisture budget [Riehl and Malkus (1957), and Betts (1997)]. Changes in the properties of cumulus clouds would influence the tropical circulation immediately. In particular, cumulus clouds that start to form precipitation impact the hydrological cycle. Most notably, an understanding on the development of precipitation and how it relates to cloud size and organization is still lacking. In this chapter, the relationship of cloud cover, cloud size distribution and organization of precipitating clouds of trade wind cumuli is explored.

Next to cloud depth and liquid water path, cloud cover affects the amount of solar radiation backscattered into space and the amount of absorbed long wave radiation (Slingo, 1990). Cumulus clouds in the trades account for an average coverage of 12% over the ocean (Warren et al., 1986). Hence, changes in their cloud cover can have a large affect on the Earth's energy cycle. Variations in cloud cover of trade wind cumuli have been studied with observations from space and ground, as well as with models. Estimates of temporal and spatial averaged cloud cover of trade wind cumuli yield about 30%, as obtained by Nuijens et al. (2013) and Kotarba (2010), respectively. Large Eddy Simulation by Neggers et al. (2003) showed, that small clouds contribute most to the total (projected) cloud cover, as confirmed later in observations by Zhao and Di Girolamo (2007).

The ubiquitous small cumulus clouds with diameters below 500 m are found to contribute only little to the overall rainfall (Jiang et al., 2010), which would be consistent with rainfall originating mostly from fewer larger clouds. Indeed, the depth of cumulus clouds correlates with the amount of rainfall, as shown by Short and Nakamura (2000). Johnson et al. (1999) found that almost 60% of all precipitating convective clouds are cumulus clouds with cloud tops between 4.5 km and 9.5 km. A study by Zuidema et al. (2012) even suggests, that the depth of the convective systems correlates with the size of precipitation-induced cold

pools ($\sim$ size of arcs). Arc-shaped clusters of shallow cumuli are reminiscent of these cold pool outflows, that are associated with a production of significant rainfall rates, see alsoSnodgrass et al. (2009). They further propose that the spatial organization of cold pools is important for shallow convection, similar to findings from studies of tropical deep convection (Tompkins, 2001). Large-Eddy-Simulations by Seifert and Heus (2013) support that idea, as they find that cold pools play an important role in the organization of precipitating shallow cumuli.

Woodcock (1940) stated that shallow cumuli are often organized as streets. An early study by Krueger and Fritz (1961) using the first meteorological satellite, TIROS-1, showed cellular patterns of convection over the sea with horizontal diameters of 30 miles to 50 miles. A study by Nair et al. (1998), using Landsat and GOES satellite imagery, suggested that small clouds with a maximum equivalent radius of 300 m strongly cluster, whereas the larger clouds arrange randomly within a scene. Furthermore, small clouds were found to cluster around large ones. This fact is strengthen by Zhao and Di Girolamo (2007), who found about 75% of all clouds are close to other clouds by at most ten times their area-equivalent radius. Furthermore, randomly distributed shallow cumulus clouds or clouds organized in wind parallel streets were identified as being likely non-precipitating, whereas precipitating clouds were found to be deeper ($\sim$ 3 km depth) and organized in successive arcs (Rauber et al., 2007).

Do clouds organize differently if they precipitate (or vice versa)? The present analysis combines observations from space and from ground to better quantify the degree of organization and the contribution of differently sized clouds to the total cloud cover in a trade wind cumulus regime during rainy conditions. For this purpose, one year of observations from space-borne remote sensing measurements with the Advanced Spaceborne Thermal Emission and Reflection Radiometer (ASTER) instrument are analyzed. The advantage of this dataset is the high resolution in space that enables the study of small clouds. An example of ASTER scenes that shows what kind of organization in trade wind cumuli we can expect is shown in Fig. 5.1, with clouds arranged along the edge of a half circle or arc (Fig. 5.1a) and organized in cloud streets (Fig. 5.1b).

The chapter is organized as follows. In section 5.2 the data processing of ASTER data is explained. Section 5.3 discusses how one can identify precipitating clouds from data of KATRIN and ASTER. Cloudiness, i.e. cloud cover, cloud sizes and organization from ASTER during more and less rainy conditions are discussed in section 5.4. Conclusions are presented in section 5.5.

5.2 Methodology

For this study measurements of ASTER and KATRIN are used. As described in chapter 4.3.1, shallow cloud entities have been identified for measurements of KATRIN. Using KATRIN measurements the cloud top, the mean Doppler velocity, and if present, the Z-lapse rate (section 4.3.3) of every cloud entity is calculated. Here, the cloud top marks the height of the highest echo of a cloud entity.

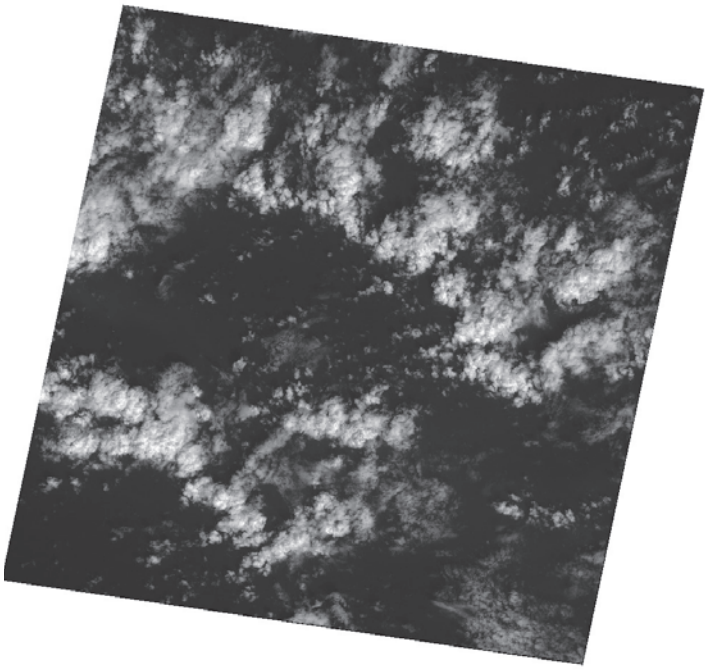

(a) ASTER snapshot on February 7^{th} 2011 at 14:08 UTC, on which BCO reports a large Z^* day.

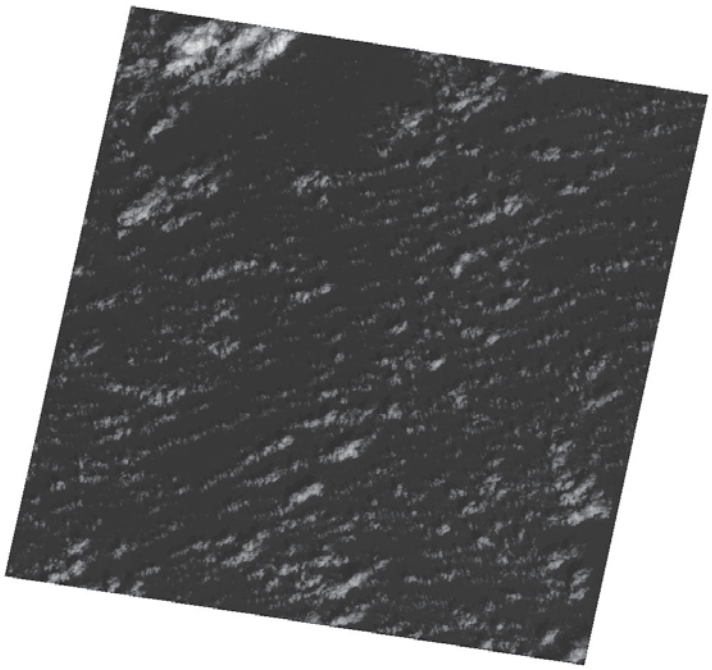

(b) ASTER snapshot on February 10^{th} 2011 at 14:38 UTC, on which BCO reports a small Z^* day.

Figure 5.1: ASTER snapshots close to the BCO in February 2011, observed in the visible channel 1 from the Level 1B product.

We also wish to identify shallow cloud entities for measurements of ASTER. For this purpose, the following steps have to be undertaken. For every pixel in a ASTER scene, reflectance (r) and brightness temperature (T_b) are calculated, and clear and cloudy pixels are identified by using a threshold in r, as described in section 5.2.1. Then, a slightly modified version of the segmentation algorithm, that was used to identify cloud entities from cloud radar retrievals (see chapter 4.3.1) is applied for every ASTER scene. Here "cloudy pixels" with common edges and vertices define a cloud entity. The last step is to filter out "non-shallow" clouds. For this purpose, the calculated brightness temperature is used. The resolution in the TIR channels is 90 m, whereas the resolution in the VIS channels is much higher with 15 m. Hence, brightness temperature has to be interpolated to the resolution of reflectance. Then the number of shallow pixels (see section 5.2.1) within a cloud entity is calculated. A cloud entity is identified as shallow, if this number contributes to more than 60% of the total number of pixels. ASTER scenes with more than 10% cloud cover by non-shallow clouds are excluded. This strict filtering is applied, to insure a consideration of only trade-wind-like conditions. The last step is to filter out sunglint contaminated pixels to avoid erroneous identification of clouds.

When the solar radiation reflects off the ocean at the same angle as a satellite sensor is viewing this surface, sun glint occurs. In the affected areas the rather smooth ocean surface is colored white to gray, which is consistent with a high value in reflectance, and the rougher surface is dark. Sun glint can be identified and filtered out by using its characteristics of having a high reflectance in the visible channel and warm brightness temperature (Frey et al., 2008). That means all cloud entities that have a brightness temperature close to the monthly calculated sea surface temperature (SST) are marked as contaminated by sun glint. In order words, only cloud entities with brightness temperature $<$ (SST - 3.5 K) are considered in the analysis.

In section 5.2.1 a detailed description follows, of how shallow cloudy pixels within an ASTER scene are identified.

5.2.1 Identification of shallow clouds in ASTER data

From the ASTER Level 1 product, a cloud mask is derived. As explained in chapter 2.4, channel 3N (0.76 μm to 0.86 μm) and channel 14 (10.95 μm to 11.65 μm) are used to create such a cloud mask. With measurements in channel 3N the reflectance (r) at the top of the atmosphere (TOA) is computed. The high spatial resolution, and the low atmospheric scatter and absorption of channel 3N, make the measurements well suited to distinguish between clear and cloudy ASTER pixels. Because measurements of reflectance are obtained when the sun shines, only scenes during daytime have been used in this work. Channel 14 gives an estimate about the brightness temperature (T_b) at the TOA, which is used to filter out high clouds, having cold brightness temperatures. Furthermore, channel 14 is least affected by the absorption due to water vapor among all TIR-channels (TIR: 8.13 μm to 11.65 μm).

For the computation of reflectance and brightness temperature at the top of the atmosphere, the spectral radiances [$\mathrm{W\,m^{-2}\,sr^{-1}\,\mu\,m^{-1}}$] in channel 3N and channel 14 have to be computed, respectively. To obtain the spectral radiance the re-calibrated digital

numbers (DN) are multiplied with a unit conversion coefficient (ucc):

$$\text{radiance} = (\text{DN} - 1) \cdot \text{ucc}, \tag{5.1}$$

with ucc = $0.005225\,\mathrm{W\,m^{-2}\,sr^{-1}\,\mu m^{-1}}$ for channel 14 and differing values for channel 3N, depending on the scene: $\text{ucc}_{\text{low}} = 1.15\,\mathrm{W\,m^{-2}\,sr^{-1}\,\mu m^{-1}}$ for a scene with low gain, $\text{ucc}_{\text{nor}} = 0.862\,\mathrm{W\,m^{-2}\,sr^{-1}\,\mu m^{-1}}$ for a scene with normal gain and $\text{ucc}_{\text{high}} = 0.423\,\mathrm{W\,m^{-2}\,sr^{-1}\,\mu m^{-1}}$ for a scene with high gain. The reflectance (r) is then calculated with:

$$\mathrm{r} = \frac{\pi \cdot \text{radiance}_{3\mathrm{N}} \cdot d^2}{I \cdot \cos(\Theta_{\mathrm{s}})}, \tag{5.2}$$

from the solar zenith angle (Θ_{s}), a mean solar exoatmospheric irradiance of $I = 1114\,\mathrm{W\,m^{-2}\,\mu m^{-1}}$ (Thome et al., 2001), and the earth-sun distance d, that differs throughout the year. Θ_{s} is calculated using the solar elevation angle (Θ_{e}), stored in the meta data of each ASTER scene:

$$\Theta_{\mathrm{s}} = (90^{\circ} - \Theta_{\mathrm{e}}). \tag{5.3}$$

Finally, the inverse of the Planck formula is applied to calculate the brightness temperature (T_b):

$$\mathrm{T}_b = \frac{\mathrm{K}_2}{\ln\left(\frac{\mathrm{K}_1}{\text{radiance}_{14}} + 1\right)}, \tag{5.4}$$

by using the two parameters, $\mathrm{K}_1 = 641.326517\,\mathrm{W\,m^{-2}\,\mu m^{-1}} = \mathrm{C}_1\,\lambda^{-5}$ and $\mathrm{K}_2 = 1271.221673\,\mathrm{K} = \mathrm{C}_2\,\lambda^{-1}$, with the effective wavelength of channel 14, $\lambda = 11.318\,\mu\mathrm{m}$, $\mathrm{C}_1 = 1.19104356 \cdot 10^{-16}\ \mathrm{W\,m^2}$ and $\mathrm{C}_2 = 1.43876869 \cdot 10^{-2}\ \mathrm{m\,K}$.

To distinguish between cloudy and clear pixels a threshold in reflectance is used. This threshold is allowed to vary with time. Compared to other studies, which used manually selected thresholds for every ASTER scene (Zhao and Di Girolamo, 2007), we account for variations in a threshold in reflectance in a more systematic way. It is expected that the reflectance of the ocean (clear pixels) and of clouds varies mainly according to the variation in the solar zenith angle throughout the year, as shown in Fig. 5.2a. Of course, variation in surface wind speed, causing variations in waves of the ocean can also modulate the reflectance.

The minimum reflectance ($r_{\min}$) is plotted as a function of month in Fig. 5.2a. Here, at least one non-cloudy pixel is assumed to be present in almost every scene, which makes $r_{\min}$ representative for the reflectance of the ocean. The box-and-whisker plot shows the variation in $r_{\min}$ among all scenes for every month. Here, $r_{\min}$ and its inner-quartile range vary throughout the year with high values from April to August. The inner-quartile range in June 2011 is remarkably small because only scenes from one day were available (only 11 scenes). Hence, the small spread is not representative for the whole month. The variation in the mean in $r_{\min}$ ($\mu_{r_{\min}}$) follows qualitatively the solar insolation (when neglecting the month of June). To distinguish cloudy from clear pixel a threshold in reflectance for every month is assigned of $2 \cdot \mu_{r_{\min}}$. With this threshold some variations in the ocean's reflectance is allowed for, e.g. high values in reflectance caused by breaking waves in high surface wind conditions.

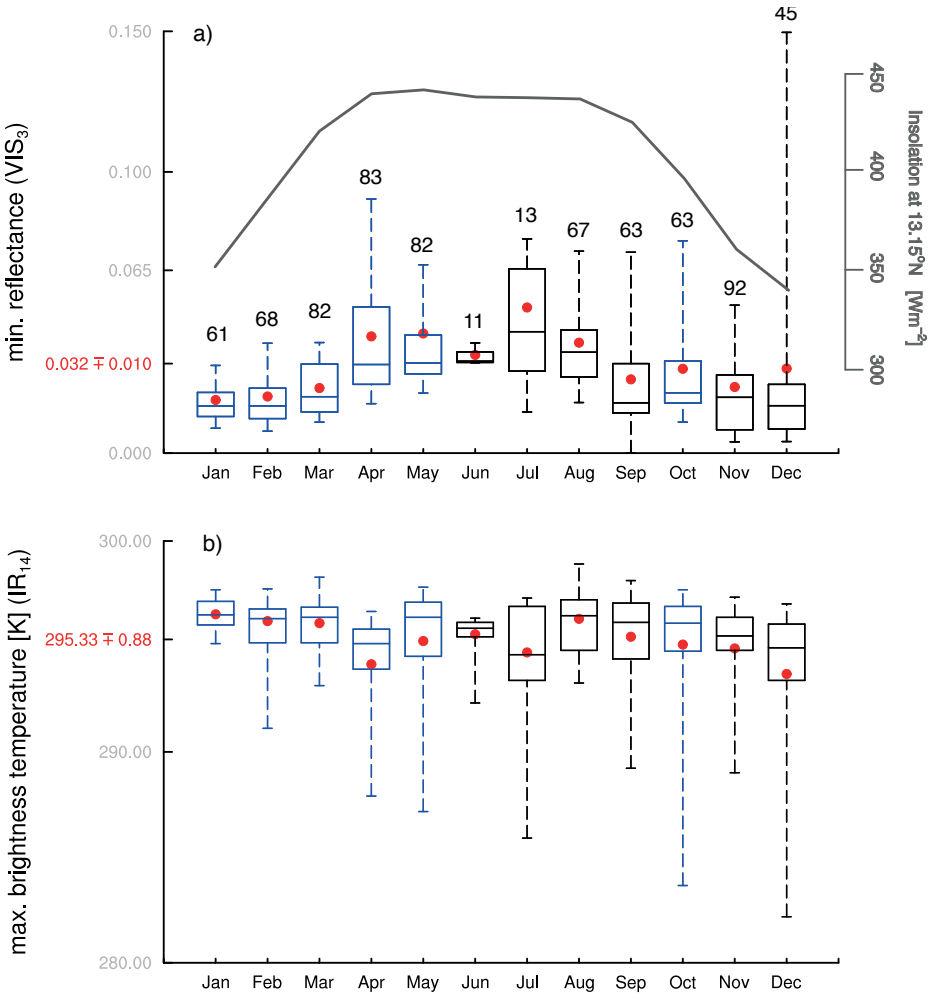

Figure 5.2: Box-and-whisker plot of a) minimum reflectance (r_{min}) and b) maximum brightness temperature ($T_{b,max}$) measured with ASTER for all months in 2011. Box and whiskers display the monthly range from the 5th percentile, 25th percentile, median, 75th percentile to the 95th percentile. The red dots mark the monthly mean. The red value on the y-axis is the yearly mean ± its standard deviation. The blue colored boxes highlight the months when measurement from both KATRIN and ASTER are available and the numbers above the box and whiskers display the number of scenes per month. On the left side in a) the annual variation in solar insolation, representative for Barbados, is displayed.

To filter out high clouds the maximum brightness temperature ($T_{b,max}$) is used. The ocean is warmer compared to any cloud. Hence, $T_{b,max}$ can be seen as a measure of sea surface temperature (SST) when assuming at least one non-cloudy pixel to be present in almost every scene. Our aim is to keep clouds which have tops $\sim$ 3.5 km and lower. When assuming a dry adiabatic lapse rate in temperature of 10 K km^{-1} from the surface to a typical cloud base of 700 m (Nuijens et al., 2013) and a moist adiabatic lapse rate of

$6\,\mathrm{K\,km^{-1}}$, the temperature at 3 km height is 21 K colder than the SST. To allow for some variations in $\mathrm{T}_{b,\mathrm{max}}$ during a month an extra 3.5 K is subtracted. This value represent the maximal value of the monthly inner-quartile range and is consistent with a height difference of 700 m. To distinguish shallow clouds from non-shallow clouds a threshold in $\mathrm{T}_{b,\mathrm{max}}$ for every month is assigned of $\mu_{\mathrm{T}_{b,\mathrm{max}}} - 21\,\mathrm{K} - 3.5\,\mathrm{K}$, with the monthly mean in the maximum brightness temperature, $\mu_{\mathrm{T}_{b,\mathrm{max}}}$. This threshold is consistent with sampling of clouds having a maximum in z_t of about 3.7 km. Every cloudy pixel which is colder than this threshold is classified as non-shallow. Future studies that are interested in even deeper clouds can adjust the threshold in $\mathrm{T}_{b,\mathrm{max}}$ to even lower values. As displayed in Fig. 5.2b, the variation in $\mathrm{T}_{b,\mathrm{max}}$ throughout the year is small. Hence, the threshold in $\mathrm{T}_{b,\mathrm{max}}$ is expected to vary only little through the year.

One could have picked different values for this threshold, e.g. the 5^{th} percentile for reflectance or 95^{th} percentile for brightness temperature, which would account for some variations in the two quantities during a month. In Fig. 5.3a the reflectance is displayed, averaged over all scenes in a month for all percentiles in reflectance. Some months, which are identified through visual inspection to be more cloudy than others (e.g. July), have a much higher value in the 5^{th} percentile compared to r_{min}. During months that are less cloudy (e.g. January), the averaged reflectance agrees better between the 5^{th} percentile and r_{min}. The choice to use r_{min} to distinguish between cloudy and clear pixels is hence a more reliable measure, than using the 5^{th} percentile, which could already include some measurements of thin clouds in a scene with high cloud cover. Even though not as evident as for reflectance, months with higher cloud cover (e.g. July) seem to have lower mean brightness temperatures in the higher percentiles (Fig. 5.3b). That means, almost all pixels in those ASTER scenes are cloudy. Our choice of $\mathrm{T}_{b,\mathrm{max}}$ to create a threshold which filters out high clouds seems to be less affected by the amount of cloudiness.

There are two caveats in the way to detect clouds in ASTER scenes. The first relates to the fact that ASTER only measures column-integrated radiances. That means that during times of multi-layer clouds the measured radiance is a signal of the sum of two or more clouds. In this case, one would identify a shallow cloud or non-shallow cloud depending on the thickness of the individual clouds, and hence their contribution to the overall signal in radiance. For example, a non-shallow cloud would be detected when a thick high-level cloud obscures a thin low-level cloud. However, the described multi-layer situation should be rather seldom in the trades. Only during situations of thick and thin low-level clouds of different depths and thin high-level cirrus clouds a false identification of clouds is possible. To avoid multilayer situations of high and low-level clouds only ASTER scenes with less than 10% cloud cover by high-level clouds are studied in this work. The second caveat is based in the cloud detection approach, as it only calculates the reflectance (r) and brightness temperature (T_b) at the top of the atmosphere (TOA). To obtain accurate measures of r and T_b, one should calculate those measures at the ocean surface which takes into account the contribution of the atmosphere on the measured radiances. Our interest, however, is only on the identification of shallow clouds in a qualitative sense, that means very accurate estimates in reflectance and brightness temperature are not from interest. The cloud detection approach developed here is sufficient for the investigation of the relationship of cloud cover and cloud size distribution of shallow cumulus clouds,

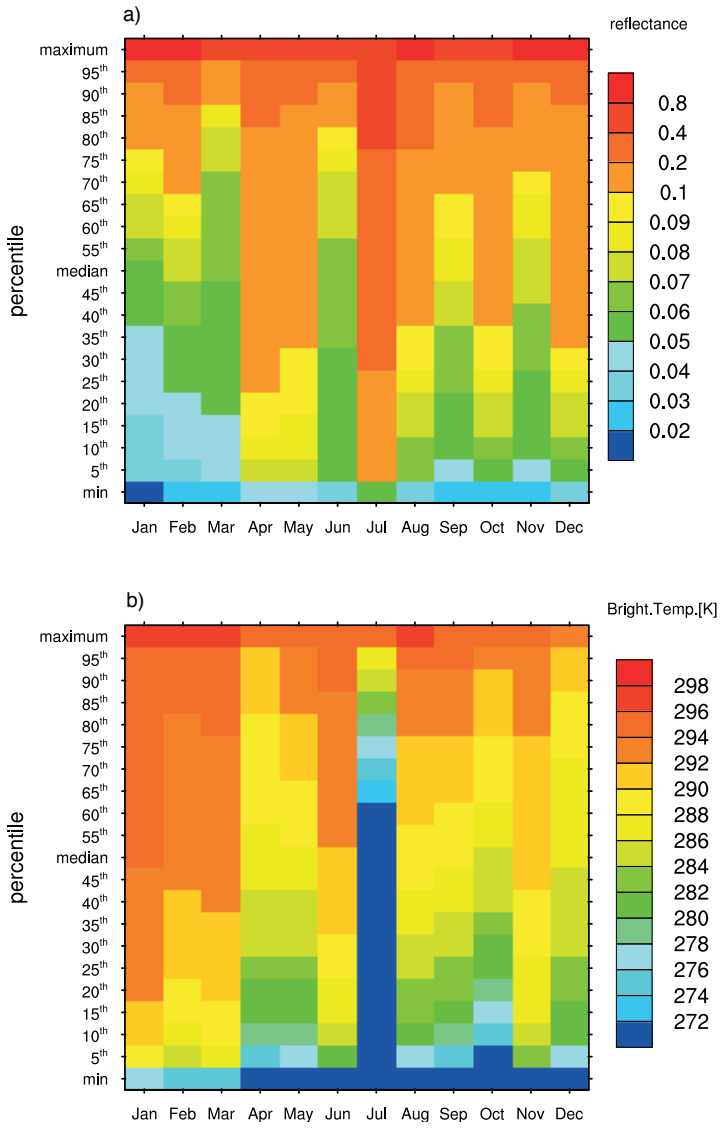

Figure 5.3: Monthly means in a) reflectance and b) brightness temperature for all percentiles (plus minimum and maximum) and all months in 2011.

which is thought to be insensitive to such distinctions.

5.3 Characteristics of raining clouds

Before investigating the cloud size distribution and the degree of organization of precipitating trade wind cumuli, we investigate whether during times of rain clouds are deeper. If such a relationship exists, the depth of a cloud or its cloud top height (z_t) could be used as a proxy for rain to study the degree of organization of precipitating trade

wind cumuli with measurements of ASTER, as no information on rain but on z_t ($\sim T_b$) is available for this dataset. To find a relationship between rain and cloud top height, measurements of the KATRIN cloud radar at the Barbados-Cloud-Observatory (BCO) are investigated.

In chapter 4 it was shown that Z^* is a good measure for identifying clouds with a higher propensity to form rain. Here, Z^* was calculated using the reflectivity values measured by KATRIN for every developing (non-precipitating) cloud. We may investigate how Z^* relates to the amount of rain and the depth of clouds by analyzing the cloud characteristics in the KATRIN data during days with a large Z^* and a small Z^*. Furthermore, the cloud radar data is segregated into days with clouds having a high z_t and a low z_t, to test if the rain amount is similar compared to rain amount on a large Z^* day and a small Z^* day (section 5.3.1). An example of two ASTER scenes with different cloud patterns are shown in section 5.3.2 including a brief discussion on the expectation in cloud organization on a rainy and a non-rainy day.

5.3.1 Cloud characteristics from KATRIN

Fig. 5.4 shows how frequent clouds with a certain cloud top height occur for height levels of 30 m using measurements from KATRIN between January 2011 and March 2012. The data is conditional sampled for very rainy and less rainy days, and for days with a large Z^* and small Z^*. Very rainy days are identified as days having a higher daily rain amount than the 75$^{\text{th}}$ percentile of all daily rain amounts, and less rainy days have a smaller daily rain amount than the 25$^{\text{th}}$ percentile.

In general, a peak in the occurrence of clouds with tops of 1 km is visible with a steep decay for clouds having higher cloud tops. This distribution is very similar between less rainy and small Z^* days, and very rainy and large Z^* days. The peak around 1 km is larger with ~ 8 % for less rainy ($\widehat{z}_t = 1192$ m) and small Z^* days ($\widehat{z}_t = 1290$ m) than during very rainy and large Z^* days with ~ 3 %, with the mean in cloud top height, $\widehat{z}_t$ (see Table 5.1). However, rainy days have on average deeper clouds with $\widehat{z}_t = 2418$ m than on large Z^* days with $\widehat{z}_t = 1922$ m. As discussed in section 4.4, Z^* is a good measure for the onset of precipitation, but may not be the best predictor for actual rain amount.

An estimate about the daily rain amount of ground-based precipitation can be approxi-

Table 5.1: The 25$^{\text{th}}$ percentile ($z_{t_{25}}$) of cloud top height (z_t) as well as its median ($\widetilde{z}_t$), the 75$^{\text{th}}$ percentile ($z_{t_{75}}$) and the mean ($\widehat{z}_t$) in meters.

	very rainy	less rainy	large Z^*	small Z^*
$z_{t_{25}}$	929	929	899	959
$\widetilde{z}_t$	1289	1049	1109	1079
$z_{t_{75}}$	2938	1229	2219	1319
$\widehat{z}_t$	2418	1192	1922	1290

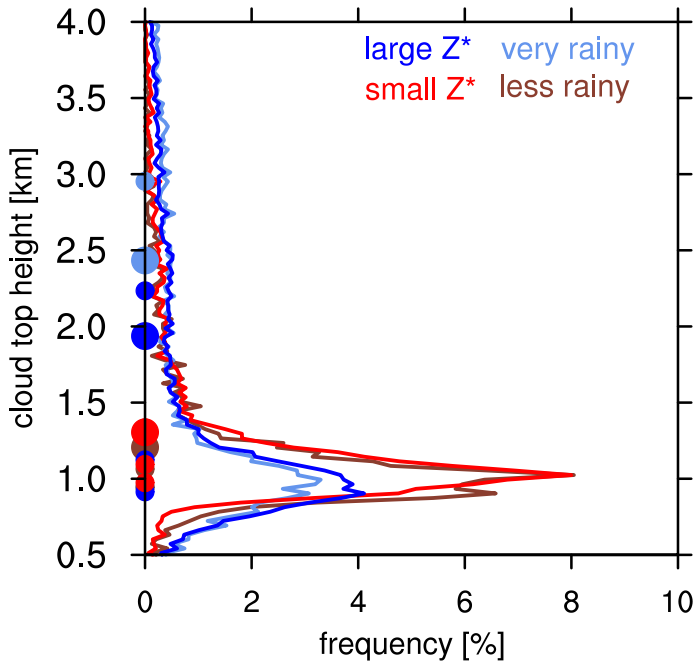

Figure 5.4: Frequency [%] of detecting clouds having a certain cloud top height (z_t) for height levels of 30 m compiled from KATRIN data, measured between January 2011 to March 2012. The measurements are segregated into days which are very rainy (colored in cyan), less rainy (colored in brown), have a large Z^* (colored in blue), and have a small Z^* (colored in red). The small dots on the y-axis from bottom to the top represent the 25th percentile ($z_{t_{25}}$), the median ($\widetilde{z}_t$) and 75th percentile ($z_{t_{75}}$), and the large dot represents the mean ($\widehat{z}_t$) in cloud top height.

mated from reflectivity measurements in 300 m height using a relationship between Z and rain rate, R. Here, the Z-R relationship by Nuijens et al. (2009) is taken:

$$Z = 248R^{1.75}, \tag{5.5}$$

with the rain rate, R, in mm h^{-1} and reflectivity, Z, in mm^6 m^3. The rain amount during a day is then simply the sum over rain rate. The frequency in daily rain amount (with a binning of 1 mm d^{-1}) is displayed for days with high z_t and days with low z_t, as well as for large Z^* days and small Z^* days in Fig. 5.5. A day with a high z_t is identified as a day with clouds having a higher daily mean cloud top height than the 75th percentile of all daily cloud top heights, and a day with a low z_t has clouds of a smaller daily mean cloud top height than the 25th percentile. Days with high z_t show higher daily rain amounts (6.76 mm d^{-1}) than days with low z_t (0.30 mm d^{-1}). The same is true for large Z^* days (3.91 mm d^{-1}) and small Z^* days (0.39 mm d^{-1}). Here, z_t seems to be a better measure of rain amount, but Z^* is still a reasonable measure to identify rainy and non-rainy days. This behavior goes in hand with the previous finding, showing that Z^* might not be the

best predictor for actual rain amount.

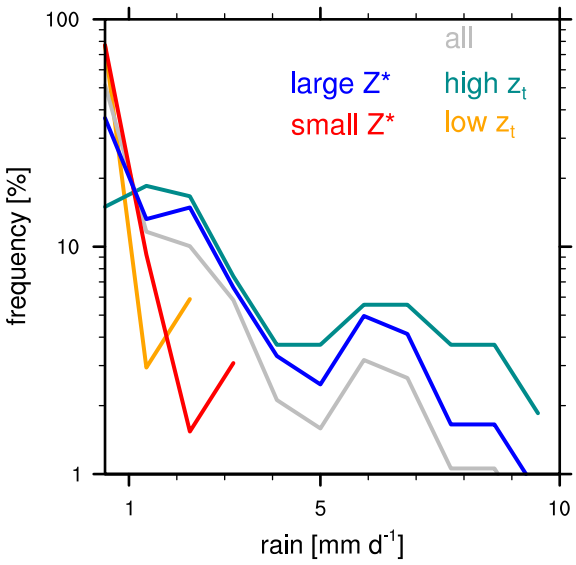

Figure 5.5: Frequency of occurrence [%] of daily rain amount [mm d^{-1}] for conditional samples on all days (colored in gray) days with high z_t (colored in turquoise) days with low z_t (colored in orange) large Z^* days (colored in blue) and small Z^* days (colored in red). On low z_t days and on small Z^* days no data was available for higher rain amounts. Normalization is done for every conditional sample by the sum over daily rain amount. A binning of 1 mm d^{-1} is used. Here, measurements by KATRIN were obtained between January 2011 and March 2012.

In summary, Z^* was found to be a good predictor of cloud top height. Large Z^* days and very rainy days are marked by much deeper clouds than clouds on small Z^* days and less rainy days. Furthermore, days with clouds of different depths have similar statistical characteristics in rain amount as clouds on different Z^* days. Small differences in the depth ($\sim z_t$) of clouds and the amount of rain remain. We conclude, that both measures, namely Z^* and cloud top height, can be used to identify conditions being more and less rainy. In section 5.4, the information about the cloud depth is used to investigate the cloud size distribution and organization during rainy and non-rainy conditions with measurements of ASTER.

5.3.2 Case study

Assuming that the point measure Z^* could be used for the identification of rain conditions in ASTER scenes, then deeper clouds organized in arcs would be expected on a large Z^* day and more shallow clouds organized in streets or randomly distributed would be expected on a small Z^* day. In Fig. 5.1 two ASTER scenes are shown, one on a large Z^* day

(February 7$^{\text{th}}$ 2011) and one on a small Z^* day (February 10$^{\text{th}}$ 2011). With measurements from KATRIN, the mean cloud top height on a the large Z^* day is computed with 1964 m and the daily cloud cover $\text{cc}_{\text{day}} = 13.75\%$. The clouds appear more massive and shaped like arcs, in the corresponding ASTER scene. The rain amount on the large Z^* day is 1.75 mm d^{-1}, whereas on the small Z^* day no rain is recorded, which highlights once again, that Z^* is a good measure for precipitation (and its onset). Compared to the large Z^* day, the mean cloud top height on the small Z^* day is smaller (1154 m) and the daily cloud cover is reduced ($\text{cc}_{\text{day}} = 4.48\%$) at the BCO. Here, the clouds in the corresponding ASTER scene are organized in streets (Fig. 5.1b).

This example would suggest to use Z^* as an indicator of precipitation for all ASTER scenes, even the ones far away from the BCO, which could be located up to 1000 km upstream (see Fig. 2.13). However, a visual inspection of all scenes taken on both days, reveals a large variety in the degree of organization, like randomly distributed clouds on large Z^* days and arc-shaped clouds on small Z^* days. To avoid false interpretation of cloud characteristics from ASTER scenes by using the point measure Z^*, we instead transfer the relationship between large Z^* days and clouds with high cloud top heights, obtained with the cloud radar data, to measurements of ASTER. That means, the cloud top height in form of brightness temperature in ASTER scenes is used to identify a scene as rainy.

5.4 Characteristics of cloudiness in the trades

Macrophysical properties of trade wind cumuli can be measured with ASTER and KATRIN. Because of differences of the two instruments, however, a combined usage is difficult: (i) KATRIN operated mostly during the dry winter season, whereas ASTER measurements are available for the whole year of 2011. (ii) Cloud cover estimates by KATRIN are an average in time compared to the spatial average in cloud cover with ASTER. (iii) Measurements of KATRIN capture clouds which are closest in time, whereas ASTER captures clouds which are closest in space. In this analysis, the macrophysical characteristics of trade wind cumuli are studied with measurements by ASTER. This allows to investigate differences in cloudiness between the wet summer season and dry winter season, and gives an estimate of the spatial organization. In the future more measurements from KATRIN will be available, which will enable to capture the seasonality in cloudiness. Those measurements could be compared to measurements from ASTER to investigate if the seasonality in cloudiness from 2011 is a prominent feature over longer timescales.

According to Brueck (2012), the months December to May define the dry season and June to November the wet season. For the remaining work 495 ASTER scenes with less than 10% high-level clouds during daytime are analyzed. Measurements by ASTER are segregated into scenes with high z_{t} and with low z_{t}. As the focus of this study is to distinguish non-rainy and rainy conditions a rather strict threshold is set. That means we identify non-precipitating scenes by the occurrence of very shallow clouds ($z_{\text{t}} \leq 1$ km) and precipitating scenes by the occurrence of deeper clouds (cloud top height ≥ 3 km). For this purpose, a scene with high z_{t} is identified, when having a mean T_b of 274 K and less, which corresponds to a cloud top height of 3 km and higher, and a scene with low z_{t} is

identified when having a mean T_b of 286 K and higher, which corresponds to a cloud top height of 1 km and less. Because the brightness temperature does not vary much (see Fig. 5.2) a fixed threshold in T_b is used to distinguish between scenes with high and low z_t.

5.4.1 Cloud cover

The projected cloud cover (cc) is defined as the ratio of number of cloudy pixels to the total number of pixels and is shown for all scenes in 2011 in Fig. 5.6a. Here, the mean in cloud cover is 31.5% with 40% of all scenes having a cloud cover up to 8% . The distribution shape in projected cloud cover is similar to findings by Zhao and Di Girolamo (2007), who identified 152 ASTER scenes (September to December 2004) with shallow clouds by visual inspection. However, their mean in cc is reduced by a factor of four compared to this study. This is most probably due to the different sampling and the amount of analyzed ASTER data (four months versus one year).

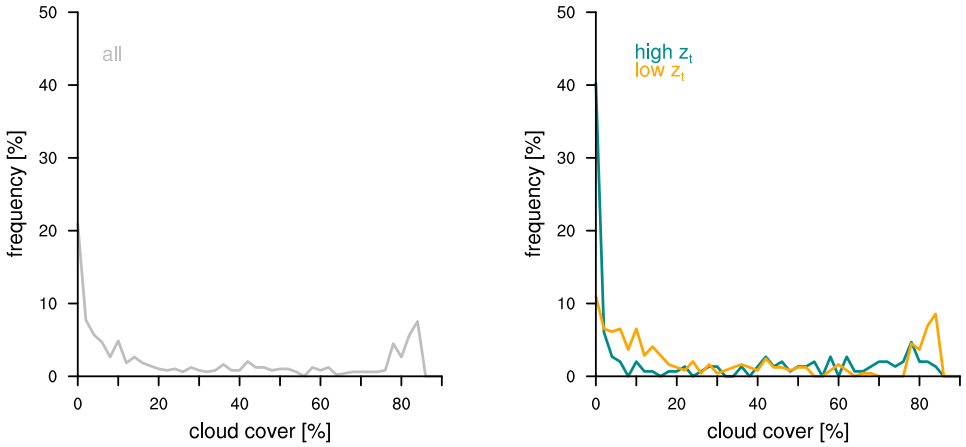

(a) Projected cloud cover (cc) of all clouds from ASTER scenes.

(b) Projected cloud cover (cc) of deep and shallow clouds from ASTER scenes.

Figure 5.6: Frequency of occurrence [%] of cloud cover (cc) for a) all scenes (colored in gray) and b) high z_t (colored in turquoise) and low z_t scenes (colored in orange) with shallow clouds obtained from ASTER scenes in 2011, binned for every cc = 1%.

In Fig. 5.6b the cloud cover is displayed for all scenes with a mean cloud cover of cc = 31.5%, for high z_t scenes with a mean cloud cover of cc = 27.8% and low z_t scenes with a mean cloud cover of cc = 33.5%. It is interesting to see, that a lower cloud cover has been found for scenes with high z_t, as one could think of clouds with higher z_t being deeper and wider or more numerous, and hence contributing to a higher cloud cover compared to clouds with low z_t. This simple assumption of deeper clouds having larger horizontal

dimensions or being more numerous might not be true for trade wind cumuli. To study this in more detail, the seasonality in cloud cover is analyzed.

Brueck (2012) and Nuijens et al. (2013) showed that the region around Barbados experiences two seasons characterized by a different structure in the clouds. The suppressed winter season (December to May) with stronger, more north-easterly winds experiences enhanced lateral cloud spreading close to an inversion or in times of high stability, whereas in the convective summer season (June to November) with higher relative humidity the mean wind advects more vigorous convective clouds during times of lower tropospheric stability. That means during the dry winter season one would expect clouds with high z_t being wider, leading to a higher cloud cover than during the wet summer season.

Table 5.2: Mean in projected cloud cover [%] for all ASTER scenes in 2011, during the dry winter season (December - May) and wet summer season (June - November) for all scenes, scenes with high z_t and scenes with low z_t.

	whole year	dry season	wet season
all	31.5	31.3	31.9
high z_t	27.8	30.3	23.3
low z_t	33.5	31.4	37.3

Tab. 5.2 shows the mean in projected cloud cover with a similar overall cloud cover between different seasons. Scenes with high z_t have a lower cloud cover during the wet season (= 23.3%) than during the dry season (= 30.3%), which translates to an increase in cloud cover in the dry season of about one half compared to the cloud cover in the wet season. This increase in cloud cover for scenes with high z_t is consistent with the existence of layers of stratus clouds close to the inversion during the winter, as discussed by Nuijens et al. (2013). Scenes with high z_t have a very similar cloud cover compared to scenes with low z_t during the dry winter season, whereas during the wet summer season the cloud cover is significantly increased for scenes with low z_t. To be able to explain these differences for scenes with high z_t and low z_t during the two seasons, one has to study which cloud sizes contribute most to the total cloud cover.

5.4.2 Cloud size distribution

The normalized cloud size distribution is the ratio of the number of clouds of a certain size (= cloud size density, $n(D)$) to the total number of clouds, with cloud size defined as the square root of the area of a cloud entity. Many previous studies (e.g. Benner and Curry (1998)) showed that the cloud size distribution behaves like a power law:

$$n(D) = a \cdot D^b, \tag{5.6}$$

with the cloud size density $n(D)$, cloud size (D) and the parameters, a and b. The integral over $n(D)$ represents the total number of clouds. The slope parameter, b, gives information about which cloud sizes contribute most to the total projected cloud cover (cc). As cloud

cover relates to D^{b+2}, cc is dominated by small clouds for $b < -2$, and dominated by large clouds for $b > -2$.

For better visualization cloud size density is often plotted on a log-log scale. According to Neggers et al. (2003), the cloud size density on a logarithmic D-scale relates to the cloud size density on a linear D-scale in the following way:

$$\begin{aligned} n(\log D) &= n(D)\frac{\mathrm{d}(D)}{\mathrm{d}(\log D)}, \\ &= n(D) \cdot D \cdot \ln 10, \\ &= a^* \cdot D^{b+1}, \end{aligned} \tag{5.7}$$

where $a^* = a \cdot \ln 10$. Note, $n(\log D)$ behaves also like a power law with a slope parameter of $(b+1)$.

In Fig. 5.7a the normalized cloud size distribution is shown on log-log axes for cloud sizes up to 10 km with a binning of 33.5 m in clouds size, which is consistent with 5 pixels. The fraction of different cloud sizes is calculated first for every scene, and then averaged and normalized over all scenes. The slope parameter b is obtained for all cloud sizes that contribute 99% to the total number of shallow clouds. This limitation to a range of cloud sizes is necessary because the linear fit generates more weight to large clouds (Zhao and Di Girolamo, 2007). Therefore, one has to be careful considering large-sized clouds that are poorly sampled. Additionally, we do not assume any scale break by calculating two different slope parameters for small and large clouds, as done before by e.g. Benner and Curry (1998) and Nair et al. (1998). Based on Heus and Seifert (2013), one could think that this artificial scale break is induced by poorly sampled large clouds.

For all ASTER scenes in 2011 the slope parameter of b = -1.21 is calculated, which is consistent with a high contribution of large clouds to the total cloud cover. What is the slope parameter for ASTER scenes with high z_t? Is the contribution of large clouds to the total cloud cover even higher? In Fig. 5.7b a high fraction of small clouds in scenes with low z_t can be seen compared to scenes with high z_t. The fraction of small clouds, however, is poorly represented in the corresponding slope parameter, because of the higher weighting of large clouds due to the linear fit between $\log(n(\log D))$ and $\log D$. That means, the slope parameters between ASTER scenes with low z_t and with high z_t can be very similar, despite a difference in the fraction of small clouds. Indeed, the slope parameter of -1.25 for scenes with low z_t is similar to the slope parameter of -1.21 for scenes with high z_t (Tab. 5.3). This similarity in b would be consistent with a similar contribution of large clouds to the total cloud cover for non-rainy ($\sim$ low z_t) and rainy ($\sim$ high z_t) conditions. Is this true for different cloud types?

The contribution of certain cloud sizes to the total cloud cover is analyzed for the dry winter season and wet summer season, as the seasons are characterized by the predominance of different cloud types (see section 5.4.1). As listed in Tab. 5.3, for all ASTER scenes the slope parameter is higher during the dry winter season compared to the wet summer season. This implies that large clouds contribute more to the overall projected cloud cover in winter than in summer, which is consistent with a prevailing stratus layer in winter compared to more vigorous convective clouds in summer (see Nuijens et al. (2013)).

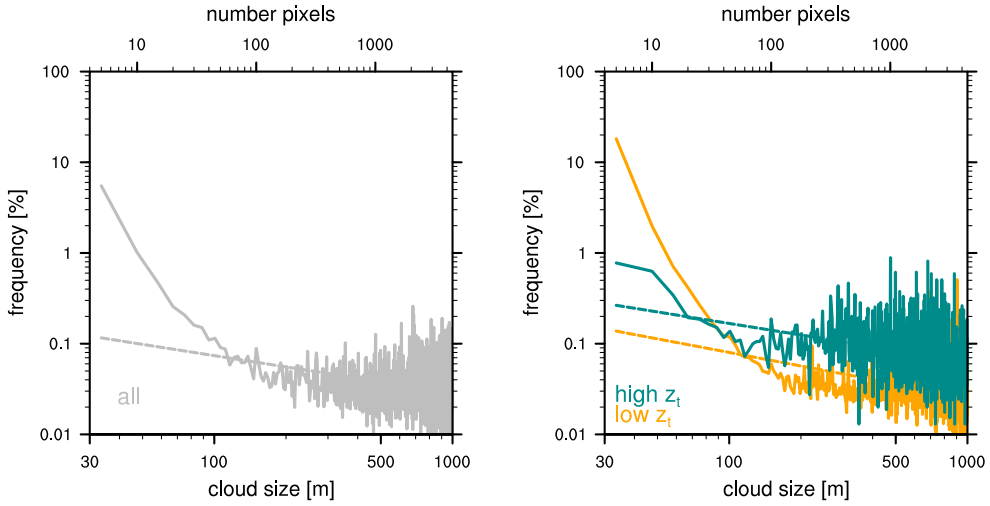

(a) All clouds from all available ASTER scenes.

(b) Deep and shallow clouds from all available ASTER scenes.

Figure 5.7: Normalized cloud size distribution on log-log axes for shallow clouds from a) all scenes (colored in gray) and b) high z_t (colored in turquoise) and low z_t scenes (colored in orange) obtained from ASTER scenes in 2011. The dashed lines correspond to linear fits by a power law [Eq. (5.7)]. The binning of 5 pixels is chosen for cloud size.

Table 5.3: Slope parameter for all ASTER scenes in 2011, during the dry winter season (December - May) and wet summer season (June - November) for all scenes, scenes with high z_t and scenes with low z_t.

	whole year	dry season	wet season
all	-1.21	-1.23	-1.41
high z_t	-1.21	-1.18	-1.18
low z_t	-1.25	-1.27	-1.42

Most evident during the wet summer season, the slope parameter for ASTER scenes with high z_t is larger than for scenes with low z_t. That means larger clouds contribute more to the total projected cloud cover (cc) in scenes with high z_t. As shown in section 5.4.1, during summer ASTER scenes with high z_t have a reduced total cloud cover compared to scenes with low z_t. In fact, knowing that large clouds contribute more to the total cloud cover than small clouds, the number of large deep clouds has to be small to be able to explain the low cloud cover in ASTER scenes during the convective summer season. Based on findings by Seifert and Heus (2013), one could expect a certain degree of organization of those large convective clouds with a high cloud top assuming that they are precipitating.

5.4.3 Spatial distribution

To undertake a conscientious investigation of organization, an analysis on the sensitivity of the distribution between different random cloud fields and observed cloud fields is necessary. This study concentrates on the spatial distribution of clouds to their neighbors, that means the nearest neighbor distance (NND) is obtained for every cloud within one ASTER scene. For this purpose, the mass center of every cloud is calculated (Benner and Curry, 1998) and its euclidean distance to the nearest cloud. Because the minimum distance to the neighboring clouds is limited by the cloud size itself, NND is normalized by the cloud size.

The distribution of the mean in $\mathrm{NND} \cdot \mathrm{size}^{-1}$ for shallow clouds in ASTER scenes in 2011 is displayed in Fig. 5.8. On the left side, the distribution of $\mathrm{NND} \cdot \mathrm{size}^{-1}$ for large and small clouds is shown. The size of a cloud is defined by the number of pixels, with large clouds having 50 pixels and more and small clouds having 5 pixels and less. The size of the neighbors of large and small clouds is not restricted. On the right side, the

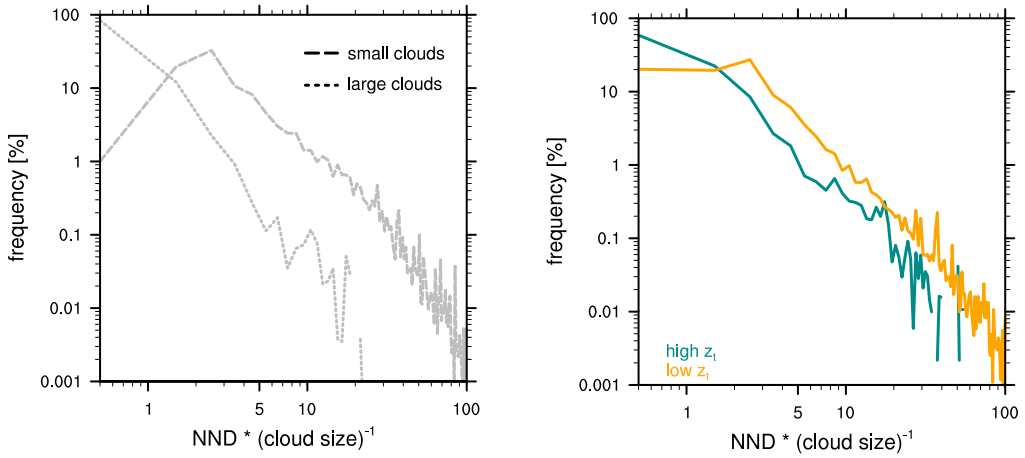

(a) Large and small clouds from all available ASTER scenes.

(b) ASTER scenes with deep and shallow clouds.

Figure 5.8: Normalized distribution of $\mathrm{NND} \cdot \mathrm{size}^{-1}$ of trade wind cumuli retrieved with ASTER in 2011 with a binning of one. a) shows the distribution for large (dotted line) and small (dashed line) clouds from all available data, and b) shows distribution for ASTER scenes with high z_t, (colored in turquoise), and scenes with low z_t (colored in orange).

distribution of $\mathrm{NND} \cdot \mathrm{size}^{-1}$ for scenes with high and low z_t is shown. 59% of all clouds in ASTER scenes with high z_t have their nearest neighbor within a distance of 1 times less than their cloud size, whereas only 20% of all clouds in ASTER scenes with low z_t have the same nearest neighbor distance. In other words, scenes with high z_t have an increased tendency to cluster compared to scenes with low z_t. In particular, large clouds show this high occurrence of small $\mathrm{NND} \cdot \mathrm{size}^{-1}$ (Fig. 5.8a) in scenes with high and low z_t (not shown). Additionally, small clouds in scenes with high z_t are found to cluster more than in scenes with low z_t. As ASTER scenes with high z_t have more large clouds than scenes with low z_t

(section 5.4.2), the high occurrence of small NND $\cdot$ size^{-1} is mainly caused by large clouds in ASTER scenes with high z_t.

Table 5.4: Fraction of clouds [%] with nearest neighbor within a distance of 1 times less than their cloud size (NND $\cdot$ size^{-1} < 1) for all ASTER scenes in 2011, during the dry winter season (December - May) and wet summer season (June - November) for all scenes, scenes with high z_t and scenes with low z_t.

	whole year	dry season	wet season
all	35.8	39.6	33.1
high z_t	58.8	58.7	58.9
low z_t	20.2	23.3	18.3

The high occurrence of NND $\cdot$ size^{-1} < 1 is evident in the dry winter season and the wet summer season for all ASTER scenes, as displayed in Tab. 5.4. However, the difference between the fraction of clouds with a nearest neighbor within a distance of 1 times less than their cloud size is larger between scenes with high z_t and low z_t in the wet summer season compared to scenes in the dry winter season. Recalling the relationship between cloud top height and precipitation (section 5.3), we can deduce that raining clouds cluster more than non-raining clouds, in particular during summer.

5.5 Summary and Conclusion

Measurements of the year 2011 from a ground-based cloud radar, KATRIN, and a high spatially resolving space-borne radiometer, ASTER, are analyzed with the purpose to characterize cloud cover, cloud size distribution and organization of precipitating trade wind cumuli.

An investigation of KATRIN measurements on cloud top height (z_t) shows that clouds with high z_t rain more than clouds with low z_t. This knowledge is transferred to identify rainy and non-rainy ASTER scenes by using the information of the measured brightness temperature (T_b). Scenes with a cold T_b mark conditions of high z_t, and scenes with a warm T_b mark conditions with low z_t. Rainy ASTER scenes are defined by a mean cloud top height of 3 km and higher, and non-rainy ASTER scenes by a mean cloud top height of 1 km and lower.

The projected cloud cover (cc) from ASTER shows a high number of cases with low cloud cover (cc = 2%) and an exponential decrease for cases with a higher cloud cover. In the wet summer season, which is characterized by vigorous deep convective clouds (Nuijens et al., 2013), ASTER scenes with high z_t show a smaller cloud cover compared to scenes with low z_t, whereas in the dry winter season with a prevailing stratus layer the cloud cover is similar among ASTER scenes with high z_t and low z_t. This implies that the high number of cases with low cloud cover can be attributed to ASTER scenes with deep convective clouds during summer.

Cloud size analysis show that large clouds are found to contribute more to the total cloud cover than small clouds. This is in particular true in summer for ASTER scenes with high z_t, which are also characterized by clouds which cluster more than clouds in ASTER scenes with low z_t. Especially, large clouds are identified to account for most of these clusters, whereas small clouds are found to cluster less. These findings support the idea that precipitating clouds can be associated with a higher degree of organization than shallow clouds, especially during summer.

This study proposes that during summer a high degree of clustering occurs for few deep precipitating clouds, which are associated with a low cloud cover. The overall question, if clouds organize differently if they precipitate could therefore be answered with yes. Small variations in the humidity field of the (sub-)cloud layer are a strong candidate to be able to explain the susceptibility of trade wind clouds to precipitation and hence, the organization of the cumulus cloud field, as already discussed in chapter 4 and based on Seifert and Heus (2013). Future studies should focus on understanding how changes in precipitation affect the degree of organization, depending on the humidity field in the cloud layer.

Chapter 6

Conclusion and Outlook

6.1 General summary and conclusion

In this thesis the macrophysical characteristics of trade wind cumuli and their susceptibility to the formation of precipitation were investigated. For this purpose, observations from the space-borne instrument, the Advanced Spaceborne Thermal Emission and Reflection Radiometer (ASTER) and from different ground-based remote sensing instruments at the Barbados-Cloud-Observatory (BCO) were analyzed. The unique combination of the KATRIN cloud radar, a Raman lidar and a Micro Rain Radar at the BCO allowed to characterize the microphysical properties of trade wind cumulus clouds, their precipitation behavior and the humidity and temperature of the environment. Macrophysical characteristics of trade wind cumuli were observed by ASTER having a very high spatial resolution up to 15 m.

Before undertaking this investigation, one had to first answer the following question: ***Can measurements from a single location describe the variety of cloudiness in the trades?*** As discussed in chapter 3 this study concentrated on the microphysical properties of trade wind cumuli during conditions of differing humidity and aerosol concentrations using measurements obtained by the Raman lidar and KATRIN. The radar reflectivity provides an excellent measure for studying cloud microphysics because it is strongly correlated with the size of cloud droplets. In the developed retrieval algorithm, it was found that setting a threshold in reflectivity of dBZ = -35 best suites the needs to filter out any non-meteorological or spurious signal. In addition, using the scanning capabilities of the cloud radar, the daily variation and vertical distribution in radar reflectivity of clouds upstream and at the BCO were compared. The reflectivities were found to be similar among the different elevation angles implying that characteristics of trade wind clouds measured at the BCO represent "typical" trade wind cumuli, as well as capture the variety in cloudiness in the trades.

Having demonstrated the representativeness of BCO trade wind cumuli the signature of radar echoes from KATRIN was analyzed in chapter 4, answering the question: ***Can aerosols significantly alter the onset of precipitation of trade wind cumuli?*** Developing cumuli were identified by their increase of radar reflectivity with height, which can be expressed by the measure of Z^*, describing the best fit profile of reflectivity at a

height of 1 km above cloud base. It was shown that Z^* is a good proxy for conditions that favor a rapid onset of precipitation within shallow cumulus. Here, the impact of changes in the aerosol concentration and thermodynamic properties of the environment on Z^* was investigated. Aerosol concentrations were identified to vary seasonally and co-vary with relative humidity. No statistical significant differences in Z^* between days with high and low aerosol concentration were found by conditional sampling of various ranges in relative humidity. Computations of a simple entraining plume model showed that even on short time scales relatively large variations in the aerosol concentration had a smaller effect on changing Z^* than subtle variations in humidity. It was emphasized, that future studies should put their focus on understanding the interplay between the characteristics of shallow cumuli and subtle changes in their thermodynamic environment.

In chapter 5 the third question: ***Do precipitating clouds have common macrophysical characteristics?*** was tackled. Measurements by ASTER were used to study the macrophysical characteristics of precipitating trade wind cumuli during the dry winter season and the wet summer season. To identify rainy conditions in ASTER scenes, the relationship between rain amount and cloud top height (z_t) was assumed to be the same as observed in measurements by KATRIN. In this respect, the brightness temperature measured with ASTER was interpreted as a measure for z_t. During conditions with high z_t, the contribution to the total cloud cover of large clouds was identified to be larger than that of small clouds. Analysis of the cloud organization shows, that large clouds cluster more than small clouds. Most of these clusters were found to be related to clouds with high z_t during the wet summer season. Those findings suggested that during summer non-precipitating trade wind cumuli cluster less than precipitating clouds which were associated with a low cloud cover. Small variations in the humidity field of the (sub-)cloud layer were proposed to be a strong candidate to be able to explain variations in precipitation and hence, the degree of organization.

To summarize, the organization of trade wind cumuli and their susceptibility to rain formation has been investigated by analyzing measurements from the space-borne instrument ASTER and from measurements recorded at the BCO. The unique combination of continual, highly resolved observations in both, the vertical and in time, and the instrumental equipment at the BCO, enabled the capture of different trade wind cumuli properties and their environment. This also enabled one to obtain robust statistical signals of (even) small changes in modulating factors of trade wind cumuli, like relative humidity and aerosols. The observed signals on trade wind cumuli due to changes in the aerosol concentration, however, can potentially always be distorted by varying accompanying meteorological conditions. Furthermore, quantitative estimates of the sensitivity of trade wind cumuli to relative humidity are difficult to obtain from observations, which are always limited in space, time or the number of observable quantities. The next section discusses four ideas for future improvement on an analysis of modulating factors of precipitating trade wind cumuli, which have the ability to give further insights into their interplay with the environment.

6.2 Outlook

The first idea is in regards to studying the effects of seasonal characteristics on trade wind cumuli. KATRIN measurements of the BCO dataset now spans about three years, as opposed to the 15 months available at the time of this study. The extended dataset would allow for a more detailed study of the effect of changes in the aerosol concentration under conditions with differing relative humidity. As shown by Brueck (2012), the relative humidity varies within a year between low values in the dry winter season (December through May) and high values in the wet summer season (June to November). Additionally, between late spring and early fall large amounts of Saharan dust are transported over the Atlantic to the BCO leading to an increase in the aerosol concentration just above the inversion ($\sim 3\,\mathrm{km}$) in the trades (Prospero and Carlson, 1972). As shown in chapter 4, changes of cloud microphysical properties (as captured by Z^*) due to a large increase in aerosol concentration can be offset by a subtle increase in relative humidity. A dataset which spans over multiple wet and dry seasons would help to further quantify the effect of aerosol changes on trade wind cumuli under conditions of differing relative humidity.

The second idea is in regard to the height in which aerosol concentration are located. In this thesis, only the measure of the height-averaged linear-depolarization ratio revealed a small signal in the radar echo, however, all measures lack an information about the height level in which the aerosol is located. The information of the aerosols' location is important, as interactions between aerosols and clouds can only take place if they are in the vicinity of each other. Nevertheless, if aerosols had a strong impact on trade wind clouds it should have been observed with the used measures. The small signal in the radar echo indicates that the changes in the Saharan dust concentration have a small effect on trade wind clouds. If future studies are interested to quantify this small effect, they could investigate cases when clouds are surrounded by aerosol. The challenge in those studies will be the sensitivity of aerosol measurements by the Raman lidar to humidity.

The third idea would be to investigate how the manner in which ASTER observes clouds influences the analysis of the organization of clouds. While ASTER high resolution scenes offer detailed insights on the structure of even small clouds, the size of a ASTER scene is limited. As such cloud located in the center of an ASTER scene have most likely more adjacent clouds than clouds located at the edges of the scene. The "edge effect" has been neglected in this work, because it has only a strong impact for elongated scenes, as pointed out by Weger et al. (1992). However, artifacts can be expected within the range of one to two mean nearest neighbor distances to the image boundary. Another important aspect for the quantification of the degree of organization of clouds is the construction of an artificial random distributed cloud field, which can be compared to the observed cloud field. As already stated by Nair et al. (1998), this requires clouds to be considered as objects of finite size and not Poisson-distributed points. An analysis which considers the two mentioned aspects could offer insights into the details of cloud organization of every ASTER scene with ruling out sensitivities of the analysis to the way the instrument observes clouds, completely.

The last idea proposes that future investigations should be undertaken to quantify the effects of subtle changes in relative humidity on trade wind cumuli rather than effects by

large changes in aerosol concentration. Observed quantities which are less sensitive to the size of cloud droplets are believed to give a better quantitative estimate of the effect of subtle changes in relative humidity. Additionally, numerical simulations are needed because not every unresolved question concerning the interplay between trade wind cumuli, their environment and precipitation formation can be answered by an observational analysis. In this thesis a simple entraining plume model was used to estimate the effect of subtle changes in relative humidity on trade wind cumuli. A more advanced model in combination with long-term observations would help to further quantify the humidity effect and thereby offer the chance to gain detailed insights into the formation of precipitation of trade wind cumuli and their impact on the spatial distribution of clouds.

The aforementioned ideas proposed would serve for better quantitative estimates on the impact of aerosols and humidity to rain formation and the degree of organization. They would build upon the results of this thesis which showed that the organization of trade wind cumuli relates to precipitation, whose onset was identified to be dominated by subtle changes in relative humidity compared with large changes in aerosol concentration.

Appendices

Appendix

Back-trajectory analysis

The idea that maritime and continental air masses could have an impact on clouds was inspired by a back-trajectory analysis by Dr. Heike Wex from the Leibniz Institute for Tropospheric Research (TROPOS) using data from the CARRIBA field campaigns (Siebert et al., 2013). By assuming that in-situ aerosol data derived from ground-based measurements is representative for the aerosol at about 500 m ($\sim$ roughly cloud base), Dr. Heike Wex found that the origin of air masses correlates with aerosol concentration.

Compared to back-trajectories computed with HYSPLIT, the 10-days back-trajectories used by Dr. Heike Wex were provided by Dr. Stephan Henne, Empa (Swiss Federal Laboratories for Materials Science and Technology) using firefly.geog.umd.edu/firemap/. Here, the data is sampled according to an area over which the air mass passed before reaching the BCO in 500 m height. Continental air masses are identified if back-trajectories crossed an area which had burning mass fires (marked in the firemaps) or came from desert regions in Africa or South America. During the first phase of CARRIBA in November 2010, burning mass areas are identified at 8°N - 15.5°N, 6°W - 6°E; and desert areas at 15.5°N - 20°N, 16°W - 0° for Africa, and 5°S - 5°N, 50°W - 35°W for South America.

To investigate if clouds are influenced by maritime and continental air masses, measurements of reflectivity by the cloud radar at BCO are analyzed using the back-trajectory analysis by Dr. Heike Wex and the back-trajectories using the HYSPLIT model (see chapter 2.5). During the first phase of CARRIBA, reflectivity-height histograms are compiled from KIT, as shown in Fig. A.1. Despite the differing definitions of air mass of the two back-trajectories models a high similarity in the distribution of reflectivity between maritime and continental air masses is found. As seen in Fig. A.1a and Fig. A.1c many low reflectivity (Z) values are measured which increase with height up to 2.5 km in combination with a high number of large reflectivity values in the lower heights during maritime conditions. During continental conditions, this number of low and high reflectivity values in the lower heights is reduced (Fig. A.1b and Fig. A.1d). One could interpret the increase of low reflectivity values with height in the lower heights as shallow cumuli having a high tendency to form rain and the high values in Z as precipitation. That means, during maritime conditions the likeliness of precipitation is enhanced compared to continental conditions. These findings motivated to investigate if a signature of aerosols on trade wind cumuli clouds can be found for the whole measuring period of this work (chapter 4), by segregating cloud radar measurements into maritime and continental conditions.

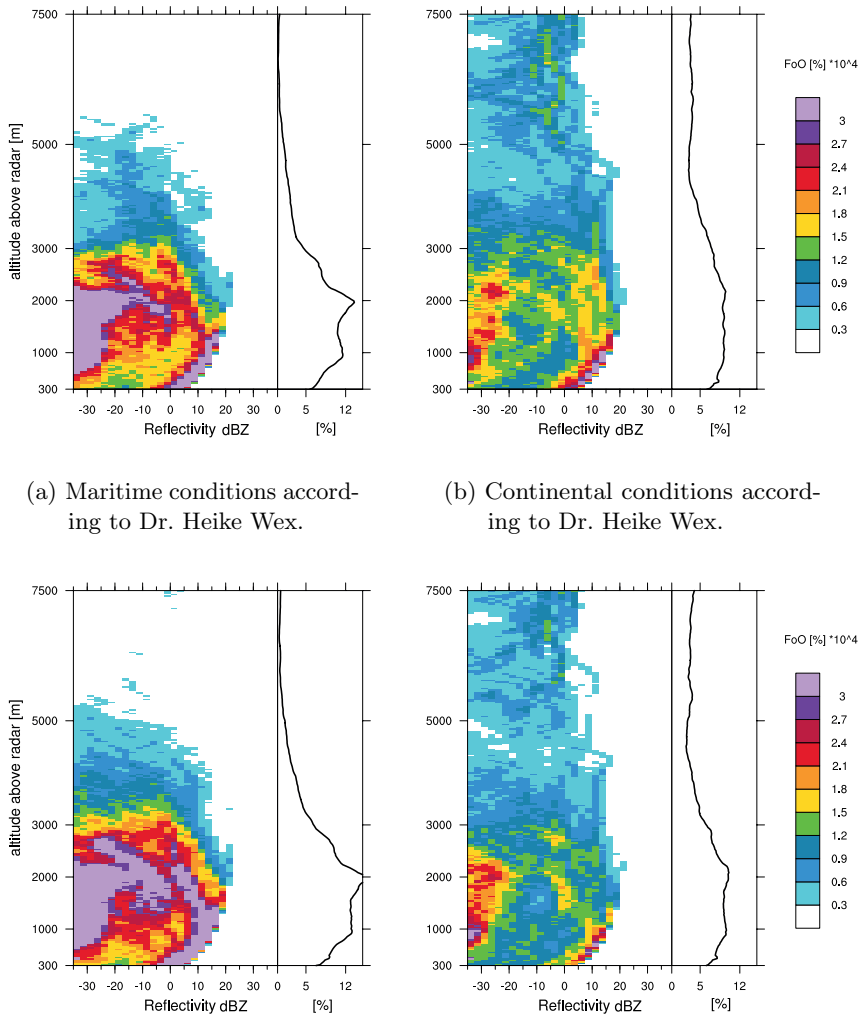

(a) Maritime conditions according to Dr. Heike Wex.

(b) Continental conditions according to Dr. Heike Wex.

(c) Maritime conditions as defined in this thesis.

(d) Continental conditions as defined in this thesis.

Figure A.1: Reflectivity-height histograms from KIT retrievals using the vertically pointing mode for the CARRIBA measurements period from 5 - 26 November 2010. Normalization is done by the sum of all actual retrievals. The frequency of occurrence (FoO) is calculated for every dBZ = 2.5. The black line on the right of each panel displays the number of retrievals per height level. Maritime and continental conditions are defined by the different back-trajectories.

Acronyms

A effective aperture of the antenna
ASTER Advanced Spaceborne Thermal Emission and Reflection Radiometer
B receiver bandwidth
BCO Barbados-Cloud-Observatory
C_{dB} radar constant
c speed of light
CIMH Caribbean Institute for Meteorology and Hydrology
D diameter of particles
DIAL differential absorption lidar
η radar reflectivity
F receiver noise factor
f_{D} Doppler shift in frequency
G antenna gain
HYSPLIT Hybrid Single Particle Lagrangian Integrated Trajectory Model
ITCZ Intertropical Convergence Zone
K_w dielectric factor
L power loss
λ wavelength
LDR linear depolarization ratio
MRR Micro Rain Radar
$n(D)$ particle size distribution
NND nearest neighbor distance
P_{b} backscattered power
P_{m} measured power
P_{n} receiver thermal noise power
PRF pulse repetition frequency
r reflectance
$S(f_{\mathrm{D}})$ Doppler spectrum
σ backscattering cross-section
SNR signal to noise ratio
SST sea surface temperature
TOA top of the atmosphere
T_b brightness temperature
θ azimuth angle

v_{D}	Doppler velocity
Z	radar reflectivity factor
Z_{e}	equivalent radar reflectivity factor
z_{t}	cloud top height

Bibliography

Albrecht, B. A., 1989: Aerosols, cloud microphysics, and fractional cloudiness. *Science*, **245**(4923), 1227–1230.

Albrecht, B. A., C. W. Fairall, D. W. Thomson, A. B. White, J. B. Snider, and W. H. Schubert, 1990: Surface-based remote-sensing of the observed and the adiabatic liquid water-content of stratocumulus clouds. *Geophysical Research Letters*, **17**(1), 89–92.

Bauer-Pfundstein, M. and U. Goersdorf, 2007: Target separation and classification using cloud radar doppler-spectra. In *33rd Conference on Radar Meteorology*.

Benner, T. C. and J. A. Curry, 1998: Characteristics of small tropical cumulus clouds and their impact on the environment. *Journal of Geophysical Research-atmospheres*, **103**(D22), 28753–28767.

Betts, A. K., 1997: Trade cumulus: Observations and modelling. *Physics and Parameterization of Moist Atmospheric Convection*, **505**, 99–126.

Blyth, A. M. and J. Latham, 1993: Influence of glaciation on an effective-radius parametrization. *Quarterly Journal of the Royal Meteorological Society*, **119**(514), 1469–1474.

Boers, R., J. R. Acarreta, and J. L. Gras, 2006: Satellite monitoring of the first indirect aerosol effect: Retrieval of the droplet concentration of water clouds. *Journal of Geophysical Research-atmospheres*, **111**(D22), D22208.

Brandau, C. L., H. W. J. Russchenberg, and W. H. Knap, 2010: Evaluation of ground-based remotely sensed liquid water cloud properties using shortwave radiation measurements. *Atmospheric Research*, **96**(2-3), 366–377.

Brueck, M. H., 2012: On the seasonal cycle of the north atlantic trades and its clouds. Master's thesis, Universität Hamburg, MIN-Fakultät, Fachbereich Geowissenschaften, Meteorologisches Institut.

Byers, H. R. and R. K. Hall, 1955: A census of cumulus-cloud height versus precipitation in the vicinity of puerto-rico during the winter and spring of 1953-1954. *Journal of Meteorology*, **12**(2), 176–178.

Deirmendjian, 1969: Electromagnetic scattering on spherical polydispersions. Technical report, Rand Corp. Santa Monica, CA, USA, 312 pp.

Draxler, R. R. and G. D. Hess, 1997: Description of the HYSPLIT_4 modeling system. Technical Report NOAA Tech. Memo. ERL ARL-224, NOAA Air Resources Laboratory, Silver Spring, MD, USA.

Frey, R. A., S. A. Ackerman, Y. Liu, K. I. Strabala, H. Zhang, J. R. Key, and X. Wang, 2008: Cloud detection with modis. part i: Improvements in the modis cloud mask for collection 5. *Journal of Atmospheric and Oceanic Technology*, **25**(7), 1057–1072.

Gerber, H. E., G. M. Frick, J. B. Jensen, and J. G. Hudson, 2008: Entrainment, mixing, and microphysics in trade-wind cumulus. *Journal of the Meteorological Society of Japan*, **86**, 87–106.

Grenzhäuser, J., 2012: Entwicklung neuartiger mess- und auswertungsstrategien für ein scannendes wolkenradar und deren anwendungsbereiche. Technical report, Institut für Meteorologie und Klimaforschung am Karlsruher Institut fr Technologie, Kaiserstr. 12, 76128 Karlsruhe, Germany.

Heus, T. and A. Seifert, 2013: Automated tracking of shallow cumulus clouds in large domain, long duration large eddy simulations. *Geoscientific Model Development*, **6**(4), 1261–1273.

Holloway, C. E. and J. D. Neelin, 2009: Moisture vertical structure, column water vapor, and tropical deep convection. *Journal of the Atmospheric Sciences*, **66**(6), 1665–1683.

Jensen, J., S. Lee, P. Krummel, J. Katzfey, and D. Gogoasa, 2000: Precipitation in marine cumulus and stratocumulus. - part i: Thermodynamic and dynamic observations of closed cell circulations and cumulus bands. *Atmospheric Research*, **54**(2), 117–155.

Jiang, H., G. Feingold, and A. Sorooshian, 2010: Effect of aerosol on the susceptibility and efficiency of precipitation in warm trade cumulus clouds. *J. Atmos. Sci.*, **67**(11), 3525–3540.

Johnson, R. H., T. M. Rickenbach, S. A. Rutledge, P. E. Ciesielski, and W. H. Schubert, 1999: Trimodal characteristics of tropical convection. *Journal of Climate*, **12**(8), 2397–2418.

Kaufman, Y. J., I. Koren, L. A. Remer, D. Rosenfeld, and Y. Rudich, 2005: The effect of smoke, dust, and pollution aerosol on shallow cloud development over the atlantic ocean. *Proceedings of the National Academy of Sciences of the United States of America*, **102**(32), 11207–11212.

Kim, B. G., M. A. Miller, S. E. Schwartz, Y. G. Liu, and Q. L. Min, 2008: The role of adiabaticity in the aerosol first indirect effect. *Journal of Geophysical Research-atmospheres*, **113**(D5), D05210.

Kotarba, A. Z., 2010: Estimation of fractional cloud cover for moderate resolution imaging spectroradiometer/terra cloud mask classes with high-resolution over ocean aster observations. *Journal of Geophysical Research-atmospheres*, **115**, D22210.

Krueger, A. F. and S. Fritz, 1961: Cellular cloud patterns revealed by tiros i1. *Tellus*, **13**(1), 1–7.

Liou, K. N. and S. C. Ou, 1989: The role of cloud microphysical processes in climate - an assessment from a one-dimensional perspective. *Journal of Geophysical Research-atmospheres*, **94**(D6), 8599–8607.

Lonitz, K., B. Stevens, L. nd Nuijens, and L. Hirsch, 2013: The signature of aerosols and meteorology in long-term cloud radar observations of trade-wind cumuli. *Journal of the Atmospheric Sciences*, **Submitted.**

Malkus, J. S., 1958: *On the structure of the trade wind moist layer*, volume 13. Massachusetts Institute of Technology and Woods Hole Oceanographic Institution.

Melchionna, S., 2010: *Retrieval of microphysical cloud properties: a novel algorithm for decomposing cloud radar spectra*. PhD thesis, Department Geowissenschaften der Universitat Hamburg.

Nair, U. S., R. C. Weger, K. S. Kuo, and R. M. Welch, 1998: Clustering, randomness, and regularity in cloud fields - 5. the nature of regular cumulus cloud fields. *Journal of Geophysical Research-atmospheres*, **103**(D10), 11363–11380.

Neggers, R. A. J., H. J. J. Jonker, and A. P. Siebesma, 2003: Size statistics of cumulus cloud populations in large-eddy simulations. *Journal of the Atmospheric Sciences*, **60**(8), 1060–1074.

Nicolae, D. and C. Talianu, 2010: Atmospheric lidars and retrieval of aerosol optical characteristics. In *Recent Advances in Atmospheric Lidars*, Luca Fiorani, V. M., editor, volume 7 of *Optoelectronic Material and Devices*. INOE.

Nuijens, L., I. Serikov, L. Hirsch, K. Lonitz, and B. Stevens, 2013: The distribution and variability of low-level cloud in the north-atlantic trades. *Quarterly Journal of the Royal Meteorological Society*, **Accepted**.

Nuijens, L., B. Stevens, and A. P. Siebesma, 2009: The environment of precipitating shallow cumulus convection. *Journal of the Atmospheric Sciences*, **66**(7), 1962–1979.

Prospero, J. M. and T. N. Carlson, 1972: Vertical and areal distribution of saharan dust over western equatorial north-atlantic ocean. *Journal of Geophysical Research*, **77**(27), 5255–&.

Prospero, J. M. and P. J. Lamb, 2003: African droughts and dust transport to the caribbean: Climate change implications. *Science*, **302**(5647), 1024–1027.

Rauber, R. M., H. T. Ochs, L. Di Girolamo, and Coauthors, 2007: Rain in shallow cumulus over the ocean: The rico campaign. *Bull. Amer. Meteor. Soc.*, **88**(12), 1912–1928.

Reutter, P., H. Su, J. Trentmann, M. Simmel, D. Rose, S. S. Gunthe, H. Wernli, M. O. Andreae, and U. Poschl, 2009: Aerosol- and updraft-limited regimes of cloud droplet formation: influence of particle number, size and hygroscopicity on the activation of cloud condensation nuclei (ccn). *Atmospheric Chemistry and Physics*, **9**(18), 7067–7080.

Riehl, H. and J. S. Malkus, 1957: On the heat balance and maintenance of circulation in the trades. *Quarterly Journal of the Royal Meteorological Society*, **83**(355), 21–29.

Riehl, H., T. C. Yeh, J. S. Malkus, and N. E. la Seur, 1951: The north-east trade of the pacific ocean. *Q.J.R. Meteorol. Soc.*, **77**(334), 598–626.

Russchenberg, H. and R. Boers, 2004: Radar sensor synergy for cloud studies; case study of water clouds. In *Weather Radar*, Meischner, P., editor. Springer Berlin Heidelberg, 235–254.

Saunders, P. M., 1965: Some characteristics of tropical marine showers. *Journal of the Atmospheric Sciences*, **22**(2), 167–&.

Savoie, D., D. L. and J. M. Prospero, 1980: Water-soluble potassium, calcium, and magnesium in the aerosols over the tropical north-atlantic. *Journal of Geophysical Research-oceans and Atmospheres*, **85**(NC1), 385–392.

Schubert, W. H., J. S. Wakefield, E. J. Steiner, and S. K. Cox, 1979: Marine stratocumulus convection .2. horizontally inhomogeneous solutions. *Journal of the Atmospheric Sciences*, **36**(7), 1308–1324.

Seifert, A. and T. Heus, 2013: Large-eddy simulation of organized precipitating trade wind cumulus clouds. *Atmospheric Chemistry and Physics*, **13**(11), 5631–5645.

Short, D. A. and K. Nakamura, 2000: TRMM radar observations of shallow precipitation over the tropical oceans. *Journal of Climate*, **13**(23), 4107–4124.

Siebert, H., M. Beals, J. Bethke, and Coauthors, 2013: The fine-scale structure of the trade wind cumuli over barbados; an introduction to the carriba project. *Atmospheric Chemistry and Physics*, **13**(19), 10061–10077.

Slingo, A., 1990: Sensitivity of the earth's radiation budget to changes in low clouds. *Nature*, **343**(6253), 49–51.

Snodgrass, E. R., L. Di Girolamo, and R. M. Rauber, 2009: Precipitation characteristics of trade wind clouds during rico derived from radar, satellite, and aircraft measurements. *Journal of Applied Meteorology and Climatology*, **48**(3), 464–483.

Stevens, B., 2005: Atmospheric moist convection. 605–643.

Stevens, B., A. S. Ackerman, B. A. Albrecht, A. R. Brown, A. Chlond, J. Cuxart, P. G. Duynkerke, D. C. Lewellen, M. K. Macvean, R. A. J. Neggers, E. Sanchez, A. P. Siebesma, and D. E. Stevens, 2001: Simulations of trade wind cumuli under a strong inversion. *Journal of the Atmospheric Sciences*, **58**(14), 1870–1891.

Stevens, B. and O. Boucher, 2012: Climate science: The aerosol effect. *Nature*, **490**(7418), 40–41.

Stevens, B. and J. L. Brenguier, 2009: Cloud-controlling factors low clouds. *Clouds In the Perturbed Climate System: Their Relationship To Energy Balance, Atmospheric Dynamics, and Precipitation* 173–196.

Stevens, B., D. Farrell, L. Hirsch, F. Jansen, I. Serikov, and L. Nuijens, 2013: On the edge of the ITCZ: Sampling climate changes most uncertain cloud regimes. *Bulletin of the American Meteorological Society*, **In preparation**.

Stevens, B. and G. Feingold, 2009: Untangling aerosol effects on clouds and precipitation in a buffered system. *Nature*, **461**(7264), 607–613.

Thome, K., S. Biggar, and P. Slater, 2001: Effects of assumed solar spectral irradiance on intercomparisons of earth-observing sensors. *Sensors, Systems and Next-generation Satellites V*, **4540**, 260–269.

Tiedtke, M., 1989: A comprehensive mass flux scheme for cumulus parameterization in large-scale models. *Monthly Weather Review*, **117**(8), 1779–1800.

Tompkins, A. M., 2001: Organization of tropical convection in low vertical wind shears: The role of cold pools. *Journal of the Atmospheric Sciences*, **58**(13), 1650–1672.

Twomey, S., 1974: Pollution and planetary albedo. *Atmospheric Environment*, **8**(12), 1251–1256.

van Zanten, M. C., B. Stevens, L. Nuijens, A. P. Siebesma, A. S. Ackerman, F. Burnet, A. Cheng, F. Couvreux, H. Jiang, M. Khairoutdinov, Y. Kogan, D. C. Lewellen, D. Mechem, K. Nakamura, A. Noda, B. J. Shipway, J. Slawinska, S. Wang, and A. Wyszogrodzki, 2011: Controls on precipitation and cloudiness in simulations of trade-wind cumulus as observed during rico. *Journal of Advances In Modeling Earth Systems*, **3**, M06001.

Warneck, P., 1988: *Chemistry of the Natural Atmosphere*, volume 41 of *International Geophysics*. Academic Press.

Warren, S., C. Hahn, J. London, R. Chervin, and R. Jenne, 1986: Global distribution of total cloud cover and cloud type amounts over land. Technical report, Atmospheric Analysis and Prediction Division (AAP).

Weger, R. C., J. Lee, T. R. Zhu, and R. M. Welch, 1992: Clustering, randomness and regularity in cloud fields .1. theoretical considerations. *Journal of Geophysical Research-atmospheres*, **97**(D18), 20519–20536.

Woodcock, A. H., 1940: Convection and soaring over the open sea. *Journal of Marine Research*, **3**(3), 248–253.

Yamaguchi, Y., A. Kahle, H. Tsu, T. Kawakami, and M. Pniel, 1998: Overview of advanced spaceborne thermal emission and reflection radiometer (aster). *Geoscience and Remote Sensing, IEEE Transactions on*, **36**(4), 1062–1071.

Zhang, S., H. Xue, and G. Feingold, 2011: Vertical profiles of droplet effective radius in shallow convective clouds. *Atmospheric Chemistry and Physics*, **11**(10), 4633–4644.

Zhao, G. Y. and L. Di Girolamo, 2007: Statistics on the macrophysical properties of trade wind cumuli over the tropical western atlantic. *Journal of Geophysical Research-atmospheres*, **112**(D10), D10204.

Zhao, M. and P. H. Austin, 2005: Life cycle of numerically simulated shallow cumulus clouds. part ii: Mixing dynamics. *Journal of the Atmospheric Sciences*, **62**(5), 1291–1310.

Zuidema, P., Z. J. Li, R. J. Hill, L. Bariteau, B. Rilling, C. Fairall, W. A. Brewer, B. Albrecht, and J. Hare, 2012: On trade wind cumulus cold pools. *Journal of the Atmospheric Sciences*, **69**(1), 258–280.

Acknowledgments

First, I gratefully thank Bjorn Stevens for supervising me over the past years of my PhD. In particular, I thank him for challenging me in way which allowed me to grow personally. His encouragement during times when "No signal was also a signal", his great ideas and his generous support for traveling to the BCO and conferences made this time to a memorable one. Second, I deeply thank Louise Nuijens for supporting me throughout my dissertation with her general interest in my work, inspiring discussions and valuable comments on earlier versions of chapter 4 and 5. Third, I thank Ákos Horváth for his external support and his idea to work with ASTER data in the beginning of my PhD. Fourth, I thank all the members of my advisory panel, Felix Ament and Stephan Bakan for their guidance and their valuable ideas during my studies.

Many thanks to the members of the BCO team: Stefan Kinne, Ilya Serikov, Friedhelm Jansen, Björn Brügmann, Holger Linné, Monika Pfeiffer and Lutz Hirsch for all their great efforts in the maintenance of the BCO and providing its dataset. In particular, I like to acknowledge Lutz and Ilya for their input on chapters 2 and 3. Furthermore, I thank Daniel Büttner for providing the information about the integrated linear depolarization ratio from the Raman lidar.

I very much thank Axel Seifert for giving me valuable comments on an earlier version of chapter 4 and for discussions about the organization of clouds. Furthermore, I like to acknowledge Christian Jacob for encouraging the cloud entity analysis. Robert Pincus is greatly thanked for his helpful comments related to the work with ASTER data in chapter 5. Special thanks to Matthias Bauer-Pfundstein for discussions on cloud radar retrievals and Jan Handwerker for letting the cloud radar from the Karlsruhe Institute of Technology, Karlsruhe, Germany operate at the BCO until January 2011. Also Heike Wex is thanked for early discussions concerning the back-trajectories analysis and Norbert Noreiks for graphical support.

I acknowledge the NOAA Air Resources Laboratory (ARL) for the provision of the HYSPLIT transport and dispersion model using the READY website (http://www.arl.noaa.gov/ready.php). ECMWF ERA-Interim data used in this work has been provided by ECMWF and have been obtained from the ECMWF Data Server. Leon Maldonado is thanked for his support with the ASTER proposal, which allowed us to obtain measurements of 1500 ASTER scenes over the Caribbean for the year 2011.

I would like to thank the IMPRS-ESM office for their financial support during my PhD and for providing an inspiring environment. In particular, I like to thank Antje Weitz, Cornelia Kampmann and Wiebke Böhm for their organizational and personal support which goes beyond their formal job duties.

Special thanks to Vera Schemann, Linda Schlemmer, Suvarchal Kumar, Sabrina Melchionna, and Christina Nam for their helpful comments on the manuscript and their editorial assistance. I deeply thank them and Irene Stemmler, Alex Khajetoorians, Julia Fruntke, Kevin Sieck, Dörte de Graaf, Felix Pithan, Thijs Heus and Renate Brokopf for distracting me by having hot and cold beverages; eating cake, Pho or lunch; climbing activities or simply a joyful time. Furthermore, I like to personal thank Gabriela Sousa Santos, Vivian Dietrich and Manuela Holz for wonderful times wherever we have been together.

Many, many thanks to my family, in particular to Ralf and my dad for their moral support and trust in me. Last but not least, I thank Daniel for cheering me up, for laughing with me, for his cooking skills and most importantly, for his love.

I dedicate this work to my mom.



ISSN 1614-1199